

國立交通大學
電子工程學系電子研究所
博士論文

光激砷化鎵中之全量子動力學
**Carrier Quantum Kinetics
in Photoexcited GaAs**

研究生：李漢傑

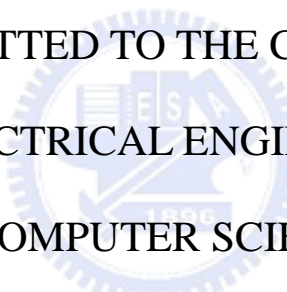
指導教授：李建平博士

中華民國九十三年六月

**CARRIER QUANTUM KINETICS
IN PHOTOEXCITED GaAs**

Han-Chieh Lee

A DISSERTATION
SUBMITTED TO THE COLLEGE
OF ELECTRICAL ENGINEERING
AND COMPUTER SCIENCE OF
NATIONAL CHIAO TUNG UNIVERSITY



ACCEPTANCE BY
THE DEPARTMENT OF
ELECTRONICS ENGINEERING
AND INSTITUTE OF ELECTRONICS

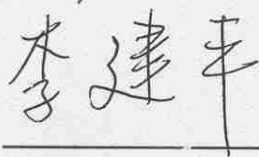
June 2004

推薦函

事由：推薦電子研究所博士班學生李漢傑舉行國立交通大學電機資訊學院博士畢業論文口試。

說明：電子所博士生李漢傑已通過博士資格考試、修畢系所規定學分、達到英語能力檢定之要求並完成博士論文初稿。論文題目為光激砷化鎘中之全量子動力學，該研究相關成果已在國際期刊及會議發表並已達系所規定要求，發表論文一覽表請參閱著作目錄。因此推薦李君舉行畢業論文口試。

此致，



李建平博士
國立交通大學電子所教授

中華民國九十三年四月二十日

國立交通大學

論文口試委員會審定書

本校電子工程學系電子研究所博士班李漢傑君
所提論文光激砷化鎵中之全量子動力學

合於博士資格標準、業經本委員會評審認可。

口試委員：
褚德三
朱仲夏
牟中瑜
汪大暉
孫建文
李建平

指導教授：李建平 教授
李建平

所長：陳紹基 教授
陳紹基

系主任：李鎮宜 教授
李鎮宜

中華民國九十三年五月二十七日


Department of Electronics Engineering
& Institute of Electronics
National Chiao Tung University
Hsinchu, Taiwan, R.O.C.

Date : 27/ May/ 2004

We have carefully read the dissertation entitled _____

Carrier Quantum Kinetics in Photoexcited GaAs

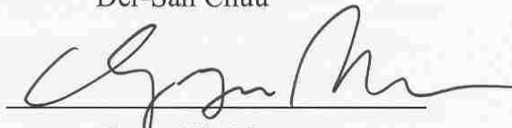
submitted by Han-Chieh Lee in partial fulfillment of the requirements of
the degree of DOCTOR OF PHILOSOPHY and recommend its acceptance.



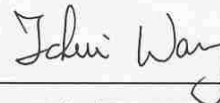
Der-San Chuu



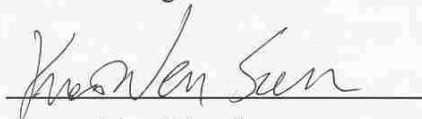
Chon-Saar Chu



Chung-Yu Mou



Tahui Wang




Kien-Wen Sun



Chien-Ping Lee

Thesis Advisor : 
Chien-Ping Lee

Director : 
Sau-Gee Chen

Chairman : 
Chen-Yi Lee

國立交通大學

博碩士論文著作權授權書

(提供授權人裝訂於紙本論文中書名頁之次頁用)

本授權書所授權之論文為本人在國立交通大學(學院)電子工程系所 固態電子 組，
92 學年度第 二 學期取得博士學位之論文。

論文名稱：光激砷化鎵中之全量子動力學
指導教授：李建平

同意 不同意 (國科會科學技術資料中心重製上網)

本人具有著作財產權之上列論文全文(含摘要)資料，授予行政院國家科學委員會科學技術資料中心(或改制後之機構)，得無限地域、時間與次數以微縮、光碟或數位化等各種方式重製後散布發行或上載網路。

本論文為本人向經濟部智慧財產局申請專利(未申請者本條款請不予理會)的附件之一，申請文號為：_____，註明文號者請將全文資料延後半年再公開。

同意 不同意 (圖書館紙本影印)

本人具有著作財產權之上列論文全文(含摘要)資料，授予教育部指定送繳之圖書館及國立交通大學圖書館，基於推動讀者間「資源共享、互惠合作」之理念，與回饋社會及學術研究之目的，教育部指定送繳之圖書館及國立交通大學圖書館得以紙本收錄、重製與利用；於著作權法合理使用範圍內，無限地域與時間，讀者得進行閱覽或列印。

本論文為本人向經濟部智慧財產局申請專利(未申請者本條款請不予理會)的附件之一，申請文號為：_____，註明文號者請將全文資料延後半年再公開。

■ 同意

本人具有著作財產權之上列論文全文(含摘要)，授予國立交通大學與台灣聯合大學系統圖書館，基於推動讀者間「資源共享、互惠合作」之理念，與回饋社會及學術研究之目的，國立交通大學圖書館及台灣聯合大學系統圖書館得無限地域、時間與次數，以微縮、光碟或其他各種數位化方式將上列論文重製，並得將數位化之上列論文及論文電子檔以上載網路方式，於著作權法合理使用範圍內，讀者得進行線上檢索、閱覽、下載或列印。

論文全文上載網路公開之範圍及時間：

本校及台灣聯合大學系統區域網路	■ 中華民國 96 年 6 月 1 日公開
校外網際網路	■ 中華民國 98 年 6 月 1 日公開

上述授權內容均無須訂立讓與及授權契約書。依本授權之發行權為非專屬性發行權利。依本授權所為之收錄、重製、發行及學術研發利用均為無償。上述同意與不同意之欄位若未勾選，本人同意視同授權。

研究生：李漢傑

學號：8711819

親筆正楷：李漢傑 (務必填寫)

中華民國 93 年 6 月 7 日

國家圖書館

博碩士論文電子檔案上網授權書

(提供授權人於辦理離校手續時繳交至系所用)

本授權書所授權之論文為本人在國立交通大學(學院)電子工程系所
固態電子組，92學年度第二學期取得博士學位之論文。

論文名稱：光激砷化鎵中之全量子動力學
指導教授：李建平

■ 同意

本人具有著作財產權之上列論文全文(含摘要)，以非專屬、無償授權國家圖書館，不限地域、時間與次數，以微縮、光碟或其他各種數位化方式將上列論文重製，並得將數位化之上列論文及論文電子檔以上載網路方式，提供讀者基於個人非營利性質之線上檢索、閱覽、下載或列印。

上述授權內容均無須訂立讓與及授權契約書。依本授權之發行權為非專屬性發行權利。依本授權所為之收錄、重製、發行及學術研發利用均為無償。上述同意與不同意之欄位若未勾選，本人同意視同授權。

研究生：李漢傑

學號：8711819

親筆正楷：李漢傑 (務必填寫)

中華民國 93 年 6 月 7 日

本授權書請以黑筆撰寫，並列印二份，其中一份影印裝訂於附錄三之一(博碩士論文授權書)之次頁；另一份於辦理離校時繳交給系所助理，由圖書館彙總寄交國家圖書館。

中文摘要

本論文理論地探討光激砷化鎵中之非熱平衡電子-電子碰撞及超快熱電子藉極性縱光聲子釋能的現象，其中的方法包括使用非熱平衡格林函數所建立的全量子動力理論及量子相位解調後的半古典波茲曼理論。庫倫碰撞率之奇異點在全量子動力理論的消失有助於比較動態遮蔽強度在不同維度空間的表現。迥於以往的研究結論，低維度空間的遮蔽強度應較高維度的空間強。該現象不僅在電子-電子碰撞成立，電子-極光聲子作用亦有相同的表現。這原因與低維度的庫倫作用力較強有關。此外，量子相位的存在也將使得電子分佈函數隨時間的演化具有記憶的行為。本論文首度發現在量子動力區間內，電子分佈函數將會由於電子-電子碰撞而有振盪的現象。該結果可成功地解釋過去超快同調光子解相時間隨電子濃度關係在量子井及塊材所得不同實驗結果的矛盾。

雖然過去超快熱電子釋能的研究已漸趨飽和，但關於釋能現象在不同空間維度的差異一直沒有一致的結論。本論文使用準二維的聲子模型精確地估計並比較熱電子能量損耗率在量子井及塊材的差別，並發現當電子濃度高於一臨界值 $2 \times 10^{18} \text{cm}^{-3}$ 時，塊材的熱電子釋能速率將明顯快於量子井。該維度的關係在電子-電子碰撞亦有相同的結論，根據計算的結果，非熱平衡的電子在塊材比量子井更快達到準熱平衡的狀態。這是由於電子在高維度的空間具有較多的碰撞路徑使然。另外，過去的認知一向認為熱聲子效應是抑制熱電子釋能的主因。然而，本研究發現量子井中高電子濃度下的動態遮蔽亦有相同抑制熱電子釋能的能力。電漿子-聲子耦合的效應也在計算中考慮，並發現在面電荷密度 10^{11}cm^{-2} 附近會明顯加速熱電子釋能速率，該現象與電子-電漿子碰撞有關。電子-極光聲子作用隨量子井結構改變的影響也將討論並與過去實驗的結果比較且有相當吻合的趨勢。

李漢傑 指導教授：李建平博士

Abstract

We theoretically studied the non-equilibrium carrier-carrier scattering in the quantum kinetic regime and the ultrafast hot-carrier relaxation through the Fröhlich interaction in photoexcited GaAs by solving the Generalized Kadanoff-Baym equation and the semi-classical Boltzmann equation, respectively. The singularity of scattering rate at the vanishing wave vector can be eliminated in the quantum kinetic theory. With the advantage, the difference of screening strength between a bulk and a quantum well can be compared. In contrast to the earlier understanding, the screening strength is shown to be stronger in a lower dimensional structure and this is an evidence for a stronger Coulomb interaction in a quantum well. The screening dependence is also held for the Fröhlich interaction. In the quantum kinetic regime, the Markovian approximation for the scattering process is no longer available due to the carrier's quantum coherence. The resulting memory effect is firstly demonstrated to be impact on the carrier's evolution. The carrier-carrier scattering leading to a burning hole on the carrier's distribution is shown at the early stage and is suggested to oscillate as the time further evolves. The theoretical result can successfully explain an earlier contradiction from the distinct measured power laws of the density dependence of photon-echo dephasing time in two different sample's dimensions.

Among the plenty of investigation on the hot carrier relaxation, the discrepancy from the dimensionality is clarified. With the dielectric continuum model, the hot carrier's energy-loss rate in a quasi-two dimensional structure was strictly calculated. Above the density of $2 \times 10^{18} \text{cm}^{-3}$, the hot carrier is shown to be significantly faster in a bulk than a 10nm-wide quantum well due to the higher density of states. The

dimensional dependence is also in consistent with the carrier-carrier scattering which shows a faster thermalization in a bulk. In addition, the dynamical screening in a quantum well on the shielding carrier-phonon interaction is demonstrated to be as important as the hot phonon effect when the carrier density is high. This rebuts the earlier argument where the dynamical screening can be neglected. The plasmon-phonon coupling was considered in the calculation and is shown to enhance the energy-loss rate around the density of 10^{11}cm^{-2} due to the carrier-plasmon scattering. The structure effect on the Fröhlich interaction was also presented and compared to earlier experimental results where a very good agreement can be obtained.

Han-Chieh Lee Advisor : Dr. Chien-Ping Lee



誌謝辭

耶和華有恩典有憐憫不輕易發怒並有豐盛的慈愛，祂萬不以有罪的為無罪，有罪的必追討他的罪自父及子直到三四代，愛祂守祂誠命的，必向祂發慈愛憐憫直到千代(出 34:6-8、申 5:9-10)。感謝神賜給我這些年來所受的訓練，不斷藉著祂的話鼓勵安慰我使我有盼望(羅 15:13)，疲乏的祂賜能力、軟弱的祂加力量(賽 40:29)，祂是在曠野開道路在沙漠開江河的神(賽 43:19)，願一切的頌讚都歸給祂(弗 1:3)。感謝李建平老師在研究上的批判、初期經費的支持和博士論文的修改、孫建文老師在修改英語寫作上的協助和晚期經費的支持、桂正楣老師在藉複變分析簡化二維電子氣介電函數計算的建議、林留玉仁老師在古典離子體的討論、教會中弟兄姐妹持續的代禱和關心以及父親在教育上長期的支持。

詩篇二十三篇

耶和華是我的牧者，我必不至缺乏，
他使我躺臥在青草地上，領我在可安歇的水邊，
他使我的靈魂甦醒，為自己的名引導我走義路，
我雖然行過死蔭的幽谷也不怕遭害，
因為你與我同在，你的杖你的竿都安慰我，
在我敵人面前你為我擺設筵席，你用油膏了我的頭使我的福杯滿溢，
我一生一世必有恩惠慈愛隨著我，我且要住在耶和華的殿中直到永遠。

Contents

Recommendation	iii
Committees	iv
Authorization	vi
Abstract	viii
Acknowledgment	xi
List of Figures and Tables	xv
Vita	xviii
Publication list	xix
1 Introduction	1
References	7
2 Non-equilibrium Carrier-Carrier Scattering	9
2.1 Introduction	9
2.1.1 Dynamical Screening and Dimensionality	9
2.1.2 Memory Effect	15
2.2 Quantum Kinetic Equation	17
2.3 Results and Discussion	20
2.3.1 2D versus 3D Dynamical Screening	20
2.3.2 Quantum Coherence on Carrier's Evolution	22
2.3.3 Scattering among Dense Fermi Sea	25
2.4 Summary	27
References	28

3	Hot Carrier Relaxation	30
3.1	Introduction	30
3.2	Semiclassical Boltzmann Equation	33
3.3	Results and Discussion	38
3.3.1	Reduced Dimensionality	39
3.3.2	Dynamical Screening versus Hot Phonon Effect	42
3.3.3	Well-Width Dependence	44
3.4	Summary	46
	References	47
4	Plasmon-Phonon Coupling	50
4.1	Introduction	50
4.2	Renormalized Phonon Propagator	52
4.3	Results and Discussion	54
4.3.1	Dispersion Relation	54
4.3.2	Average Energy-Loss Rate	55
4.3.3	Carrier Temperature Effect	59
4.4	Summary	62
	References	63
5	Structure Effect on Fröhlich Interaction	66
5.1	Introduction	66
5.2	Dielectric Continuum Model	67
5.2.1	Phonon Energy in GaAs/Al _x Ga _{1-x} As Quantum Wells	67
5.2.2	Electron-Phonon Scattering Rates	72
5.3	Intrasubband Scattering	76

5.4 Intersubband Scattering	84
References	87
6 Conclusion and Direction	89
References	91
A Calculating Interband Coulomb Quantum Kinetics	92
B Calculating Building up of Screening	95
C G Factor for Intersubband Scattering	98



List of Figures and Tables

Figure 2.1: Density dependence of photon-echo dephasing time in GaAs wells	10
Figure 2.2: Density dependence of photon-echo dephasing time in bulk GaAs	11
Figure 2.3: Comparison of photon-echo dephasing time between experimental and theoretical results	13
Figure 2.4: Time-resolved differential transmission spectra in an undoped, n-type doped and p-type doped quantum wells	16
Figure 2.5: Comparison of non-equilibrium carrier-carrier scattering in the quantum kinetic regime between a quantum well and a bulk	21
Figure 2.6: Comparison of non-equilibrium carrier's distribution at distinct excitation densities between a quantum well and a bulk	23
Figure 2.7: Comparison of 2D and 3D average relaxation time between the quantum and Boltzmann kinetic regimes	24
Figure 2.8: Comparison of non-equilibrium carrier-carrier scattering among dense Fermi sea between the quantum and Boltzmann kinetic regimes	26
Figure 3.1: Time-resolved photoluminescence in quantum wells and bulk GaAs	31
Figure 3.2: Comparison of hot-carrier cooling behavior between quantum wells and bulk	32
Figure 3.3: Average energy-loss rate with distinct conditions in a bulk GaAs and a 10nm GaAs/Al _{0.24} Ga _{0.76} As quantum well	40
Figure 3.4: Illustration of reduced dimensionality on hot carrier relaxation	41
Figure 3.5: Dynamical screening and hot phonon effect on average energy-loss rate in bulk GaAs and a 10nm GaAs/Al _{0.24} Ga _{0.76} As quantum well	43

Figure 3.6: Well-width dependence of average energy-loss rate in a GaAs/Al_xGa_{1-x}As quantum well 45

Figure 4.1: Dispersion curves of plasmon-phonon coupled mode in a 10nm GaAs/Al_{0.24}Ga_{0.76}As quantum well 56

Figure 4.2: Net plasmon-phonon generation rate in a 10nm GaAs/Al_{0.24}Ga_{0.76}As quantum well 57

Figure 4.3 Illustration of plasmon-phonon coupling on average energy-loss rate in a 10nm GaAs/Al_{0.24}Ga_{0.76}As quantum well 60

Figure 4.3 Illustration of carrier temperature on plasmon-phonon coupling in a 10nm GaAs/Al_{0.24}Ga_{0.76}As quantum well 61

Figure 5.1: Schematic diagram of hot-electron acceptor photoluminescence . . . 68

Figure 5.2: Dispersion curves of interface phonon modes in a 50nm GaAs/Al_{0.3}Ga_{0.7}As quantum well 71

Figure 5.3: Dependence of phonon energy of S+ and S- interface modes on the Al composition at minimum and maximum in-plane phonon wave vectors 77

Figure 5.4: Dependence of electron-phonon scattering rate of S+ mode, confined mode, and S- mode on the Al composition 78

Figure 5.5: Dependence of H and G factors on the in-plane phonon wave vector for interface phonon modes 79

Figure 5.6: Experimental and calculated results for dependence of effective phonon energy on the Al composition 81

Figure 5.7: Dependence of electron-optical phonon scattering rates on the well width in a quantum well 83

Figure 5.8: Structure dependence of intersubband scattering rate in a two-state quantum well 85

Figure 5.9: Intersubband scattering rate in a three-state quantum well with 10nm

width and 0.3 Al composition 86

Table I: The electron-optical phonon interaction strengths in a quantum well . . . 36

Table II: Used parameters for GaAs, AlAs and $\text{Al}_x\text{Ga}_{1-x}\text{As}$ materials 70

Table III: The potential in a quantum well for various phonon modes 75



Chapter 1

Introduction

Kinetic theory is of fundamental importance in many branches of physics such as in the condensed matter, nuclear, astronomy, etc., and is of strong dependence on the many subjects of applied mathematics such as the statistics, analysis, and geometry, etc. The goal of kinetic theory is to understand the dynamics of a many-particle system and to construct a bridge linking the macroscopic and microscopic variables in a substance. The preliminary step in the theory is to deal with the equilibrium statistical mechanics, where the notion of the ensemble is introduced. Ensemble is a very useful concept in statistical mechanics and it represents repeatedly mathematical experiments conducted on a system consisting of particles and fundamental interactions with the same conditions. The purpose of the experiments is to obtain a many-particle equilibrium distribution by averaging all undetermined factors such as the thermal fluctuation. Based on the Birkhoff-Khinchin ergodic theorem¹, the distribution function will reach an asymptotic solution when the number of experiments is large enough. By the particle's property, the solution for the distinguishable particle is the Maxwell-Boltzmann distribution and the solutions for the indistinguishable particle can be further classified into the Fermi-Dirac and Bose-Einstein distributions for Fermions and Bosons, respectively. When the given system is out of equilibrium, the existence of an asymptotic solution for the ensemble experiment is the most central problem in statistical mechanics. To hold the validity of the ergodic theorem, the time resolution in the non-equilibrium region must be long

enough so that there is an asymptotic solution however it is still in the interesting time scale.

In the classical kinetic theory, the time evolution of a many-particle distribution function can be obtained by solving the Bogoliubov-Born-Kirkwood-Green-Yvon (BBKGY) equation². The equation is based on the Liouville theorem where the density flux in a differential volume of the space-momentum coordinate is conserved for the distinguishable particles. The subsequent degree of approximations for the equation can be made to obtain a variety of the kinetic equations. Using one-particle distribution could be the most important approximation in the kinetic theory because it significantly reduces the huge calculations where the distribution functions of every particle in the given system should be considered. The approximation is valid for the dilute-enough particle density where the coupling among distinct particles disappears so that the many-particle distribution function can be simplified by the product of a one-particle distribution. The result is the well-known Boltzmann equation. When a perturbation is turned on, the non-equilibrium distribution will evolve due to a variety of scattering mechanisms in the given system. These scatterings cause the disturbed particles to lose their excess energies inputted by the external excitation or to exchange energies among themselves or with the surrounding until the equilibrium state is reached. Quasi-thermal equilibrium is an intermediate stage between the non-thermal and the equilibrium states where the distribution function can be approximately characterized by specific parameters and where further simplifications can be made for the Boltzmann equation. By comparing the mean-free path of scatterings to the length of local quasi-equilibrium, the Chapman-Enskog expansion and the Maxwell-Grad method³ can be used to derive the so-called Navier-stokes and the Burnett equations, where they have different levels to approximate the deviated-equilibrium distribution by using parameters such as temperatures, chemical

potentials, hydrodynamic velocities, etc. and their gradients. By solving the equations, the solutions can show the time evolution of the spatial non-uniformity for the deviated distribution, which is very useful to analyze various fluid motions such as the Laminar and turbulent flows.

In the quantum kinetic theory (QKT), the notion of the distribution function in the space-momentum phase space can be no longer available because the state vector for the description of a particle in the spatial coordinate has been generalized to the Hilbert space, where the uncertainty principle arises. The distinct statistical algorithm for identical particles from distinguishable particles causes that the accompanying kinetic equation must be reconstructed to satisfy the updated particle's property. In the Schrödinger picture, the non-equilibrium Green function can be used to derive the so-called generalized Kadannoff-Baym equation⁴ and the Schwinger-Keldysh formulation⁵, that were built up in the early 1960s. In the Heisenberg picture, von Neumann and Dirac used the density matrix method to explore the quantum kinetic theory⁶ independently in the 1930s. The Master equation derived from the method is now frequently used in the quantum statistics of optics⁷. The intermediate stage between the classical and the quantum kinetic theory includes using the Wigner function and the semiclassical Boltzmann equation. The Wigner function proposed by Wigner in 1932 is a created function quantum analogical to the space-momentum phase space for the statistical requirements⁸. Although the functional concept is principally classical, the applications are still effective for partial situations of high-energy particles. Starting from the Klein-Gordon equation for spinless particles or the Dirac equation for spin particles⁹, the relativistic kinetic theory has been well constructed in the present day¹⁰. By using the technique of the quantum field theory¹¹ the weak and strong interactions¹² are included in the kinetic equation where the applications have been widely used in the astronomical and nuclear circumstances

such as the neutrino¹³ and the pion particles¹⁴, respectively. Another simplified formalism before the QKT is to use the semiclassical Boltzmann equation. With the classical notion of the phase space, the distribution function in the space-momentum coordinate is still used while the inside collisional integrals are derived in quantum mechanics. A number of applications in condensed matters can be derived from the semi-classical method such as the Cooper pair dynamics in superconductors, the charge-density-wave dynamics in one-dimensional metal chains¹⁵, and the carrier dynamics in semiconductors¹⁶. During the last two decades, there is a new approach to the QKT due to the advantage of the rapid progress in the computing ability on the workstation and it is the so-called quantum Monte Carlo method. The Monte Carlo method is a mathematical game to simply determine the outcomes by using a random-number generator and was initially used to simulate the reaction and the trajectory of nuclear substances inside the reactor and to design the reactor structure where the wall can shield the outgoing radiations. The quantum Monte Carlo method is the improvement considering the statistical property of identical particles and can be appropriated to model the time evolution of the many-particle quantum states by using the simulation where fewer particles as compared to the actual numbers in the given system are performed.

The primary features in the QKT are due to the non-Markovian process and the energy (momentum) non-conservation. The Markovian process is a non-memorial scattering effect, where the earlier scattering information is not saved in the dynamical system so that the time evolution of a distribution function is as a scattering result with the instantaneous moment, and is often assumed in the classical kinetic theory. However, the assumption of the Markovian process is not held longer in the QKT because the evolution of the quantum state is a continuous process from the perturbation is turned on to the quantum coherence is broken. An atom oscillates

between the two states where a coherent and resonant light source is incident, the Rabi oscillation, is a clear example¹⁷. Another feature, the energy (momentum) non-conservation, is as a result of the uncertainty principle. This is not surprised because at the time (space) scale where the energy (momentum) uncertainty is comparable to the exchanged energy (wave vector) in a scattering process, the energy (momentum) distribution, not due to the ensemble average, covers a wide range and the conservation becomes meaningless in the ultrashort scale. Unless the time (length) evolves long enough, the conservation rule may recover. The Fermi golden rule is an example, where the energy conserve as the time goes to the infinity.

The quantum kinetic effects in semiconductors have attracted a lot of attention because of the fundamental interest and device applications (in the near future). In semiconductors, the time and length scales where the kinetic effects mentioned above arises are in the femtosecond and the nanometer, respectively, and the ranges are also called the quantum kinetic regime. With the advantage in semiconductor manufacturing technology, the semiconductor sample can be prepared with a very high quality, which makes the possible measurement of quantum kinetic effects, because the external dephasing scatterings from the lattice imperfection or the impurity can be significantly avoided. By using the ultrafast spectroscopy¹⁸, a non-equilibrium carrier's distribution in semiconductors can be generated by illuminating a femtosecond laser pulse with a photon energy higher than the bandgap and the following carrier's time evolution can be measured by using the pump-probe or the four-wave-mixing techniques. Several reports have demonstrated the memory effect^{19,20} and the energy non-conserving event^{21,22} on the carrier-phonon interaction in the recent years. The validity of the quantum kinetic theory has also been examined. On the other hand, for device applications, the current models in semiconductor devices such as the current-voltage characteristic still stand at the level of

semi-classical Boltzmann theory. However, as the integrated-circuit technology evolves rapidly, the next generation of electronic devices with dimensions in the nano-meter scale would require the use of the QKT because the wave interference in the spatial scale becomes increasingly important.

In the thesis, the quantum kinetic carrier-carrier scattering in photoexcited GaAs is studied. The non-equilibrium Green function was used to derive the quantum kinetic equation. By solving the equation, the carrier's evolution was obtained and was found the memory effect. Another interesting fact in the QKT is the absent singularity of scattering rate at the vanishing wave vector²³. With the advantage, the screening strength in different sample's dimensions was studied. In contrast to earlier understanding²⁴, a stronger screening in a quantum well than a bulk is demonstrated. The result is also in good agreement with the carrier-polar-optical phonon scattering, which has a similar dimensional dependence of the interaction Hamiltonian. Hot carrier relaxation through the several phonon types simply governed by the semiclassical Boltzmann equation was presented. The discrepancies including the dynamical screening, the dimensionality, and the well-width dependence from earlier experiments^{25,26} can be clarified. Re-normalized phonon propagator due to the plasmon coupling was also considered and is shown to have an important effect on the hot carrier's energy-loss rate around intermediate carrier densities. The outline of the thesis is as follows. In chapter 2 we present the non-equilibrium carrier-carrier scattering in the quantum kinetic regime. In chapter 3 the hot carrier relaxation and the relevant derivation including the net phonon generation rate, the hot phonon effect, etc. is discussed. The plasmon-phonon coupling is in Chapter 4. In chapter 5 we discussed the structure effect on the Fröhlich interaction, where the fundamental of phonon types in a double heterostructure and material parameters used in the thesis are also shown. In chapter 6 we give a conclusion and a direction of the work.

References

1. R. Balescu, *Equilibrium and Nonequilibrium Statistical Mechanics* (1975).
2. R. Liboff, *Kinetic Theory: classical, quantum, and relativistic descriptions* (John Wiley & Sons, New York, 1990).
3. S. Chapman and T. G. Cowling, *The Mathematical Theory of Non-uniform Gases*, 3rd ed. (Cambridge University Press, Cambridge, 1970); H. Grad, *Comm. Pure Appl. Math.* **2**, 331 (1949).
4. L. P. Kadanoff and G. Baym, *Quantum Statistical Mechanics* (Benjamin, New York, 1962).
5. J. Schwinger, *J. Math. Phys.* **2**, 407 (1961) and L. V. Keldysh, *Sov. Phys. JETP* **20**, 1018 (1965).
6. J. von Neumann, *Mathematische Grundlagen der Quantenmechanik*, Berlin (1932) and P. A. M. Dirac, *The Principles of Quantum Mechanics*, (Clarendon, Oxford, 1930).
7. Y. Yamamoto, *Mesoscopic quantum optics* (John Wiley & Sons, New York, 1999).
8. E. P. Wigner, *Phys. Rev.* **40**, 749 (1932).
9. P. Strange, *Relativistic Quantum Mechanics: with applications in condensed matter and atomic physics* (Cambridge University Press, New York, 1998).
10. S. R. de Groot, W. A. van Leeuwen, Ch. G. van Weert, *Relativistic Kinetic Theory: Principles and Applications* (North-Holland, Amsterdam, 1980).
11. F. Mandl and G. Shaw, *Quantum Field Theory* (Wiley, New York, 1984).
12. Q. Ho-Kim, X. Y. Pham, *Elementary Particles and Their Interactions: Concepts and Phenomena* (Springer, Berlin, 1998).
13. R. N. Mohapatra and P. B. Pal, *Massive Neutrinos in Physics and Astrophysics* (World Scientific, Singapore, 1991).

14. T. Ericson and W. Weise, Pions and Nuclei (Oxford University Press, New York, 1988).
15. G. Gruner, Density Waves in Solids (Addison-Wesley, Massachusetts, 1994); J. Demsar, K. Biljakovic, and D. Mihailović, Phys. Rev. Lett. **83**, 800 (1999); H. W. Yeom, S. Takeda, E. Rotenberg, I. Matsuda, K. Horikoshi, J. Schaefer, C. M. Lee, S. D. Kevan, T. Ohta, T. Nagao, and S. Hasegawa, Phys. Rev. Lett., **82** 4898 (1999).
16. B. K. Ridley, Quantum Processes in Semiconductors (Oxford University Press, New York, 1988).
17. H. Haken, Light: waves, photons, atoms, (North-Holland, Amsterdam, 1981).
18. J. Shah, Ultrafast Spectroscopy of Semiconductors and Semiconductor Nanostructures (Springer, Berlin, 1996).
19. L. Bányai, D. B. Tran Thoai, E. Reitsamer, H. Haug, D. Steinbach, M. U. Wehner, M. Wegener, T. Marschner and W. Stolz, Phys. Rev. Lett. **75**, 2188 (1995).
20. J. Schilp, T. Kuhn, and G. Mahler, Phys. Rev. B **50**, 5435 (1994).
21. M. Betz, G. Göger, A. Laubereau, P. Gartner, L. Bányai, H. Haug, K. Ortner, C. R. Becker, and A. Leitenstorfer, Phys. Rev. Lett. **86**, 4684 (2001).
22. C. Fürst, A. Leitenstorfer, A. Laubereau, and R. Zimmermann, Phys. Rev. Lett. **78**, 3733 (1997).
23. K. El Sayed, L. Bányai, and H. Haug, Phys. Rev. B **50**, 1541 (1994).
24. J. -Y. Bigot, M. T. Portella, R. W. Schoenlein, J. E. Cunningham, and C. V. Shank, Phys. Rev. Lett. **67**, 636 (1991).
25. K. Leo, W. W. Rühle, and K. Ploog, Phys. Rev. B **38**, 1947 (1988).
26. W. S. Pelouch, R. J. Ellingson, P. E. Powers, C. L. Tang, D. M. Szymyd, and A. J. Nozik, Phys. Rev. B **45**, 1450 (1992).

Chapter 2

Non-equilibrium Carrier-Carrier Scattering

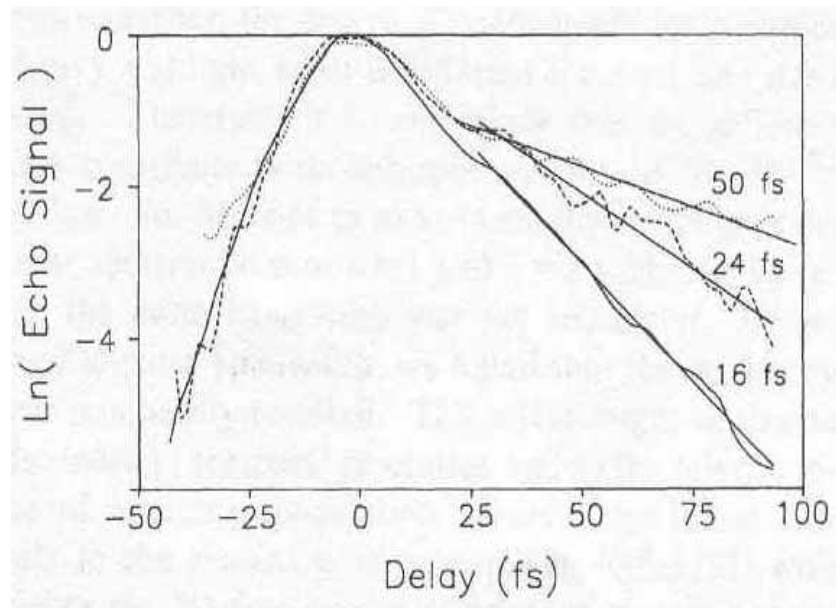
2.1 Introduction

2.1.1 Dynamical Screening and Dimensionality

Dynamical screening is of fundamental interest in semiconductors and is also an important effect on the carrier-carrier and the carrier-phonon interactions. Since the ultrafast four-wave-mixing (FWM) experiment¹ was introduced, the dependence of dynamical screening on the sample's dimension has been further investigated. In the earlier report^{2,3}, the photon-echo dephasing time at different excited carrier densities (n) had been measured and the dependence was found to be governed by the power law of $n^{-\frac{1}{D}}$, where D represents the dimension, shown in Fig. 2.1 and 2.2. The reason for the photon-echo dephasing was attributed to the carrier-carrier scattering (CCS), which leads the non-equilibrium carrier distribution spreading out so that the photon-echo's coherence is broken. In their assumption, the shielding potential in the CCS had built up at the measured time interval and thus the power law is as a result of screened scattering rate. If the shielding potential was not developed, the dephasing process would become more quickly due to a faster CCS, and the power law would also change, in principal, to satisfy the dependence of n^{-1} for both sample's structures.

By comparing the two kinds of power law, the dynamical screening was found to be

(a)



(b)

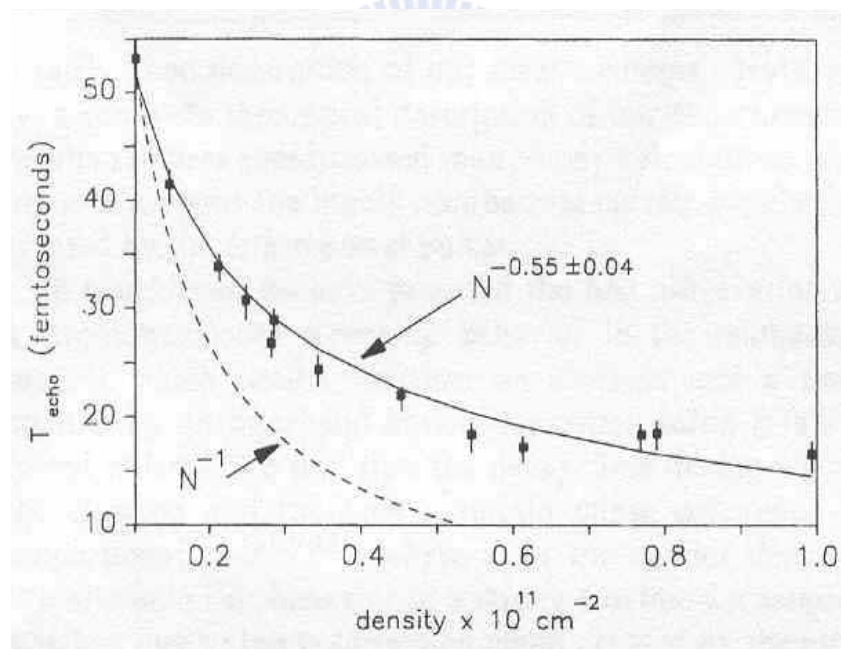
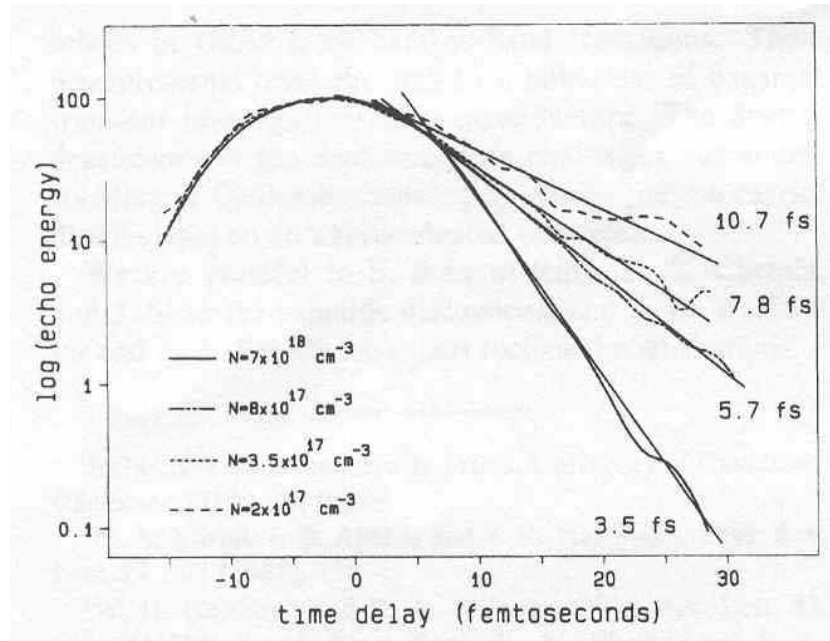


Figure 2.1: Time-resolved four-wave mixing results from Bigot's experiment in GaAs quantum wells. (a) Extraction of photon-echo dephasing time. (b) Density dependence of photon-echo dephasing time. Solid line: the fitting curve for the measured result. Dash line: the curve of unscreened carrier-carrier scattering rate. (quoted from Phys. Rev. Lett. **67**, 636 (1991))

(a)



(b)

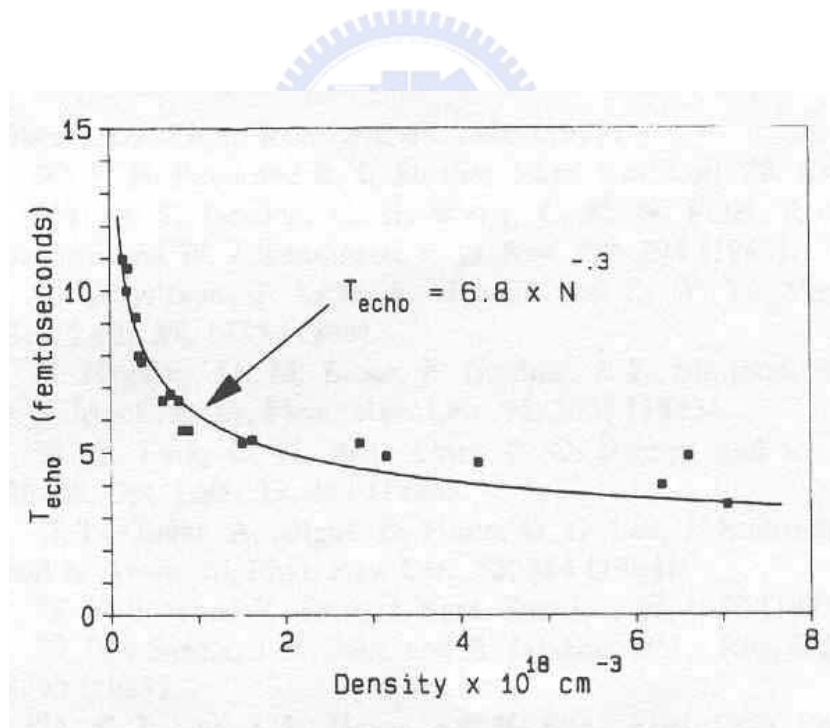


Figure 2.2: Time-resolved four-wave mixing results from Becker's experiment in bulk GaAs. (a) Extraction of photon-echo dephasing time. (b) Density dependence of photon-echo dephasing time. Solid line: the fitting curve for the measured result. (quoted from the Phys. Rev. Lett. **61**, 1647 (1988))

weaker in a quantum well because the variation from n^{-1} to $n^{-\frac{1}{D}}$ in a two dimension (2D) is smaller.

The screening dependence was, in general, accepted for more than one decade until a conflicting result was demonstrated experimentally and theoretically⁴. Under the same experiment of ultrafast FWM in GaAs, the photon-echo dephasing times at different excited carrier densities were re-measured; however, the significant power law $n^{-\frac{1}{D}}$ cannot be repeated. Unexpectedly, the dephasing time as a function of the carrier density was satisfied the $n^{-\frac{1}{3}}$ dependence for both a quantum well and a bulk. For a further examination, the time evolution of optical polarization field coupled to the CCS at different carrier densities was calculated with using the quantum kinetic theory. By extracting the dephasing time from the polarization field, the function of dephasing time on the carrier density can be obtained and also shows the dependence⁴, shown in Fig. 2.3. Thus, from the result one cannot determine which structure the carrier has a stronger or weaker screening strength in. In addition, according to the estimation of screening buildup⁵, for a low carrier density the shielding potential has been not completely developed at the measured time interval. Thus, the conventional method is also weak in the comparison of screening strength between the two sample's structures.

Recently, the screening dependence for the Fröhlich interaction⁶ was discovered. Although the scattering mechanism between the Fröhlich and the carrier-carrier interactions is different, the result is still meaningful because their unscreened Coulomb interactions in the Fourier space ($\propto 1/qL^2$ in 2D and $\propto 1/q^2L^3$ in 3D) are very similar, where q and L denotes the exchanged wave vector and the sample's length, respectively. Nevertheless, for the Fröhlich interaction, the dynamical screening was shown to be stronger in a quantum well than a bulk. This is opposite to

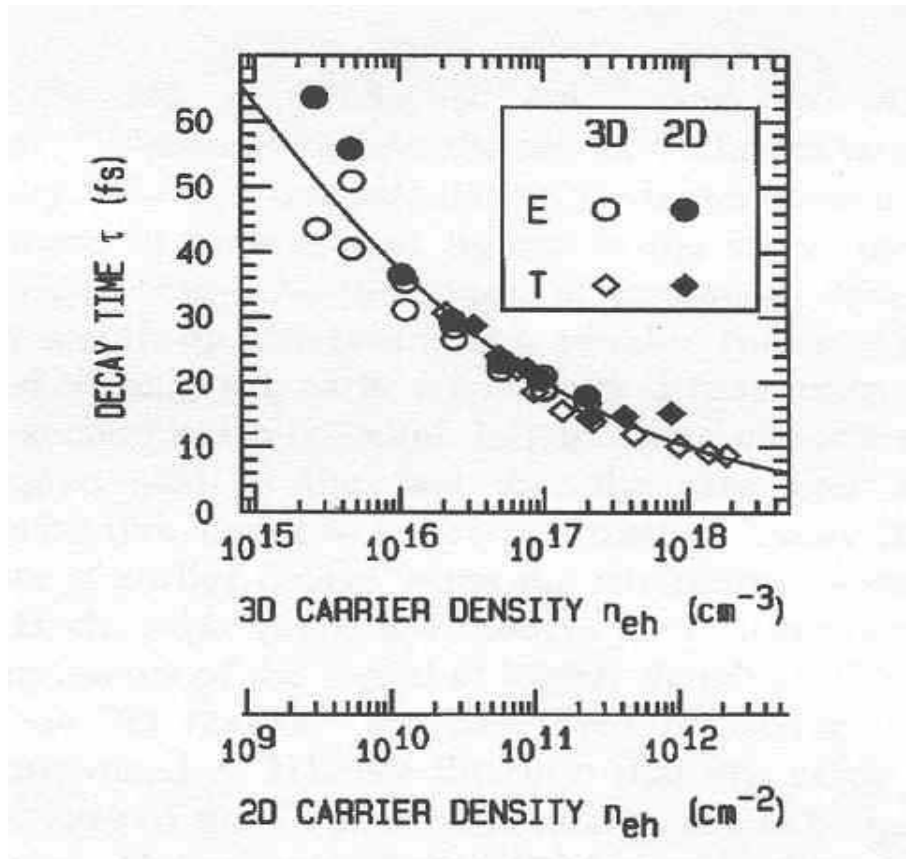


Figure 2.3: Density dependence of photon-echo dephasing time from Mieck's results in a quantum well and a bulk. E: experiment. T: theory. (quoted from Phys. Rev. B **62**, 2686 (2000))

the earlier understanding but is in agreement with the electrodynamics. In a lower dimension the electric flux has a stronger confinement so that has a stronger electric flux density than that in a higher dimension. Because the screening is a many-particle effect to shield an external charge source, it acts as a sub-Coulomb interaction and would also follow the dependence. The static screening (abbreviated as s.s.) is a verification. As the exchanged wave vector large enough ($q \gg \kappa_{2D}, \kappa_{3D}$), where κ denotes the screening wave vector, the screened Coulomb interaction in the two distinct dimensions can be written as a series.

$$V_{s.s.}^{2D}(q) = \frac{e^2}{(q + \kappa_{2D})L^2 \epsilon_\infty} \cong \frac{e^2}{qL^2 \epsilon_\infty} \left(1 - \frac{\kappa_{2D}}{q} + \dots\right) \quad (2.1a)$$

$$V_{s.s.}^{3D}(q) = \frac{e^2}{(q^2 + \kappa_{3D}^2)L^3 \epsilon_\infty} \cong \frac{e^2}{q^2 L^3 \epsilon_\infty} \left(1 - \left(\frac{\kappa_{3D}}{q}\right)^2 + \dots\right) \quad (2.1b)$$

where ϵ_∞ denotes a high-frequency dielectric constant. In the series the next leading term κ_{2D}/q and $(\kappa_{3D}/q)^2$ stands for the screening factor. Although κ_{2D} and κ_{3D} have different values, the 3D screening factor is generally smaller due to the square power. This dependence is also held for the opposite limit ($q \ll \kappa_{2D}, \kappa_{3D}$).

Dynamical screening is more complex because it is a time-dependent interaction, and should be studied with using the non-equilibrium carrier's evolution. The carrier's evolution can be obtained by solving the kinetic equation. In the semiclassical Boltzmann equation, there is a singular point at the vanishing exchanged wave vector where the unscreened scattering rate is divergent. One must consider the screening effect to eliminate the singularity so that the scattering rate becomes finite. However, the divergence can be avoided in the quantum kinetic theory⁷ (QKT) because the state vector in Hilbert space leading to the energy uncertainty can smooth it. This is an advantage because one can obtain two kinds of non-equilibrium carrier's evolution

(screened and unscreened) and then compare the difference to show the screening strength. In the report, the non-equilibrium Green function was used to derive the quantum kinetic equation and the solution therein also verifies the screening dependence as the Fröhlich interaction as we mentioned above.

2.1.2 Memory Effect

The carrier's quantum coherence not only smoothes the singularity but also relaxes the conservation of energy (or momentum) and the Markovian approximation for a scattering event. In the last decade, the energy non-conservation has been demonstrated in semiconductors experimentally and theoretically^{8,9} but the non-Markovian effect is still not well understood¹⁰. The Markovian approximation is valid for the carrier's scattering is instantaneous and independent on the past carrier's distribution. This is no longer held for the carrier's quantum kinetics because the evolution of quantum state is a continuous process with respect to the time from the excitation turned on to the coherence broken down. In this thesis, we discover that the relaxed Markovian approximation would cause an impact effect on the carrier's evolution. Since the non-equilibrium carrier is generated, the carrier begins to scatter with each other and spreads out. As the time evolves, the past carrier's distribution would increase the scattering rate and causes a burning hole in the carrier's evolution.

Earlier, Knox experimentally found a very rapid thermalization (less than 10fs) of non-equilibrium carrier among a cold electron's background in a quantum well¹¹, shown in Fig. 2.4. The carrier's evolution has a strong dependence on the cold electron and the specific dimension. However, up to now, the physical mechanism is still not understood. Kane theoretically obtained the carrier's evolution¹² by solving the Boltzmann equation but cannot repeat the result. We go further to the problem within the quantum kinetic regime. With the absent singularity, the effect of 2D cold

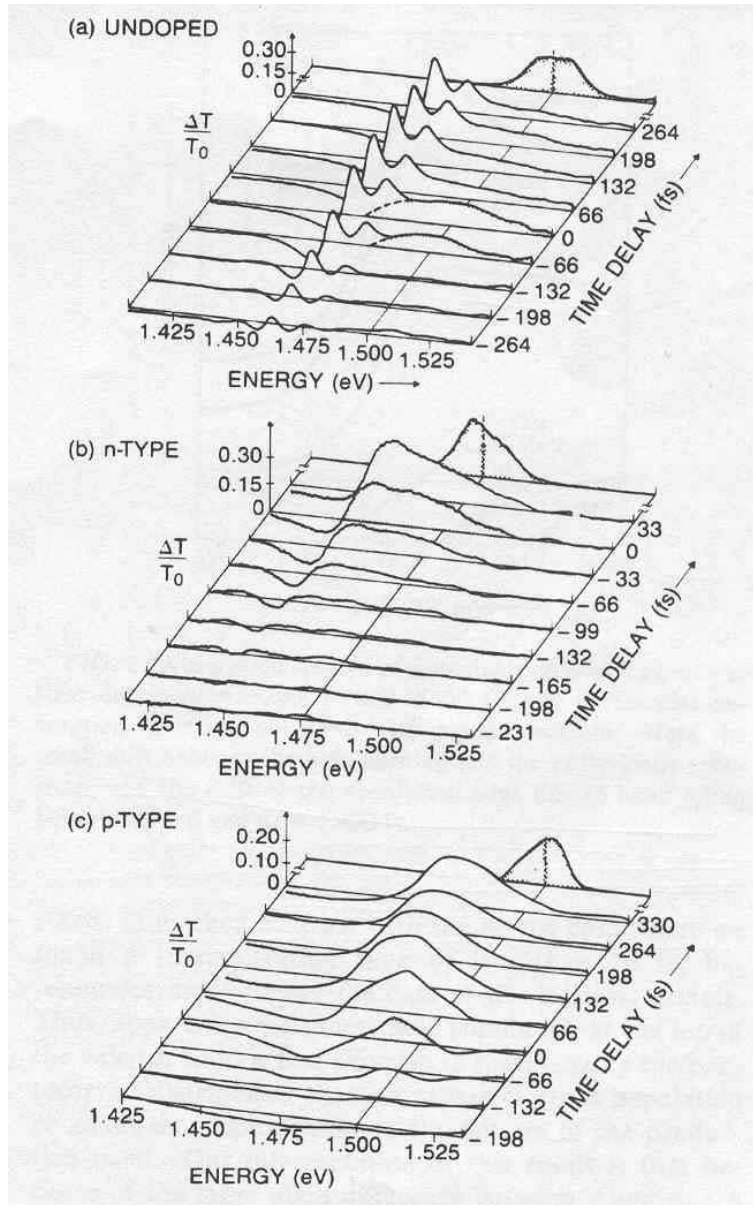


Figure 2.4: Time-resolved differential transmission spectra from Knox's experiments in GaAs quantum wells. (a) Undoped sample at excitation density of $5 \times 10^{11} \text{ cm}^{-2}$. (b) Sample with n-modulation doping of $3 \times 10^{11} \text{ cm}^{-2}$, excited with density of $3 \times 10^{11} \text{ cm}^{-2}$. (c) Sample with n-modulation doping of $3 \times 10^{11} \text{ cm}^{-2}$, excited with density of $3 \times 10^{11} \text{ cm}^{-2}$. The excitation energy had about 20meV above edge of ground subband. (quoted from Phys. Rev. Lett. **61**, 1290 (1988))

electron on the non-equilibrium carrier's evolution can be divided into that on the unscreened carrier's evolution and the screening strength. By the benefit, one can demonstrate the difference of screening strength caused by the non-equilibrium and the cold carriers. The Knox's result¹¹ is in a very short time scale so that the memory effect is important. The memory effect leading to a faster carrier's evolution is similar to the result¹¹. Nevertheless, the 2D cold electron is not shown to cause a significant difference and the carrier is also not shown to reach the thermalization in a less than 10fs time scale.

2.2 Quantum Kinetic Equation

In this section, we introduce the derivation and approximations of scattering term. By using the close-time-path non-equilibrium Green function, the Dyson equation can be extended to the generalized Kadanoff-Baym equation¹³ (GKBE). The GKBE was chosen as the quantum kinetic equation in the investigation. A non-equilibrium carrier's distribution is generated on the band structures and the carrier's evolution via the electron-electron interaction can be obtained by solving the equation. Because the femtosecond scale is concerned, the carrier-phonon and other scatterings were omitted. The electron-hole interaction was also not considered because their different Bloch functions lead a lower scattering rate than that of electron-electron interaction. Generalized Kadanoff-Baym Ansatz¹⁴ (GKBA) was used to simplify the memorial integral of scattering term and the random phase approximation¹⁵ (RPA) was to the screening behavior. The scattering terms were strictly derived in the distinct dimensions and the 2D formulations (including the scattering term and RPA dielectric function) are firstly demonstrated in the thesis. The carrier's distribution can be in terms of equal-time lesser Green function ($f_{\mathbf{k}}(t) = -i\hbar G_{\mathbf{k}}^<(t, t)$). In the GKBE, the scattering term of k-state particle can be written as¹⁶

$$\left. \frac{\partial f_{\mathbf{k}}(t)}{\partial t} \right|_{\text{scatt.}} = - \int_{-\infty}^t dt' \left[\Sigma_{\mathbf{k}}^{>}(t, t') G_{\mathbf{k}}^{<}(t', t) - \Sigma_{\mathbf{k}}^{<}(t, t') G_{\mathbf{k}}^{>}(t', t) - G_{\mathbf{k}}^{>}(t, t') \Sigma_{\mathbf{k}}^{<}(t', t) + G_{\mathbf{k}}^{<}(t, t') \Sigma_{\mathbf{k}}^{>}(t', t) \right] \quad (2.2)$$

where $G_{\mathbf{k}}^{>(<)}(t, t')$ and $\Sigma_{\mathbf{k}}^{>(<)}(t, t')$ denote a greater (lesser) two-time Green function and a Coulomb scattering self energy. By using the analytic continuation¹⁷, the Coulomb scattering self energy in the RPA can be rearranged as¹⁶

$$\Sigma_{\mathbf{k}}^{>(<)}(t, t') = 2\hbar^2 \sum_{\mathbf{q}, \mathbf{k}'} G_{\mathbf{k}-\mathbf{q}}^{>(<)}(t, t') \int_{-\infty}^t dt_1 \int_{-\infty}^{t_1} dt_2 V_{s, \mathbf{q}}^r(t, t_1) (V_{s, \mathbf{q}}^r(t', t_2))^* G_{\mathbf{k}+\mathbf{q}}^{>(<)}(t_1, t_2) G_{\mathbf{k}}^{<(>)}(t_2, t_1) \quad (2.3)$$

where $V_{s, \mathbf{q}}^r(t, t_1)$ represents a retarded shielding potential. Before the screening builds up, the shielding potential is given by $V_{\mathbf{q}}\delta(t-t_1)$, where $V_{\mathbf{q}}$ denotes the Coulomb interaction in Fourier space. The shielding potential almost takes a plasma forming time to build up⁵. In the calculation, the screening was assumed to be built up instantaneously because it can significantly shorten the simulating time but not change the dependence of screening strength on the sample's dimension. The retarded shielding potential¹⁸ was modeled by $V_{\mathbf{q}}\delta(t-t_1)/\epsilon_{\text{RPA}}(\mathbf{q}, \omega)$, where $\epsilon_{\text{RPA}}(\mathbf{q}, \omega)$ denotes the RPA dielectric function.

Substitute the Coulomb scattering self energy into the eq.(2.2), after an algebraic arrangement by using the GKBA, the scattering term can be written as¹⁶

$$\begin{aligned} \frac{\partial f_{\mathbf{k}}(t)}{\partial t} = & -\frac{4}{\hbar^2} \sum_{\mathbf{q}, \mathbf{k}'} \int_{-\infty}^t dt' V_{s, \mathbf{q}}(t) V_{s, \mathbf{q}}(t') \cos\left[\frac{\Delta}{\hbar}(t-t')\right] e^{-\frac{\Gamma}{\hbar}(t-t')} \\ & \times \left\{ f_{\mathbf{k}}(t') f_{\mathbf{k}'}(t') [1-f_{\mathbf{k}-\mathbf{q}}(t')] [1-f_{\mathbf{k}+\mathbf{q}}(t')] - [1-f_{\mathbf{k}}(t')] [1-f_{\mathbf{k}'}(t')] f_{\mathbf{k}-\mathbf{q}}(t') f_{\mathbf{k}'+\mathbf{q}}(t') \right\} \end{aligned} \quad (2.4)$$

where Δ denotes the non-conserving energy and Γ denotes the dephasing factor.

Change the notation of \mathbf{k} , \mathbf{k}' , $\mathbf{k}-\mathbf{q}$, and $\mathbf{k}'+\mathbf{q}$ by \mathbf{k}_1 , \mathbf{k}_2 , \mathbf{k}_3 , and \mathbf{k}_4 , respectively, and

derive the scattering terms in distinct dimensions that with screening can be shown as

$$\begin{aligned}
\left. \frac{\partial f_{k_1}(t)}{\partial t} \right|_{2D} &= -\frac{m_e e^4}{\pi^4 \hbar^4 k_1 \epsilon_\infty^2} \int_{-\infty}^t dt' \int_0^\infty dk_3 \int_{|k_1-k_3|}^{k_1+k_3} \frac{dq}{q^2} \int_0^\infty dk_2 \int_{\Delta_{\min}}^{\Delta_{\max}} d\Delta \\
&\quad \times \frac{1}{\left| \epsilon_{\text{RPA}}^{2D}(\mathbf{q}, \omega, t') \right|^2} \frac{\cos\left(\frac{\Delta}{\hbar}(t-t')\right) e^{-\frac{\Gamma}{\hbar}(t-t')}}{\sqrt{1 - \left(\frac{k_1^2 + k_3^2 - q^2}{2k_1 k_3} \right)^2} \sqrt{1 - \left(\frac{k_1^2 - k_3^2 - q^2 - \frac{2m_e \Delta}{\hbar^2}}{2qk_2} \right)^2}} \\
&\quad \times \left\{ f_{k_1}(t') f_{k_2}(t') [1 - f_{k_3}(t')] [1 - f_{k_4}(t')] - [1 - f_{k_1}(t')] [1 - f_{k_2}(t')] f_{k_3}(t') f_{k_4}(t') \right\} \\
\left. \frac{\partial f_{k_1}(t)}{\partial t} \right|_{3D} &= -\frac{m_e e^4}{\pi^4 \hbar^4 k_1 \epsilon_\infty^2} \int_{-\infty}^t dt' \int_0^\infty k_3 dk_3 \int_{|k_1-k_3|}^{k_1+k_3} \frac{dq}{q^4} \int_0^\infty k_2 dk_2 \int_{\Delta_{\min}}^{\Delta_{\max}} d\Delta \frac{1}{\left| \epsilon_{\text{RPA}}^{3D}(\mathbf{q}, \omega, t') \right|^2} \cos\left(\frac{\Delta}{\hbar}(t-t')\right) \\
&\quad \times e^{-\frac{\Gamma}{\hbar}(t-t')} \left\{ f_{k_1}(t') f_{k_2}(t') [1 - f_{k_3}(t')] [1 - f_{k_4}(t')] - [1 - f_{k_1}(t')] [1 - f_{k_2}(t')] f_{k_3}(t') f_{k_4}(t') \right\}
\end{aligned}$$

where the parabolic band is used. The unscreened scattering term is the formulation

without the $\left| \epsilon_{\text{RPA}}^{2D,3D}(\mathbf{q}, \omega, t') \right|^{-2}$. Δ_{\max} and Δ_{\min} denote the maximum and m (2.5a)

non-conserving energy and are equal to $\frac{\hbar^2 k_1^2}{2m_e} + \frac{\hbar^2 k_2^2}{2m_e} - \frac{\hbar^2 k_3^2}{2m_e} - \frac{\hbar^2}{2m_e} (q - k_2)^2$ and

$\frac{\hbar^2 k_1^2}{2m_e} + \frac{\hbar^2 k_2^2}{2m_e} - \frac{\hbar^2 k_3^2}{2m_e} - \frac{\hbar^2}{2m_e} (q + k_2)^2$. The form factor in 2D term is set to be unity¹⁹.

The RPA dielectric functions in distinct dimensions can be expressed as

(2.5b)

$$\begin{aligned}
\epsilon_{\text{RPA}}^{2D}(\mathbf{q}, \omega, t') &= 1 + \frac{m_e e^2}{2\pi^2 \hbar^2 q^2 \epsilon_\infty} \int_0^\infty dk f_k(t') \oint_{|z|=1} idz \\
&\quad \times \left[z - \frac{1}{\beta} \left((\hbar\omega + E_q) + i\delta + \sqrt{(\hbar\omega + E_q)^2 - \delta^2 - \beta^2 + 2i\delta(\hbar\omega + E_q)} \right) \right]^{-1} \\
&\quad \times \left[z - \frac{1}{\beta} \left((\hbar\omega + E_q) + i\delta - \sqrt{(\hbar\omega + E_q)^2 - \delta^2 - \beta^2 + 2i\delta(\hbar\omega + E_q)} \right) \right]^{-1} \\
&\quad - \left[z - \frac{1}{\beta} \left((\hbar\omega - E_q) + i\delta + \sqrt{(\hbar\omega - E_q)^2 - \delta^2 - \beta^2 + 2i\delta(\hbar\omega - E_q)} \right) \right]^{-1} \\
&\quad \times \left[z - \frac{1}{\beta} \left((\hbar\omega - E_q) + i\delta - \sqrt{(\hbar\omega - E_q)^2 - \delta^2 - \beta^2 + 2i\delta(\hbar\omega - E_q)} \right) \right]^{-1} \quad (2.6a)
\end{aligned}$$

$$\epsilon_{\text{RPA}}^{3D}(\mathbf{q}, \omega, t') = 1 + \frac{m_e e^2}{2\pi^2 \hbar^2 q^3 \epsilon_\infty} \int_0^\infty k dk f_k(t') \ln \left[\frac{(E_q + \beta/2 - \hbar\omega - i\delta)(E_q + \beta/2 + \hbar\omega + i\delta)}{(E_q - \beta/2 - \hbar\omega - i\delta)(E_q - \beta/2 + \hbar\omega + i\delta)} \right] \quad (2.6b)$$

where ω denotes the oscillating frequency of dynamical screening and is equal to $\frac{\hbar^2 k_1^2}{2m_e} - \frac{\hbar^2 k_3^2}{2m_e} - \Delta$. E_q and β are $\frac{\hbar^2 q^2}{2m_e}$ and $\frac{\hbar^2 kq}{m_e}$, respectively.

2.3 Results and Discussion

In the investigation, the parameters of GaAs were taken from the Adachi's report²⁰ and the structure of a quantum well was chosen as a 10-nm well width (L_w) and 0.3 Al fractions. The initial carrier's distribution was the Gaussian function with a center of 25meV above the ground state and a full width half maximum (FWHM) of 15meV around the center. Before the carrier exchanges the energy with phonons, the lattice temperature of 15K was used. 0.8 Rydberg energy⁵ was used for the dephasing factor. Partial scattering terms were integrated by using the Gaussian quadratures²¹. The calculation was performed on the momentum space but the result will change to the electron's energy in the plots.

2.3.1 2D versus 3D Dynamical Screening

Fig. 2.5(a) and 2.5(b) show the 2D and 3D GKBE solutions at the carrier density of $8 \times 10^{10} \text{cm}^{-2}$ and $8 \times 10^{16} \text{cm}^{-3}$, respectively. Distinct colors represent different delayed times. Solid and dash curves denote the screened and unscreened results, respectively. At the beginning, a non-thermal carrier's distribution is generated and carriers start to scatter with each other. The unscreened carrier's evolution is faster than the screened one. Their difference is enlarged as the time evolves and is more considerable in a quantum well. Thus, the screening dependence is verified and can be understood in a simple picture. In a 2D structure, due to a stronger confinement, the electric field is larger than that in a 3D structure and the stronger dynamical screening is as a result of larger difference between the unscreened and screened electric fields. The screening

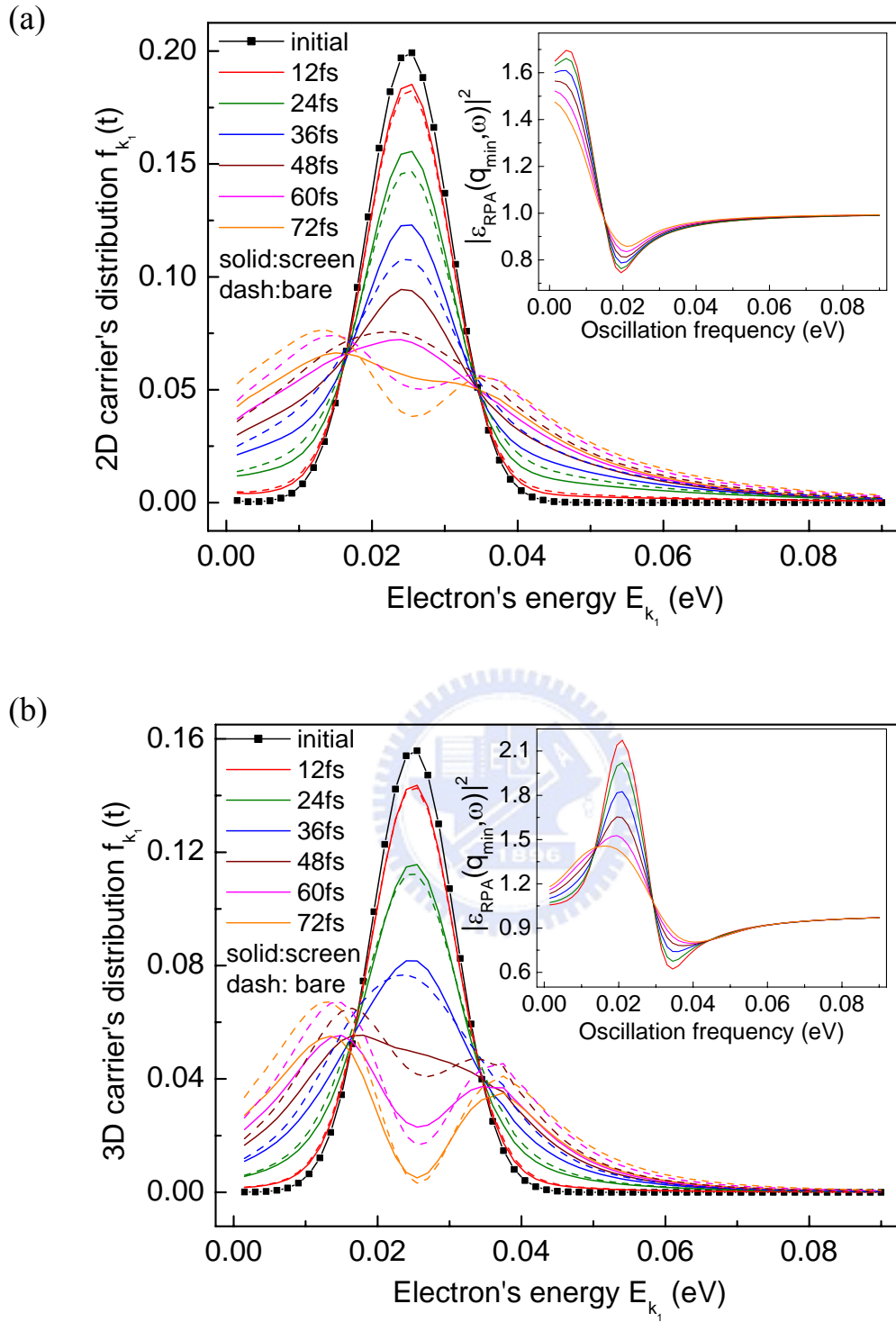


Figure 2.5: GKBE solutions for the screened and the unscreened (bare) non-equilibrium CCS. (a) in a 10nm-width GaAa/Al_{0.3}Ga_{0.7}As quantum well at the non-equilibrium density of $8 \times 10^{10} \text{ cm}^{-2}$. (b) in bulk GaAs at the non-equilibrium density of $8 \times 10^{16} \text{ cm}^{-3}$. The initial distribution was modeled by the Gaussian function with the center of 25meV above the ground state and the FWHM of 15meV around the center. Inset figures show the transient screening strength at the minimum wave vector q_{min} of CCS.

strength is shown in the inset figure where a larger magnitude around the center of non-equilibrium carrier's distribution in 2D than 3D structures is demonstrated. Although the (unscreened and screened) electric field is weaker in a bulk than a quantum well (respectively), the carrier in a higher dimension has a larger density of states so that the scattering rate becomes larger and the carrier has a faster evolution. The dependence is in good agreement with the experiment where the photon-echo dephasing time is shorter in a bulk^{2,3}. In addition, the distinct density of states causes an increased and a flat scattering rate with an increased carrier's energy in a bulk and a quantum well respectively so that the former has a quick scattering to the lower energy state while the later has a uniformly spreading distribution along the energy.

2.3.2 Quantum Coherence on Carrier's Evolution

Because the carrier's quantum coherence breaks the Markovian approximation, the past carrier's distribution is taken into account the scattering so that the carrier's evolution has the memory effect. The scattering rate is enhanced at the early stage. As the time evolves, the enhancement becomes energy dependent so that a burning hole is demonstrated on the carrier's distribution. The memory effect can give a reasonable explanation for the contradiction of power laws of photon-echo dephasing time²⁻⁴. Fig. 2.6(a) and 2.6(b) show the 2D and 3D screened GKBE solutions at 90fs and 60fs for the density from 10^{10}cm^{-2} to 10^{11}cm^{-2} and 10^{16}cm^{-3} to 10^{17}cm^{-3} , respectively. Inset figure shows the Boltzmann solution. The average relaxation time is defined by $\frac{\Delta t}{\Delta f_{k_1}}$, where Δf_{k_1} is the difference of occupations at 25meV in a time interval Δt . Changing n_{2D} to n_{2D}/L_w , the relaxation time is shown in Fig. 2.7. The density dependence in distinct regimes is quite different. In the Boltzman regime, it is slightly stronger in a quantum well than a bulk and is in consistent with the experimental

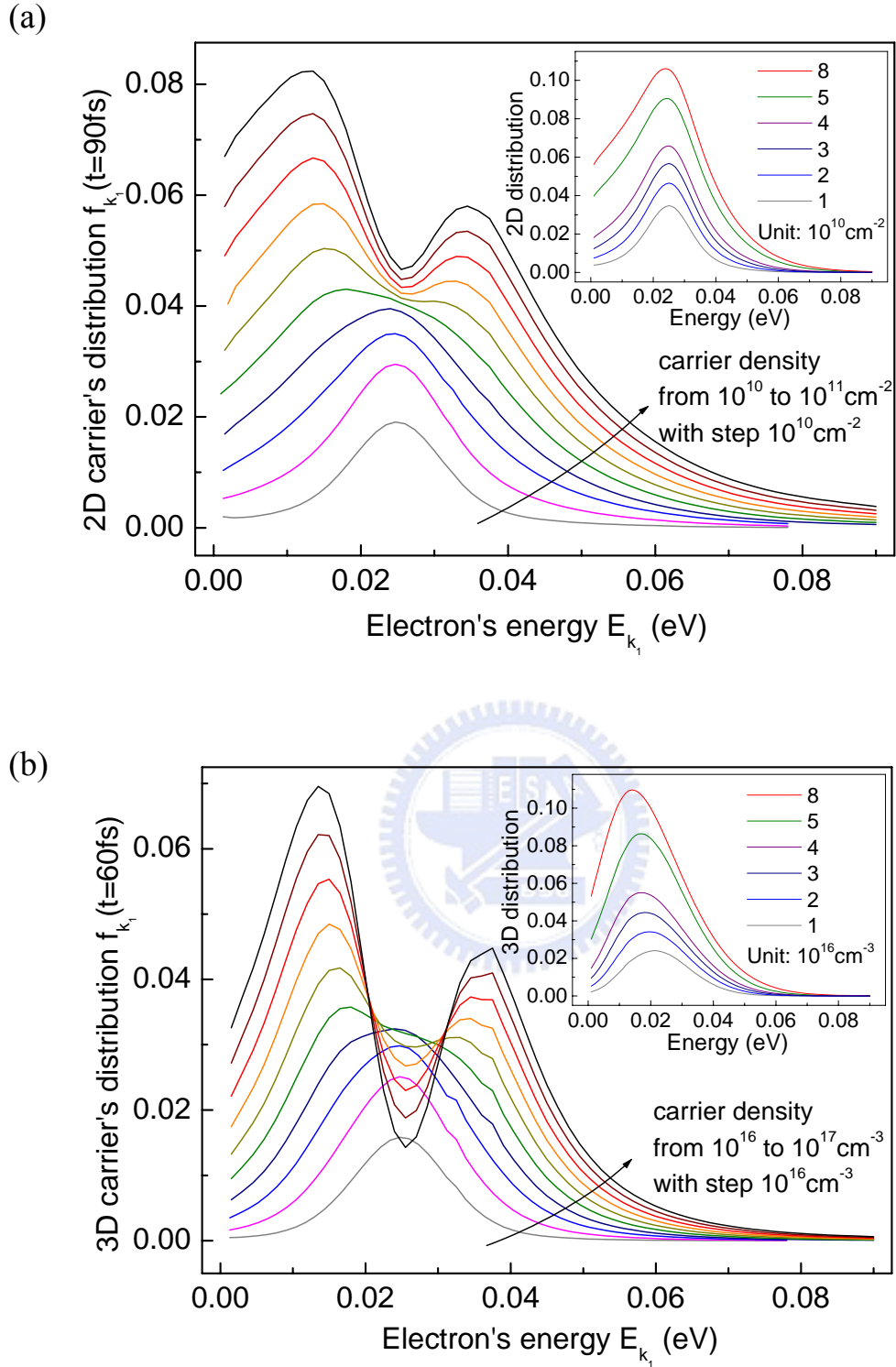


Figure 2.6: GKBE solutions for the screened CCS at distinct non-equilibrium densities. (a) in a 10nm-width GaAs/Al_{0.3}Ga_{0.7}As quantum well at the delayed time of 90fs. (b) in bulk GaAs at the delayed time of 60fs. Inset figures show the Boltzmann solutions. The center and the FWHM of initial Gaussian distribution are 25meV and 15meV, respectively.

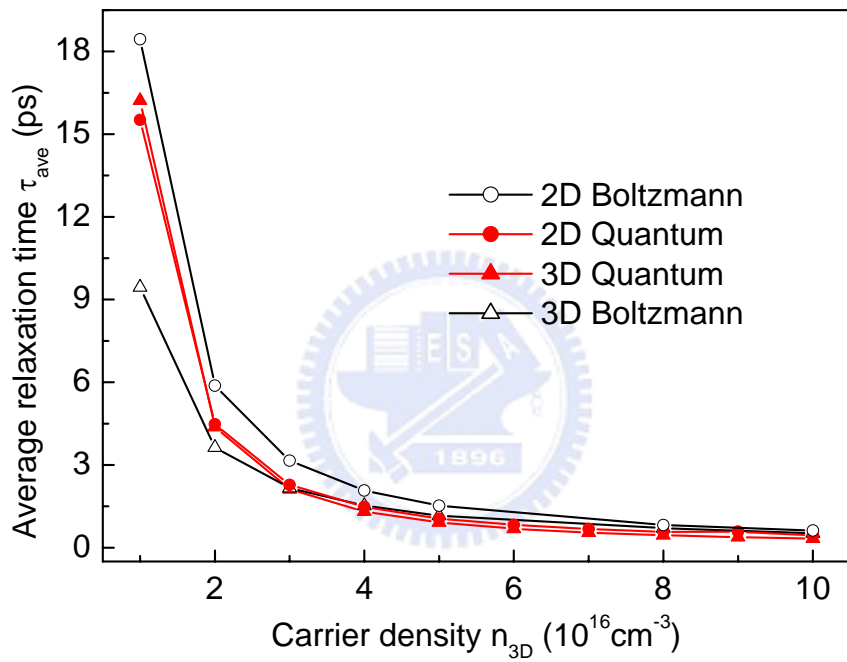


Figure 2.7: Comparison of 2D and 3D average relaxation times as a function of the non-equilibrium carrier density between the quantum and the Boltzmann kinetic regimes. The results were extracted from the Fig. 2.6. The sheet density in a quantum well was converted to the volume density by dividing the L_w of 10nm.

power law of $n^{-\frac{1}{D}}$. The power law also can be obtained by using the estimation of average interparticle distance^{2,3} and a strict derivation in the Boltzmann theory²². Thus, the earlier experimental result^{2,3} should be valid and was measured from a dephasing non-equilibrium carrier. In the quantum regime, the dependence in the two sample's structures becomes almost indistinguishable and is in surprisingly good agreement with the report⁴. Although the semiconductor Bloch equation was used there⁴, the two theoretical approaches give the same dependence. Thus, the experiment result⁴ should be measured from a coherent non-equilibrium carrier and the memory effect is the reason for the change of power law from the Boltzmann to the quantum regimes.

2.3.3 Scattering among Dense Fermi Sea

Fig. 2.8(a) shows the 2D GKBE solution at the density of $8 \times 10^{10} \text{ cm}^{-2}$, where 55% is partitioned to the non-equilibrium carrier and 45% is to a 100K electron's background. Fig. 2.8(b) shows the Boltzmann solution. In the absent screening, the carrier's evolution is shown to evolve as normal as that with the non-equilibrium carrier alone. The non-equilibrium carrier has a weak interaction with the cold electron because their exchanged wave vector is large. Thus, the non-equilibrium carrier has a very slow scattering to the cold electron and most scattering among the non-equilibrium carrier is due to itself. Comparing the Fig. 2.8(a) and 2.5(a), the screening strength caused by the 2D cold electron is shown to have a very small difference from that caused by the non-equilibrium carrier although their dielectric functions are a little different. Thus, the effect of 2D cold electron can be rule out from the possibility of Knox's result. The memory effect leads the carrier with a faster scattering rate and a shorter thermalization time as compared to the Boltzmann solution. Nevertheless, the thermalization is not shown to become so rapid in a less than 10fs time scale. In addition, this is independent of the 2D cold electron. Thus, the

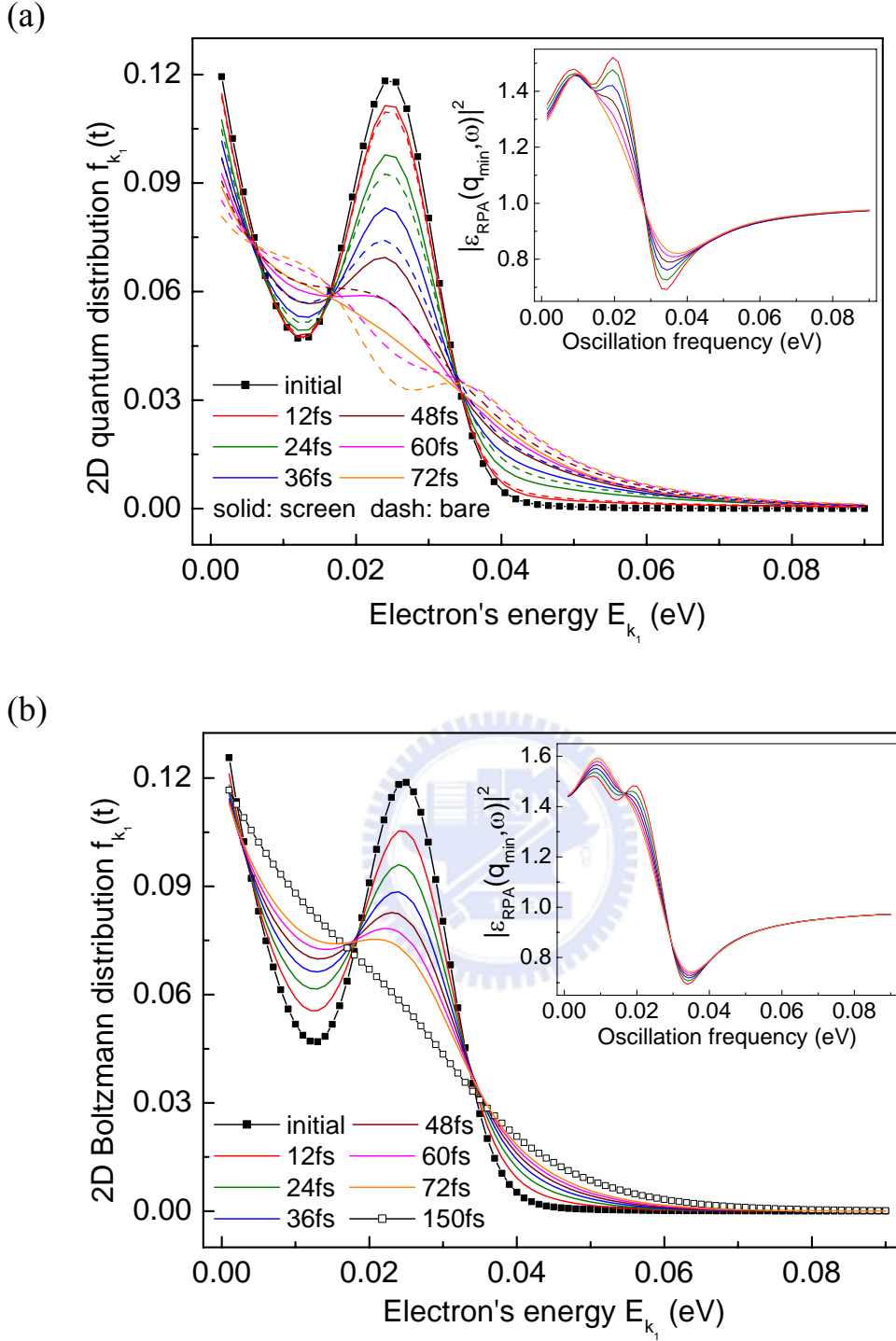


Figure 2.8: Time evolution of non-equilibrium carrier among a 100K electron's background in a 10nm-width GaAa/Al_{0.3}Ga_{0.7}As quantum well. (a) GKBE solution. (b) Boltzmann solution. The non-equilibrium and the cold electron's densities are $0.55 \times 8 \times 10^{10} \text{ cm}^{-2}$ and $0.45 \times 8 \times 10^{10} \text{ cm}^{-2}$, respectively. Inset plots show the screening strength at the minimum wave vector q_{\min} . The center and the FWHM of initial Gaussian distribution are 25meV and 15meV, respectively.

memory effect also can be ruled out. In the earlier experiment¹¹, the 2D cold carrier is generated from the modulation dopants in the barrier, where Si and Be were used as the n-type and p-type dopants. The ionized impurities would build an electric field so that increases the scattering rate. Because the Si has electrons in orbit ($Z=14$) three times more than the Be ($Z=4$), the building electric field of Si enhances the scattering more considerably. After ruling out all possibilities, the rapid thermalization in the presence of 2D cold electron should be due to the electric field induced from barrier's modulation dopants.

2.4 Summary

Although the dynamical screening on the CCS is a complex Coulomb interaction, the dimensional dependence can be understood in a simple picture and the picture is also valid on the Fröhlich interaction and the static-screened interaction. The memory effect is as a result of quantum coherence and would cause a burning hole on the carrier's distribution at the early stage. As the time further goes, the two hills aside the burning hole is expected to continue to evolve to two burning holes and three hills due to the memory effect and go on until the carrier dephases or thermalizes. The non-equilibrium carrier's evolution is normal in the presence of 2D cold electron and the Knox's result should be due to the effect of wafer's preparation.

References

1. J. Shah, *Ultrafast Spectroscopy of Semiconductors and Semiconductor Nanostructures* (Springer, Berlin, 1996).
2. J. -Y. Bigot, M. T. Portella, R. W. Schoenlein, J. E. Cunningham, and C. V. Shank, *Phys. Rev. Lett.* **67**, 636 (1991).
3. P. C. Becker, H. L. Fragnito, C. H. Brito Cruz, R. L. Fork, J. E. Cunningham, J. E. Henry, and C. V. Shank, *Phys. Rev. Lett.* **61**, 1647 (1988).
4. B. Mieck, H. Haug, W. A. Hügel, M. F. Heinrich, and M. Wegener, *Phys. Rev. B* **62**, 2686 (2000).
5. K. El Sayed, S. Schuster, H. Haug, F. Herzel, and K. Henneberger, *Phys. Rev. B* **49**, 7337 (1994).
6. H. C. Lee, K. W. Sun, and C. P. Lee, *Solid State Comm.* **128**, 245 (2003).
7. K. El Sayed, L. Bányai, and H. Haug, *Phys. Rev. B* **50**, 1541 (1994).
8. M. Betz, G. Göger, A. Laubereau, P. Gartner, L. Bányai, H. Haug, K. Ortner, C. R. Becker, and A. Leitenstorfer, *Phys. Rev. Lett.* **86**, 4684 (2001).
9. C. Fürst, A. Leitenstorfer, A. Laubereau, and R. Zimmermann, *Phys. Rev. Lett.* **78**, 3733 (1997).
10. L. Bányai, D. B. Tran Thoai, E. Reitsamer, H. Haug, D. Steinbach, M. U. Wehner, M. Wegener, T. Marschner and W. Stolz, *Phys. Rev. Lett.* **75**, 2188 (1995).
11. W. H. Knox, D. S. Chemla, G. Livescu, J. E. Cunningham, and J. E. Henry, *Phys. Rev. Lett.* **61**, 1290 (1988).
12. M. G. Kane, *Phys. Rev. B* **54**, 16345 (1996) and *Carrier-Carrier Scattering among Photoexcited Nonequilibrium Carriers in GaAs* (Dissertation of Princeton University, 1994).
13. L. P. Kadanoff and G. Baym, *Quantum Statistical Mechanics* (Benjamin, New

Tork, 1962).

14. P. Lipavský, V. Špička, and B. Velický, Phys. Rev. B **34**, 6933 (1986).
15. G. Mahan, “Many Particle Physics” (Plenum, New York, 2000).
16. H. Haug and A. -P Jauho, Quantum Kinetics in Transport and Optics of Semiconductors, 2nd ed. (Springer, Berlin, 1998).
17. D. C. Langreth, Linear and Nonlinear Electron Transport in Solids, ed. By J. T. Devreese and E. Van Doren (Plenum, New York, 1976).
18. L. Bányai, Q. T. Vu, B. Mieck, and H. Haug, Phys. Rev. Lett. **81**, 882 (1998).
19. The form factor is given by

$$F_{ijmn}(q) = \int_{-\infty}^{\infty} dz \int_{-\infty}^{\infty} dz' \varphi_i(z) \varphi_j(z') \varphi_m^*(z) \varphi_n^*(z') e^{-q|z-z'|}$$

where $\varphi(z)$ denotes the electron's wave function and lower subscript indicates the subband of initial and final states. The form factor of intrasubband scattering in the ground state can be expressed as

$$F_{1111}(q) = \frac{8}{(qL_w)^2 + (2\pi)^2} \left[\frac{\pi^2}{qL_w} - \frac{4\pi^4(1 - e^{-qL_w})}{(qL_w)^2 [(qL_w)^2 + (2\pi)^2]} + \frac{1}{2} qL_w \right]$$

20. S. Adachi, J. Appl. Phys. **58**, R1 (1985).
21. M. Abramowitz and A. Stegun, Handbook of Mathematical Functions, p.916, 917 (Dover, New York, 1964).
22. D. W. Snoke, Phys. Rev. B **50**, 11583 (1994).

Chapter 3

Hot Carrier Relaxation

3.1 Introduction

Although hot carrier relaxations in a bulk GaAs and quantum wells have been studied experimentally¹⁻¹¹ and theoretically¹²⁻¹⁴ for more than one decade, the dependence of the dynamical screening in hot carrier relaxations on the sample's dimensionality is still not well understood. The screening behavior caught less attention on hot carrier relaxations in GaAs probably attributes that the hot phonon effect was primarily considered to be responsible for the great drop of energy-loss rates via Fröhlich interaction^{2,5,11}, and hot carrier relaxations seem not to depend on the dimensionality experimentally^{4,5,6}. However, the deduction could not hold on the overall carrier densities. Because more recent experimental results indicated that there is a clear difference in energy-loss rates between a bulk GaAs and quantum wells when the carrier density is above a certain critical value^{7,8,9}, shown in Fig. 3.1 and 3.2. Though the critical carrier densities determined in those experiments are not consistent, the results imply that the dimensionality and the dynamical screening may have a significant effect on hot carrier relaxations in a bulk GaAs and quantum wells.

To theoretically study the difference of hot carrier relaxations between the two different dimensional systems, it is important to consider the optical phonon modes in a quantum well. Many improved models were developed to give a better description for atomic vibrations and the interaction Hamiltonians with electrons in the quasi two-dimensional structure¹⁵⁻²⁶. In our calculations, we use the dielectric continuum

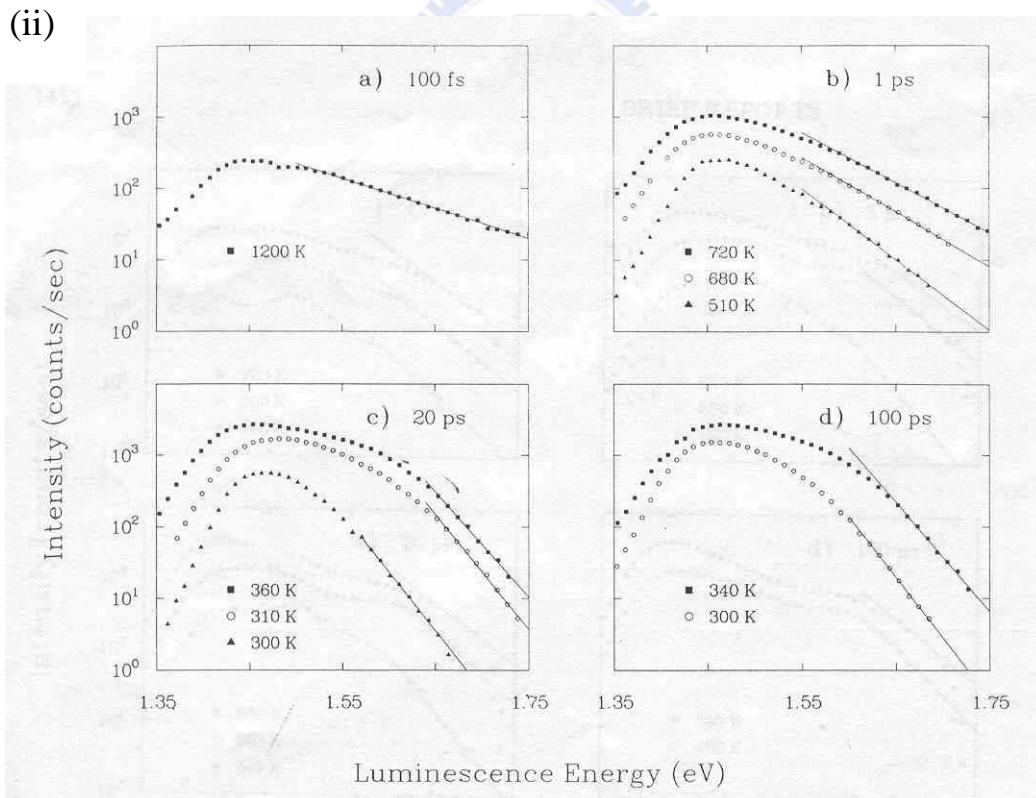
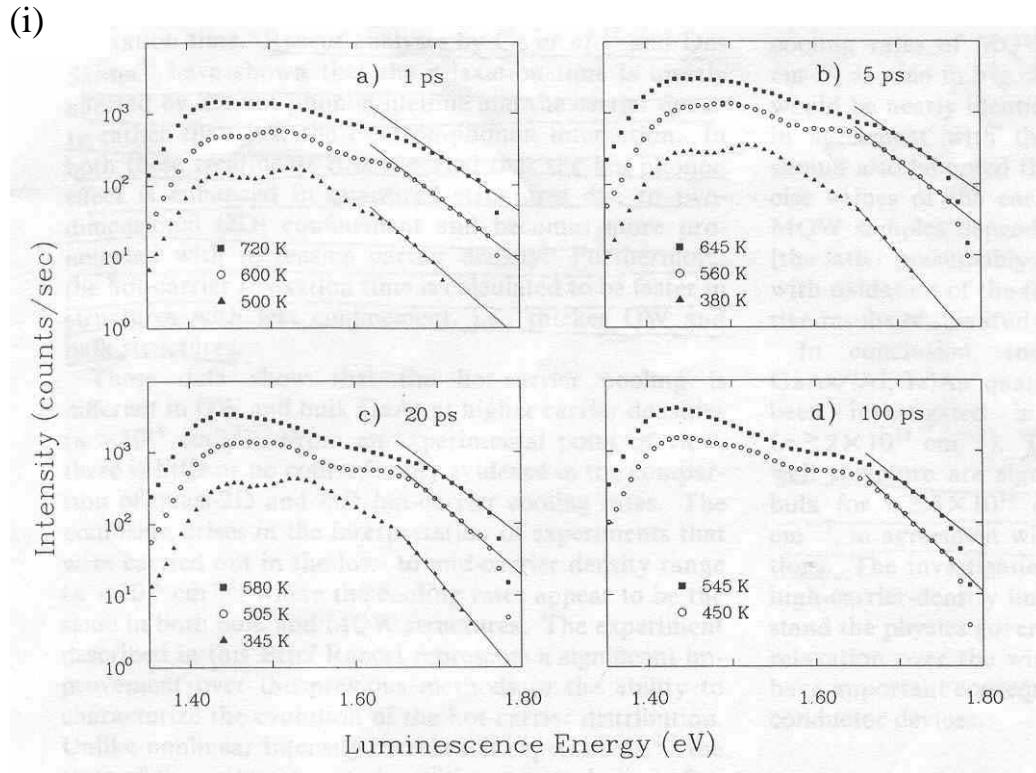


Figure 3.1: Time-resolved luminescence spectra at room temperature from Pelouch's results. (i) for 400nm bulk GaAs. (ii) for multiple quantum well. square: 10^{19}cm^{-3} ; circle: $5 \times 10^{18}\text{cm}^{-3}$; triangles: $2 \times 10^{18}\text{cm}^{-3}$ (quoted from Phys. Rev. B **45**, 1450 (1992))

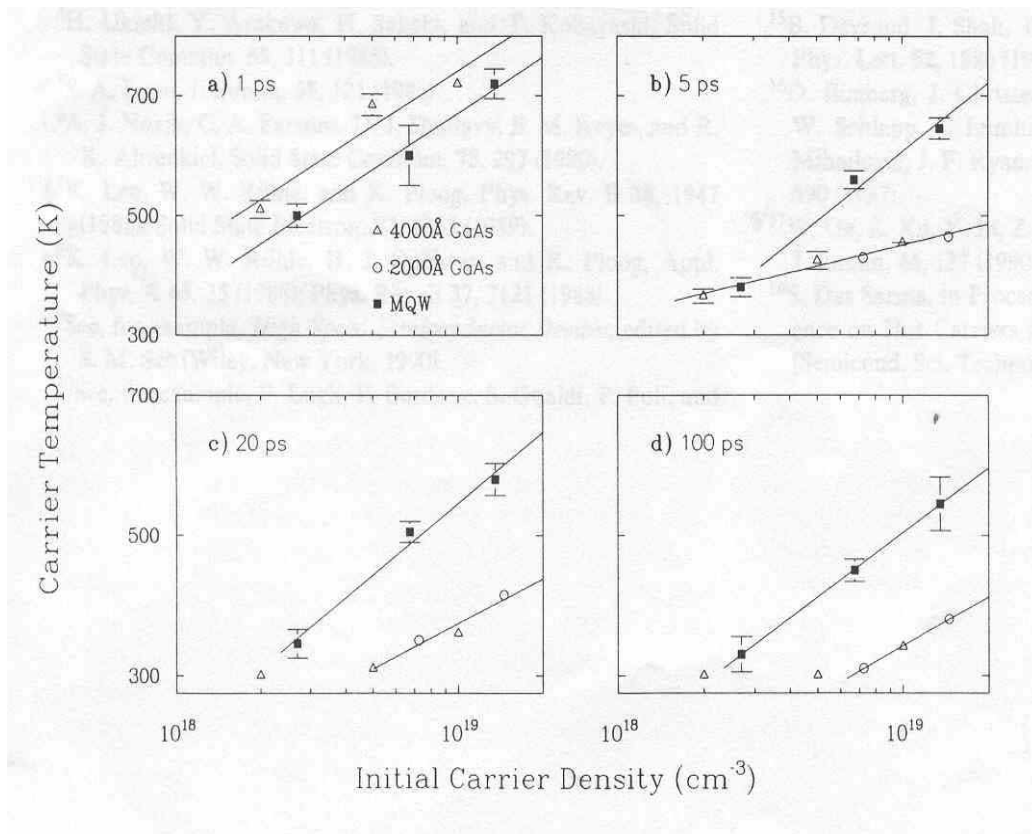


Figure 3.2: Comparison of carrier temperature versus initial carrier density between different sample's structures. (quoted from Phys. Rev. B **45**, 1450 (1992))

model^{15-17,20} (DCM) because the model has provided a good agreement with many earlier experimental results²⁷⁻³³. Although the interaction Hamiltonians of phonon modes in a quantum well are strongly dependent on the well width, many experimental results^{4,5,6} demonstrated the less well-width dependence of hot carrier relaxations except few report shown the contrary results^{34,35}. This discrepancy also stimulates us to study the structural dependence of energy-loss rates in a quantum well.

In the thesis, the significance of the dimensionality and the dynamical screening on hot carrier relaxations in a bulk GaAs and quantum wells is investigated. The distinct dimensionality and the dynamical screening indeed cause that hot carriers in quantum wells relax significantly slower than that in a bulk GaAs above the critical carrier density of $2 \times 10^{18} \text{cm}^{-3}$. We attribute this to the smaller density of state in quantum wells and the strong 2D dynamical screening. The dynamical screening in quantum wells appears to be much stronger than that in the bulk and considerable as compared to the hot phonon effect. The critical carrier density determined in our studied is in very good agreement with the earlier experiments of Pelouch and co-researchers⁷. We also found that the average energy-loss rate in quantum wells depends on the well width more appreciably when Al compositions are high.

3.2 Semiclassical Boltzmann Equation

The average energy-loss rate (AELR) is calculated in order to compare the difference of hot carrier relaxations between the two different dimensional systems. In this section, we describe the derivations of the AELR in a bulk GaAs and a quantum well where the net phonon generation rate, and the treatments of hot phonon effect and the dynamical screening are included. The dynamical screening is dealt with the RPA³⁶. Exact dimensional treatments are handled on the AELR's derivations and the

dynamical screenings. In our calculations, the electron-phonon scattering is through Fröhlich interaction and only intrasubband scattering is considered in the calculation of the AELR in quantum wells. The hole-phonon interaction is neglected. The plasmon-phonon coupling (PPC) is not considered here because the significant enhancement of energy-loss rates^{37,38} induced by the PPC does not appear above the critical carrier density of $2 \times 10^{18} \text{ cm}^{-3}$.

The AELR is determined by the net phonon generation rate and the phonon energy. The net phonon generation rate represents the subtracting difference between phonon's generation rates and absorption rates. In a bulk GaAs, the 3D net phonon generation rate is given by³⁹

$$\frac{\partial N_{\mathbf{q}}}{\partial t} = \frac{m_e^2 k_B T_C V}{\pi \hbar^5 q} |M_{\mathbf{q}}|^2 [N_{\mathbf{q}}(T_C) - N_{\mathbf{q}}] \int_{\zeta_{\min}}^{\infty} \left[f(\zeta) - f\left(\zeta + \frac{\hbar \omega_{\mathbf{q}}}{k_B T_C}\right) \right] d\zeta \quad (3.1)$$

where \mathbf{q} and $\omega_{\mathbf{q}}$ denote phonon's wave vector and phonon's energy, respectively. $f(\zeta)$ is the electron's distribution. With the thermalized assumption for carriers, Fermi-Dirac distribution is used where T_C is the carrier temperature. $N_{\mathbf{q}}$ represents phonon population. k_B and V have their usual meanings. The quantity $N_{\mathbf{q}}(T_C)$ can be written as³⁹

$$N_{\mathbf{q}}(T_C) = \frac{1}{\exp\left(\frac{\hbar \omega_{\mathbf{q}}}{k_B T_C}\right) - 1} \quad (3.2)$$

ζ , a dimensionless quantity, represents the normalized energy (energy divided by thermal energy $k_B T_C$). ζ_{\min} is the minimum normalized energy required for an electron to kick out a phonon of wave vector. It is given by³⁹

$$\zeta_{\min} = \frac{m_e}{2\hbar^2 q^2 k_B T_C} \left| \frac{\hbar^2 q^2}{2m_e} - \hbar \omega_{\mathbf{q}} \right|^2 \quad (3.3)$$

$|M_{\mathbf{q}}|^2$, Fröhlich interaction strength, is given by³⁹

$$|M_{\mathbf{q}}|^2 = \frac{e^2 \hbar \omega_{\mathbf{q}}}{2Vq^2} \left(\frac{1}{\epsilon_{\infty}} - \frac{1}{\epsilon_S} \right) \quad (3.4)$$

where ϵ_{∞} and ϵ_S are high frequency and static dielectric constants.

In a quantum well, based on the DCM^{15-17,20}, the confined (C), the symmetric plus interface (S+), symmetric minus (S-) interface and the half-space (HS) phonon modes are considered in our calculations. Anti-symmetric interface modes are excluded due to the selection rule for the intra-subband scattering. The dispersion relations for the S+ and the S- interface modes are shown in the sec. 5.2⁴⁰. The noun “half-space” in double heterojunctions originates from the report of Mori and Ando²⁰ where the same name as the case of a single heterojunction is used. The 2D net phonon generation rate can be written as

$$\frac{\partial N_{\mathbf{q}_{//}}^{(C,S\pm,HS)}}{\partial t} = \frac{\sqrt{2m_{en}^3 k_B T_C A}}{\pi \hbar^4 q_{//}} \left| M_{\mathbf{q}_{//}}^{(C,S\pm,HS)} \right|^2 \left[N_{\mathbf{q}_{//}}^{(C,S\pm,HS)}(T_C) - N_{\mathbf{q}_{//}}^{(C,S\pm,HS)} \right] \times \int_{\zeta_{\min}}^{\infty} \frac{1}{\sqrt{\zeta}} \left[f(\zeta + \zeta_1) - f\left(\zeta + \zeta_1 + \frac{\hbar \omega_{\mathbf{q}_{//}}^{(C,S\pm,HS)}}{k_B T_C}\right) \right] d\zeta \quad (3.5)$$

where $\mathbf{q}_{//}$ and $\omega_{\mathbf{q}_{//}}^{(C,S\pm,HS)}$ denote the in-plane phonon wave vector and the phonon energies of various modes. m_{en} is the n^{th} layer effective electron’s mass while 1 represents GaAs and 2 represents AlGaAs layers. A denotes the area. ζ_1 is the normalized ground state energy to the thermal energy. $\left| M_{\mathbf{q}_{//}}^{(C,S\pm,HS)} \right|^2$ represents the electron-phonon interaction strength of various modes shown in Table I. The used Hamiltonians are taken from the report of Mori and Ando²⁰.

The quantity of $N_{\mathbf{q}(\mathbf{q}_{//})}^{(C,S\pm,HS)}$ is to be determined. When the hot phonon effect is excluded, the phonon population satisfies the Bose-Einstein relation with a lattice temperature T_L . In general, the hot phonon effect plays an important role in hot

TABLE I. The electron-optical-phonon interaction strengths in a quantum well structure

Optical-phonon mode	Interaction strength
Symmetric \pm interface modes ^a	$ M_{q_{//}}^{S\pm} ^2 = \frac{e^2 \hbar \omega_{q_{//}}^{S\pm}}{4Aq\epsilon_0} [h_1^{-1}(\omega_{q_{//}}^{S\pm}) \tanh(\frac{1}{2} q_{//} L_w) + h_2^{-1}(\omega_{q_{//}}^{S\pm})]^{-1} G_{S\pm}^n ^2$ <p style="text-align: center;">where $n = \begin{cases} 1 & : \text{ the well region} \\ 2 & : \text{ barrier regions} \end{cases}$</p>
Confined mode ^{a,b}	$ M_{q_{//}}^C ^2 = \frac{e^2 \hbar \omega_{q_{//}}^C}{V} \left(\frac{1}{\epsilon_{\infty 1}} - \frac{1}{\epsilon_{S1}} \right) \frac{1}{q_{//}^2 + (p\pi/L_w)^2} G_C^p ^2$
Half-space mode ^{a,b,c}	$ M_{q_{//}}^{HS} ^2 = \int_0^\infty \frac{e^2 \hbar \omega_{q_{//}}^{HS}}{2\pi A} \left(\frac{1}{\epsilon_{\infty 2}} - \frac{1}{\epsilon_{S2}} \right) \frac{1}{q_{//}^2 + q_z^2} G_{HS} ^2 dq_z$

^a $G_{S\pm}^n$ is $\langle \varphi_1 | \phi_{S\pm} | \varphi_1 \rangle$, where φ_1 is the electron's ground state and $\phi_{S\pm}$ is potential for interface modes, and the factors G_C^p, G_{HS} are the overlap integral for the p^{th} confined mode and the half-space mode respectively. Their expressions and $h_n(\cdot)$ are shown in the sec. 5.2.

^b $\epsilon_{\infty n}, \epsilon_{Sn}$ are n^{th} layer high frequency and static dielectric constants.

^c q_z is the phonon wave vector paralleled to the crystal's growth direction.

carrier relaxations. The phonon dynamics can be governed by the phonon Boltzmann equation. At the steady state, the phonon's population can be given by the following equation with using eq.(3.1) for bulk (eq.(3.5) for quantum wells)³⁹.

$$\frac{\partial N_{\mathbf{q}(\mathbf{q}_{//})}^{(C,S\pm,HS)}}{\partial t} = \frac{N_{\mathbf{q}(\mathbf{q}_{//})}^{(C,S\pm,HS)} - N_{\mathbf{q}(\mathbf{q}_{//})}^{(C,S\pm,HS)}(T_L)}{\tau_{\text{ph}}} \quad (3.6)$$

where τ_{ph} is the phonon life time.

The dynamical screening on hot carrier relaxations is handled with the electronic dielectric function. Based on the RPA, the dielectric function is given by³⁶

$$\varepsilon_{\text{RPA}}(\mathbf{q}, \omega) = 1 + 2V_{\mathbf{q}} \sum_{\mathbf{k}} \frac{f(E(\mathbf{k} + \mathbf{q})) - f(E(\mathbf{k}))}{\hbar\omega + E(\mathbf{k} + \mathbf{q}) - E(\mathbf{k}) + i\gamma} \quad (3.7)$$

where $V_{\mathbf{q}}$ is $\frac{e^2}{\varepsilon_{\infty} q^2 L^3}$ in 3D and $\frac{e^2}{2\varepsilon_{\infty} q_{//} L^2}$ in 2D. The damping coefficient γ ranges from 0.2 to 0.3 times of the plasma frequency⁴¹.

According to the result from the derivation of Haug and Koch⁴² with the RPA, the effective screened electron-phonon interaction strength $|M_{\mathbf{q}}^{\text{eff}}|^2$ can be expressed as

$$|M_{\mathbf{q}}^{\text{eff}}|^2 = \left| \frac{M_{\mathbf{q}}}{\varepsilon_{\text{RPA}}(\mathbf{q}, \omega)} \right|^2 \quad (3.8)$$

The 3D and 2D zero-temperature dielectric functions are, respectively, given by⁴³

$$\varepsilon_{\text{RPA}}^{3\text{D}}(\mathbf{q}, \omega_{\mathbf{q}}) = 1 + \frac{3n_{3\text{D}}e^2}{4\varepsilon_{\infty}q^2E_{\text{F}}} \left\{ 1 + \frac{k_{\text{F}}}{2q} \left[\left[1 - \left(\frac{\omega_{\mathbf{q}} + i\gamma}{qv_{\text{F}}} + \frac{q}{2k_{\text{F}}} \right)^2 \right] \ln \left| \frac{\frac{\omega_{\mathbf{q}} + i\gamma}{qv_{\text{F}}} + \frac{q}{2k_{\text{F}}} + 1}{\frac{\omega_{\mathbf{q}} + i\gamma}{qv_{\text{F}}} + \frac{q}{2k_{\text{F}}} - 1} \right| \right. \right. \\ \left. \left. - \left[1 - \left(\frac{\omega_{\mathbf{q}} + i\gamma}{qv_{\text{F}}} - \frac{q}{2k_{\text{F}}} \right)^2 \right] \ln \left| \frac{\frac{\omega_{\mathbf{q}} + i\gamma}{qv_{\text{F}}} - \frac{q}{2k_{\text{F}}} + 1}{\frac{\omega_{\mathbf{q}} + i\gamma}{qv_{\text{F}}} - \frac{q}{2k_{\text{F}}} - 1} \right| \right] \right\} \quad (3.9a)$$

$$\varepsilon_{\text{RPA}}^{2\text{D}}(\mathbf{q}_{//}, \omega_{\mathbf{q}_{//}}^{(\text{C,S}\pm,\text{HS})}) = 1 + \frac{n_{2\text{D}} e^2}{2\varepsilon_{\infty n} q_{//} E_{\text{F}}} \left\{ 1 - \frac{k_{\text{F}}}{q_{//}} \left[\left[\left(\frac{\omega_{\mathbf{q}_{//}}^{(\text{C,S}\pm,\text{HS})} + i\gamma}{q_{//} v_{\text{F}}} + \frac{q_{//}}{2k_{\text{F}}} \right)^2 - 1 \right]^{1/2} - \left[\left(\frac{\omega_{\mathbf{q}_{//}}^{(\text{C,S}\pm,\text{HS})} + i\gamma}{q_{//} v_{\text{F}}} - \frac{q_{//}}{2k_{\text{F}}} \right)^2 - 1 \right]^{1/2} \right] \right\} \quad (3.9\text{b})$$

where E_{F} , k_{F} and v_{F} represent Fermi energy, Fermi wave vector and Fermi velocity, respectively.

Finally, the 3D and 2D AELRs can be obtained as the definition shown below

$$(\text{AELR})_{3\text{D}} = \frac{1}{n_{3\text{D}} V} \sum_{\mathbf{q}} \hbar \omega_{\mathbf{q}} \frac{\partial N_{\mathbf{q}}}{\partial t} \quad (3.10\text{a})$$

$$(\text{AELR})_{2\text{D}} = \frac{1}{n_{2\text{D}} A} \sum_{\text{C,S}\pm,\text{HS}} \sum_{\mathbf{q}_{//}, \mathbf{q}_z} \hbar \omega_{\mathbf{q}_{//}}^{(\text{C,S}\pm,\text{HS})} \frac{\partial N_{\mathbf{q}_{//}}^{(\text{C,S}\pm,\text{HS})}}{\partial t} \quad (3.10\text{b})$$

where q_z is defined in the caption of Table I.

3.3 Results and Discussion

The material's parameters and the used assumptions are referred^{40,44-46}. Our calculations of the reduced dimensionality on hot carrier relaxations are performed on a bulk GaAs and a 10nm-width single GaAs/Al_{0.3}Ga_{0.7}As quantum well where the band-offset ratio of $\Delta E_{\text{C}} : \Delta E_{\text{V}} = 65 : 35$ is used⁴⁴. The average phonon energy is approximated in AlGaAs layers to simplify the two-mode behaviors of the GaAs-like and the AlAs-like phonons⁴⁰. The material's parameters are quoted from Adachi's report⁴⁵. The electron's distribution function is assumed to satisfy with Fermi-Dirac relation. We use 300K as the electron's temperature except the section reported the structural dependence in quantum wells, where 600K is taken. An initial lattice temperature is chosen to be 15K. We quote 7ps to be the phonon life times in both bulk GaAs and quantum wells⁴⁶. Only first-order mode²⁰ of confined phonons is considered in our calculation because of the very less contribution to the AELR from

higher-order modes. In general, the AELRs in quantum wells are summed over S_{\pm} interface and the confined modes.

3.3.1 Reduced Dimensionality

In Fig. 3.3 we show the dependence of the AELR on the carrier density in bulk GaAs and a quantum well where the sheet carrier densities are transferred by n_{2D}/L_w . Three sets of curves are shown in the figure representing three different conditions: (1) in the absence of the hot phonon effect and the dynamical screening (denoted by None in the plot), (2) in the presence of the hot phonon effect alone (denoted by HP), and (3) in the presence of both the hot phonon effect and the dynamical screening (denoted by HP+DS). For the first case, the AELRs in the bulk are shown to be higher than that in a quantum well. Above the carrier density of 10^{18} cm^{-3} , the AELR in a quantum well drops much faster than that in a bulk. Because the energy-loss rate in materials is equal to the product of the AELR and the carrier density, this implies that there is a considerable difference in the energy-loss rate between bulk GaAs and a quantum well as the carrier density is increased. In the absence of hot phonon effect and the dynamical screening, the rapid deviation of the AELRs between the 2D and the 3D structures is only attributed to the difference in density of states. Due to the smaller density of state, hot carriers in quantum wells are shown to relax considerably slower than that in the bulk above the critical carrier density. When the hot phonon effect is considered, although the AELRs greatly reduce in both sample's structures, the rapid deviation of the AELR between bulk GaAs and a quantum well still appears while the critical carrier density is shifted to the higher one (toward $2 \times 10^{18} \text{ cm}^{-3}$).

In Fig. 3.4 we show the difference $\left| \text{AELR}_{\text{HP}}^{3D} - \text{AELR}_{\text{HP}}^{2D} \right|$ on the left axis and the ratio $\frac{\left| \text{AELR}_{\text{HP}}^{3D} - \text{AELR}_{\text{HP}}^{2D} \right|}{\text{AELR}_{\text{HP}}^{2D}}$ on the right, where the lower and upper symbols of the

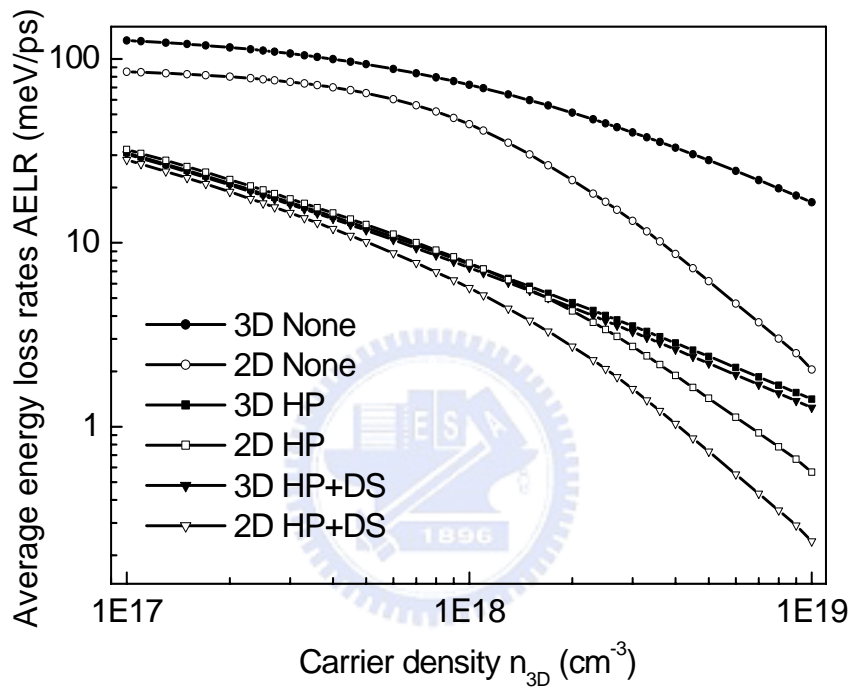


Figure 3.3: Average energy-loss rate with distinct conditions in a bulk GaAs and a 10nm GaAs/Al_{0.24}Ga_{0.76}As quantum well. The symbols “None”, “HP”, and “HP+DS”, respectively, denote the AELRs in the absence of the hot phonon effect and the dynamical screening, in the presence of the hot phonon effect, and in the presence of the hot phonon effect and the dynamical screening. The confined and the S_{\pm} interface modes were considered in the AELR of a quantum well. The carrier temperature of 300K and the initial lattice temperature of 15K were used.

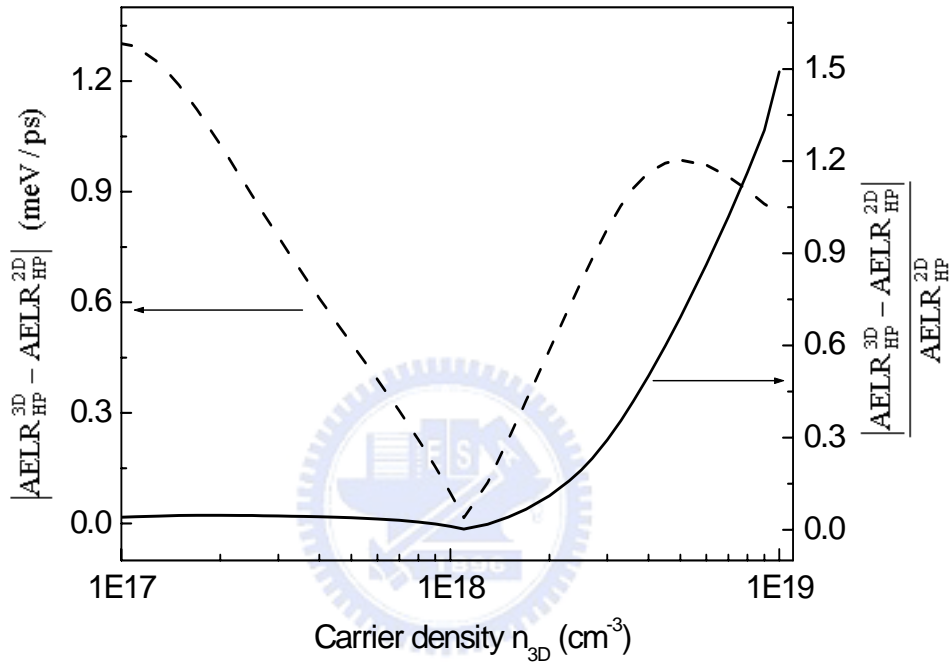


Figure 3.4: Illustration of reduced dimensionality on hot carrier relaxation. The left axis shows the absolute difference of the AELR with the hot phonon effect between a bulk GaAs and a 10nm GaAs/ $\text{Al}_{0.24}\text{Ga}_{0.76}\text{As}$ quantum well while the right axis shows the percentage change of $|\text{AELR}_{\text{HP}}^{3\text{D}} - \text{AELR}_{\text{HP}}^{2\text{D}}|$ per $\text{AELR}_{\text{HP}}^{2\text{D}}$. The AELR of the quantum well was obtained by summing the confined and the S_{\pm} interface modes. The carrier temperature of 300K and the initial lattice temperature of 15K were used.

AELR represent the considered effect and dimensions, respectively. Below the carrier density of 10^{18}cm^{-3} , slightly higher 2D AELRs are demonstrated and this is because the hot phonon effect in quantum wells is weaker than that in the bulk. But, above the carrier density, the effect of the smaller density of state in quantum wells overcomes the hot phonon effect so that 2D AELRs recover to be lower than the 3D case, and the threshold curve clearly shows the significance effect of the distinct density of state on hot carrier relaxations between a bulk GaAs to quantum wells.

3.3.2 Dynamical screening versus Hot Phonon Effect

In our investigation, the 2D dynamical screening is also found to be an important role on hot carrier relaxations at a high carrier density. Due to the great difference of the dynamical screening between the two different dimensions, the calculated results with the HP+DS in Fig. 3.3 shows the more rapid deviation of AELRs between the two sample's structures. In order to compare the screening strength between a bulk GaAs and quantum wells, we plot Fig. 3.5 where the right and left axes, respectively, show reduction factors due to the dynamical screening and the hot phonon effect. The symbols were mentioned earlier. The dynamical screening in quantum wells is shown to be much stronger than that in the bulk and more quickly increased when the carrier density is above 10^{18}cm^{-3} . The quicker increase for the 2D dynamical screening is the consequence of the chemical potential in quantum wells, which is raised faster than that in the bulk as the carrier density is increased. The 2D dynamical screening is also shown to be as important as the hot phonon effect at a high carrier density. To our best knowledge, the earlier investigations^{2,4,5} usually omit the effect of the dynamical screening on hot carrier relaxations. In a short summary, because of the fewer density of state and the strong 2D dynamical screening, hot carriers in quantum wells relax significantly slower than that in the bulk at a carrier density above the critical value of

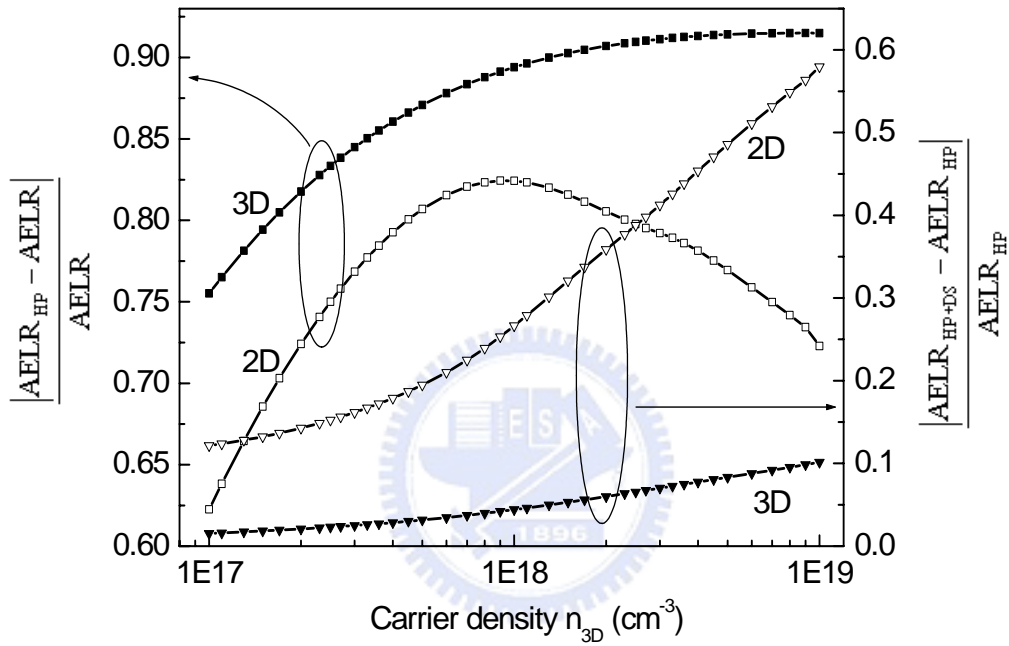


Figure 3.5: Comparison of dynamical screening and hot phonon effect on average energy-loss rate between a bulk GaAs and a 10nm GaAs/Al_{0.24}Ga_{0.76}As quantum well. The left axis shows the hot phonon effect while the right axis shows the dynamical screening. The AELR of a quantum well was obtained by summing the confined and the S_± interface modes. The carrier temperature of 300K and the initial lattice temperature of 15K were used.

$2 \times 10^{18} \text{ cm}^{-3}$. The threshold behavior and the critical carrier density are in very good agreement with the earlier experimental results of Leo⁵, Pelouch⁷, and their co-researchers.

3.3.3 Well-Width Dependence

Next, we interpret the calculated results for the well-width dependence of hot carrier relaxations in quantum wells. The sheet density of $5 \times 10^{11} \text{ cm}^{-2}$ is fixed for all calculated results with different structural parameters. Firstly, we show the dependence of the AELR on the well width for various phonon modes in Fig. 3.6(a), where the S+, the S-, the confined, and the half-space modes are considered. The AELRs for the confined mode always increases until to the well width of 10nm. This is the consequence of the electrons better confined in the wider well and the decreased phonon wave vector parallel to the crystal's growth direction. For the S+ interface modes, because the electron's spatial distribution departs from the double interfaces and the decreased Hamiltonian, the AELRs are shown to quickly decrease with the increased well widths. The S- interface and the half-space modes are less noticeable because of the flatter dependence and much smaller AELR as compared to the other modes. In Fig. 3.6(b), we show the AELRs as functions of the well width and the Al composition by summing over all phonon modes. The opposite dependence on the well width between the confined and the S+ interface modes compensates with each other and brings the protruding well-width dependence for various Al compositions. The protruding behavior was also ever found in the earlier experiment of Ryan and Tatham³⁵. As the Al composition is increased, the well-width dependence of the AELR becomes more appreciable and the maximum AELR moves toward the shorter well width. The reason is the increasingly stronger effect of the S+ interface phonon mode on the hot carrier relaxations with the increased Al composition. The slightly

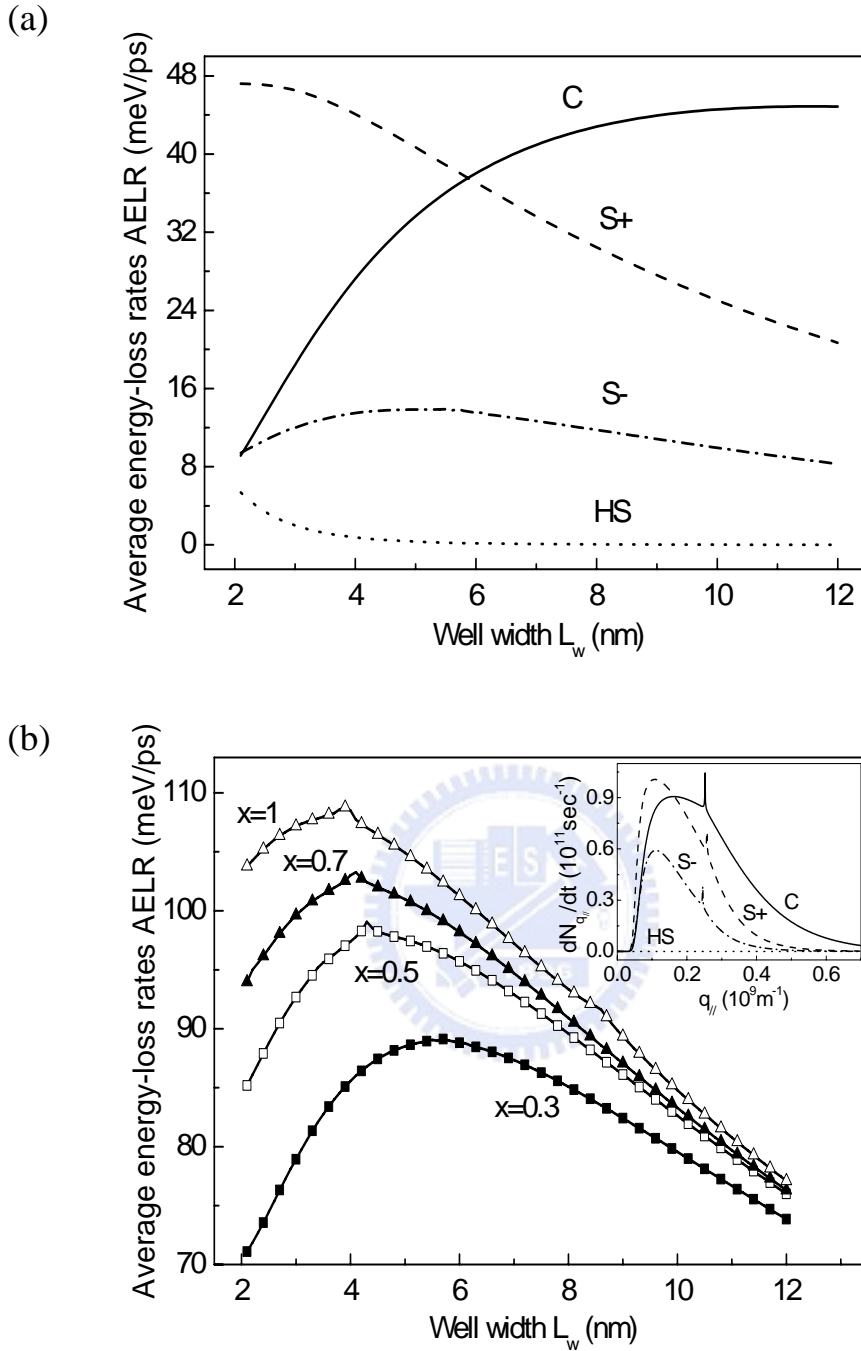


Figure 3.6: Well-width dependence of average energy-loss rate in a GaAs/ $\text{Al}_x\text{Ga}_{1-x}\text{As}$ quantum well. (a) for the confined, S_{\pm} interface, and the half-space modes at $x=0.3$. (b) for the total AELR at $x=0.3, 0.5, 0.7$, and 1 . The inset figure shows the spectrum of the net phonon generation rates in a quantum well with L_w of 10nm and $x=0.3$. The hot phonon effect is included in the AELR. The carrier temperature of 600K , the initial lattice temperature of 15K , and the carrier density of $5 \times 10^{11} \text{ cm}^{-2}$ were used.

roughness in AELR's curves is the consequence of the numerical inaccuracy from the 2D net phonon generation rate where the finite spike at a given in-plane phonon wave vector is shown in the inset of Fig. 3.6(b).

3.4 Summary

We clarify the discrepancies of the earlier experimental results on hot carrier relaxations in bulk GaAs and quantum wells. In contrast to the results in a bulk GaAs, both the dimensionality and the dynamical screening have a significant effect on hot carrier relaxations in quantum wells. The smaller density of state in quantum wells and the strong 2D dynamical screening cause hot carriers in quantum wells to relax significantly slower than that in a bulk GaAs when the carrier density is above $2 \times 10^{18} \text{ cm}^{-3}$. The influence of the 2D dynamical screening on hot carrier relaxations is considerable and is as important as the hot phonon effect when the carrier density is high. As the Al composition is increased, the AELR in quantum wells has a more appreciable dependence on the well width.

References

1. J. F. Ryan, R. A. Taylor, A. J. Turberfield, A. Maciel, J. M. Worlock, A. C. Gossard, and W. Wiegmann, Phys. Rev. Lett. **53**, 1841 (1984).
2. J. Shah, A. Pinczuk, A.C. Gossard, and W. Wiegmann, Phys. Rev. Lett. **54**, 2045 (1985).
3. C. H. Yang, J. M. Carlson-Swindle, S. A. Lyon, and J. M. Worlock, Phys. Rev. Lett. **55**, 2359 (1985).
4. H.-J. Polland, W. W. Rühle, J. Kuhl, K. Ploog, K. Fujiwara, and T. Nakayama, Phys. Rev. B **35**, 8273 (1987).
5. K. Leo, W. W. Rühle, and K. Ploog, Phys. Rev. B **38**, 1947 (1988); K. Leo, W. W. Rühle, H.J. Queisser, and K. Ploog, Phys. Rev. B **37**, 7121 (1987).
6. C. V. Shank, R. L. Fork, R. Yen, J. Shah, B. I. Greene, A. C. Gossard, and C. Weisbuch, Solid State Commun. **47**, 981 (1983).
7. W. S. Pelouch, R. J. Ellingson, P. E. Powers, C. L. Tang, D. M. Szmyd, and A. J. Nozik, Phys. Rev. B **45**, 1450 (1992).
8. Y. Rosenwaks, M. C. Hanna, D. H. Levi, D. M. Szmyd, R. K. Ahrenkiel, and A. J. Nozik, Phys. Rev. B **48**, 14675 (1993).
9. Z. Y. Xu and C. L. Tang, Appl. Phys. Lett. **44**, 692 (1984).
10. K. Kash, D. Block, and J. Shah, Phys. Rev. B **33**, 8762 (1986).
11. H. Lobentanzer, W. Stolz, J. Nagle, and K. Ploog, Phys. Rev. B **39**, 5234 (1989).
12. J. F. Young and P. J. Kelly, Phys. Rev. B **47**, 6316 (1993).
13. J. H. Collet, Phys. Rev. B **39**, 7659 (1989).
14. E. J. Yoffa, Phys. Rev. B **23**, 1909 (1981).
15. R. G. Ulbrich, Phys. Rev. B **8**, 5719 (1973).
16. R. Fuchs and K. L. Kliewer, Phys. Rev **140**, A2076 (1965).

17. J. J. Licari and R. Evrard, Phys. Rev. B **15**, 2254 (1977).
18. R. Lassnig, Phys. Rev. B **30**, 7132 (1984).
19. K. Huang and B. Zhu, Phys. Rev. **38**, 13377 (1988).
20. N. Mori and T. Ando, Phys. Rev. B **40**, 6175 (1989).
21. R. Chen, D. L. Lin, and T. F. George, Phys. Rev. B **41**, 1435 (1990).
22. G. Q. Hai, F. M. Peeters, and J. T. Devreese, Phys. Rev. B **48**, 4666 (1993).
23. M. P. Chamberlain, M. Cardona, Phys. Rev. B **48**, 14356 (1993).
24. H. Rucker, E. Molinari, and P. Lugli, Phys. Rev. B **45**, 6747 (1992); H. Rucker, E. Molinari, and P. Lugli, Phys. Rev. B **44**, 3463 (1991).
25. B. K. Ridley, Phys. Rev. B **47**, 4592 (1993); B. K. Ridley, Phys. Rev. B **39**, 5282 (1989).
26. V. N. Stavrou, C. R. Bennett, O. M. M. Al-Dossary, M. Babiker, Phys. Rev. B **63**, 205304-1 (2001);
27. A. K. Sood, J. Menendez, M. Cardona, and K. Ploog, Phys. Rev. Lett. **54**, 2111 (1985).
28. A. K. Sood, J. Menendez, M. Cardona, and K. Ploog, Phys. Rev. Lett. **54**, 2115 (1985).
29. J. K. Jain and S. D. Sarma, Phys. Rev. Lett. **62**, 2305 (1989).
30. K. T. Tseng, K. R. Wald, T. Ruf, P. Y. Yu, H. Morkoc, Phys. Rev. Lett. **67**, 2557 (1991).
31. A. J. Shields, M. Cardona, and K. Eberl, Phys. Rev. Lett. **72**, 412 (1994); A. J. Shields, M. P. Chamberlain, M. Cardona, and K. Eberl, Phys. Rev. B **51**, 17728 (1994).
32. A. K. Arora, E. -K. Suh, A. K. Ramdas, F. A. Chambers, and A. L. Moretti, Phys. Rev. B **36**, 6142 (1987).
33. V. F. Sapega, M. P. Chamberlain, T. Ruf, M. Cardona, D. N. Mirlin, K. Totemeyer,

- A. Fischer, and K. Eberl, Phys. Rev. B **52**, 14144 (1995).
34. M. Tatham, R. A. Taylor, J. F. Ryan, W. I. Wang, and C. T. Foxon, Solid State Electron. **31**, 459 (1988).
35. J. F. Ryan and M. Tatham, Solid State Electron. **32**, 1429 (1989).
36. G. Mahan, Many Particle Physics (New York, Plenum, 2000).
37. S. D. Sarma, J. K. Jain, and R. Jalabert, Phys. Rev. B **37**, 6290 (1988).
38. J. Shah, Solid State Electron. **21**, 43 (1978).
39. J. T. Devreese and F. M. Peeters, "The Physics of the Two-Dimensional Electron Gas" (New York, Plenum, 1987), p.183-p.225.
40. H. C. Lee, K. W. Sun, and C. P. Lee, J. of Appl. Phys. **92**, 268 (2002).
41. T. Thoai and H. Haug, Phys. Status Solidi B **98**, 581 (1980).
42. H. Haug and S. W. Koch, "Quantum Theory of Optical and Electronic Properties of Semiconductors" (Singapore, World Scientific, 1994), p.142-p.144.
43. J. Shah, "Hot Carriers in Semiconductor Nanostructures: Physics and Applications" (Boston, Academic, 1992), p.61.
44. C. G. V. de Walle, Phys. Rev. B **39**, 1871 (1989).
45. S. Adachi, J. Appl. Phys. **58**, R1 (1985).
46. J. F. Ryan, M. Tatham, D. J. Westland, C. T. Foxon, and W. I. Wang, Proc. SPIE **942**, 256 (1988).

Chapter 4

Plasmon-Phonon Coupling

4.1 Introduction

Electronic collective oscillations in multiple quantum wells have been shown to be naturally different from that in the absence of heterointerfaces both theoretically¹⁻¹³ and experimentally¹⁴⁻²¹. The broken spatial symmetry has caused several fundamental kinds of plasmons in multiple quantum wells. They can be categorized into intrasubband, intersubband, intrawell and interwell types when the quantum confinement and the Coulomb coupling between different layers are considered, respectively. Theoretically, the electronic collective oscillations were solved which is modeled by a large number of electrons in multiple quantum wells and based on the density matrix method with the self-consistent field approximation (SCF)^{2,3}. The dispersion relations indicate that in the case of weak Coulomb coupling between adjacent quantum wells, the collective oscillation behaves like that of an ideal two-dimensional gas. At the long wavelength limit, the plasmon energy is proportional to the root of the in-plane wave vector, which was firstly proposed by F. Stern¹. On the contrary, when the Coulomb coupling is strong, this would result in the optical and acoustic plasmon modes at the long wavelength limit, which are very similar to the lattice vibration in polar semiconductors. Intersubband plasmon's types are the interesting case caused by the quantum effect on the collective electronic oscillation. Many improved theories are developed^{8-10,12,13}. The resonant screening¹⁰ (depolarization shift), excitonic shifts³ (final-state correction), and vertex correction

due to many-body effects⁹ are taken into the consideration to obtain more accurate dispersions of intersubband plasmons. While numerous electronic collective oscillations in quantum wells are theoretically studied, there also have very good agreement with experimental results¹⁴⁻²¹. Because of high-quality samples grown by using molecular beam epitaxy, various types of plasmons in modulation-doped GaAs/AlGaAs quantum wells are experimentally observed. The earlier reports of intrasubband and intersubband plasmons consisted of a layered electron gas can be found in Ref. [14-16]. By using the electronic Raman scattering, intrawell and interwell plasmons in multiple quantum wells are also systematically studied. Their dispersions are determined clearly and the experimental results are reported in Ref. [17,18].

Because the electron gas is immersed in a crystal structure, the interaction between plasmons and phonons via the macroscopic electric field could arise, which is so-called the plasmon-phonon coupling (PPC). When double heterojunctions are further considered, the PPC behavior is more complex and the mathematical treatment becomes more difficult than the bulk case either from electrodynamics or many-body technique. However, if one uses the given phonon and plasmon modes in the presence of double heterojunctions²²⁻³⁰ to probe the problem, the mathematical treatment could be greatly simplified and the physical meaning is also clearer. For instance, the intersubband plasmon between adjacent energy levels would not couple to interface phonon modes because of their perpendicular polarization. The previous one polarizes parallel to the crystal growth direction while another parallel to its propagation direction along heterointerfaces. In addition, the relevant derivations for the PPC can also follow the developed method in the bulk case as long as replacing objects by that in quantum wells. Wendler and Pechstedt²⁶ attempted to obtain the PPC dispersions from the total dielectric function that is accounted by the electron-electron,

electron-interface phonon, and electron-confined phonon interaction terms with using Dyson equation and the RPA. The results are dramatic different from the those in bulk. Coupling between plasmon, confined, and interface phonons causes their dispersions deviate from that the uncoupled ones. Setting the real part of the total dielectric function to be zero, coupled dispersion branches are obtained and shown to deviate from the uncoupled modes.

In our investigation, another possible coupling of plasmons and phonons in the presence of double interfaces is proposed. Differing from the mechanism of Wendler and Pechstedt²⁶, we assume that intrasubband plasmons individually interact with interface and confined modes; that is, the quasi-2D PPC results in the plasmon-interface phonon and the plasmon-confined phonon coupled modes. Each coupled mode splits into the plasmon-like and the phonon-like modes. The dispersions are obtained by using the renormalized phonon propagators, corrected by taking the effect of free electron gas. Following the PPC treatment proposed by Sarma and co-researchers²²⁻²⁴, the net plasmon-phonon generation rates are calculated and used to obtain AELR by summing over all coupled modes. Plasmon-like modes are found to be considerable for hot carrier relaxations around the sheet carrier density of 10^{11} cm^{-2} , where the enhanced AELR are shown as compared to the uncoupled case. We also found that an increase in carrier temperature reduces the AELR enhancement but does not influence the considerable sheet carrier density.

4.2 Re-normalized Phonon Propagator

In this section, the coupled dispersion relations and the net plasmon-phonon generation rates are shown. Our calculation is performed on a 10nm single GaAs/Al_{0.24}Ga_{0.76}As quantum well. Based on the DCM³¹⁻³³, the S+, the S-, and the C

phonon types are considered in a quantum well. The electrons in the quantum well are simplified by ideal 2D electron gas and the plasma dispersion is given by¹⁰

$$\omega_p = \left(\frac{n_{2D} e^2}{2m_e \epsilon_\infty} q_{//} \right)^{1/2} \quad (4.1)$$

With the PPC effect, six coupling branches are considered. They are two of the plasmon- S+ (PS+), two of the plasmon- S- (PS-), and two of the plasmon-confined (PC) coupled modes. The renormalized phonon propagator due to the correction of free electron gas is given by³⁴

$$D(\mathbf{q}_{//}, \omega) = \frac{2\omega_i}{\omega^2 - \omega_i^2 - 2\omega_i |M_i|^2 \Pi_0(\mathbf{q}_{//}, \omega) / \epsilon(\mathbf{q}_{//}, \omega)} \quad (4.2)$$

where ω denotes the modified energy while ω_i represents uncoupled phonon energies where the index i denotes the S+, the S-, and the C phonon modes. M_i^2 denote the electron-phonon interaction strengths and the expressions are reported in the Ref.[22]. The polarizability function $\Pi_0(\mathbf{q}_{//}, \omega)$ and the dielectric function $\epsilon(\mathbf{q}_{//}, \omega)$ in the renormalized phonon propagator were adapted from the work of Sarma^{23,24}, who assume the plasmon-pole approximation for the dielectric function and the unknown coefficient was determined by using the Kramers-Kronig relation. The expression can be found in the report^{23,24} and not shown here. As a result, the coupled dispersion relations and the interaction strengths for the coupled modes are given by^{23,24}

$$\omega_{i(\pm)} = \sqrt{\frac{1}{2} \left\{ \omega_i^2 + \tilde{\omega}_p^2 \pm \left[(\omega_i^2 - \tilde{\omega}_p^2)^2 + 8\omega_i \omega_p^2 \frac{M_i^2}{\hbar V_{q_{//}}} \right]^{1/2} \right\}} \quad (4.3)$$

$$M_{i(\pm)}^2 = \frac{\omega_i}{\omega_{i(\pm)}} \frac{|\omega_{i(\pm)}^2 - \tilde{\omega}_p^2|}{\omega_{i(+)}^2 - \omega_{i(-)}^2} M_i^2 \quad (4.4)$$

where $\omega_{i(\pm)}$ represents the upper (+) and the lower (-) energies with the PPC effect.

So does the coupled interaction strength $M_{i(\pm)}^2$.

$$\tilde{\omega}_p^2 = \omega_p^2 + \frac{n_{2D} q_{//}^2}{m_{e1} |\Pi_0(\mathbf{q}_{//}, \omega = 0)|} \quad (4.5)$$

Then, the 2D net plasmon-phonon generation rate in GaAs region is given by

$$\frac{\partial N_{i(\pm)}}{\partial t} = \frac{\sqrt{2m_{e1}^3 k_B T_C} A}{\pi \hbar^4 q_{//}} M_{i(\pm)}^2 [N_{i(\pm)}(T_C) - N_{i(\pm)}] \int_{\zeta_{\min}}^{\infty} \frac{1}{\sqrt{\zeta}} [f(\zeta + \zeta_1) - f(\zeta + \zeta_1 + \frac{\hbar\omega_{i(\pm)}}{k_B T_C})] d\zeta \quad (4.6)$$

where $N_{i(\pm)}(T_C)$ and $N_{i(\pm)}$ are, respectively, Bose-Einstein number³⁵ at T_C and nonequilibrium phonon number. ζ_{\min} is the minimum normalized energy required for an electron to kick out a plasmon-phonon modes of wave vector $\mathbf{q}_{//}$. It is given by

$$\zeta_{\min} = \frac{m_{e1}}{2\hbar^2 q_{//}^2 k_B T_C} \left| \frac{\hbar^2 q_{//}^2}{2m_{e1}} - \hbar\omega_{i(\pm)} \right|^2 \quad (4.7)$$

The net generation rate in AlGaAs region is treated as the uncoupled case because the electrons are generated in the well region. Hot phonon effect and the dynamical screening are also taken into the consideration. The determination of nonequilibrium occupation can be obtained by solving the steady-state phonon Boltzmann equation. The dynamical screening with the RPA is considered. Finally, the AELR can be obtained by the definition shown below.

$$\text{AELR} = \frac{1}{n_{2D} A} \sum_{\mathbf{q}_{//, q_z, (\pm)}} \hbar\omega_{i(\pm)} \frac{\partial N_{i(\pm)}}{\partial t} \quad (4.8)$$

4.3 Results and Discussion

4.3.1 Dispersion Relation

In Fig. 4.1(a) and 4.1(b) we show the coupled plasmon-phonon energies as a function of the in-plane wave vector on the two sheet carrier densities of 10^{11} and 10^{12} cm^{-2} with a carrier temperature of 300K and an initial lattice temperature of 15K. The PS+, the PS-, and the PC coupled modes are shown in the plots, where L+ and L- represent the upper and lower branches for each couple mode, respectively. As energies of L+ branches approach to that of L- branches, the two vibration modes are perturbed with each other so that the energies of the two branches are shown to deviate, which splitting arises. When the in-plane wave vectors are smaller than the coupled places, L+ and L- branches behave as the phonon-like and the plasmon-like modes, respectively. On the opposite case, the behaviors of the two branches exchange with each other. As the sheet carrier densities increase, the crossing in-plane wave vectors are shown to move toward lower. When the crossing wave vector leaves the range of the plasmon-phonon coupled modes generated by hot carriers, PPC is expected not to influence significantly hot carrier relaxations as compared to the uncoupled case. In the sheet density of 10^{11} cm^{-2} , we show the enlarged plot of lower branches in the inset. The figure indicates that the PS+ mode becomes to the lowest one among three coupled modes. The little amount of the energy difference will be shown to have a significant effect on the net plasmon-like generation rates.

4.3.2 Average Energy-Loss Rate

In Fig. 4.2(a) and 4.2(b) we show the net plasmon-phonon generation rates as a function of the in-plane wave vector on the two sheet carrier densities same as mentioned above. The quantity of the L+ branch of PS+ mode is plotted on the right axis while others are plotted on the left. The generation rates are shown to have different behavior between the two sheet densities. In the sheet density of 10^{11} cm^{-2} , because the crossing in-plane wave vector is larger than the range of the

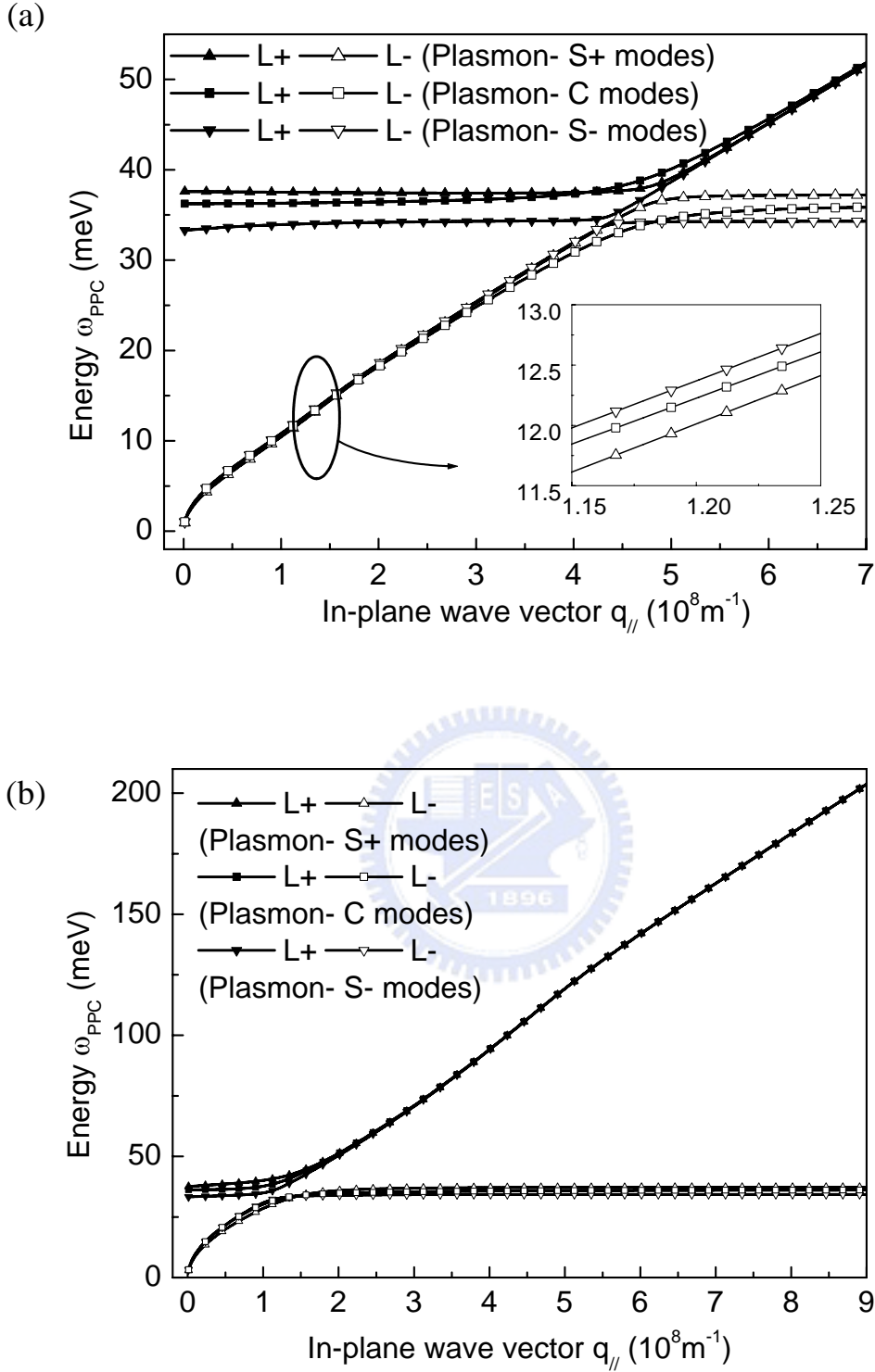


Figure 4.1: Dispersion curves of plasmon-phonon coupled mode in a 10nm GaAs/Al_{0.24}Ga_{0.76}As quantum well. (a) the carrier density of 10^{11}cm^{-2} . The inset shows the enlarged plot. (b) the carrier density of 10^{12}cm^{-2} . L+ and L- denote the upper and lower modes, respectively. A carrier temperature of 300K and an initial lattice temperature of 15K are used.

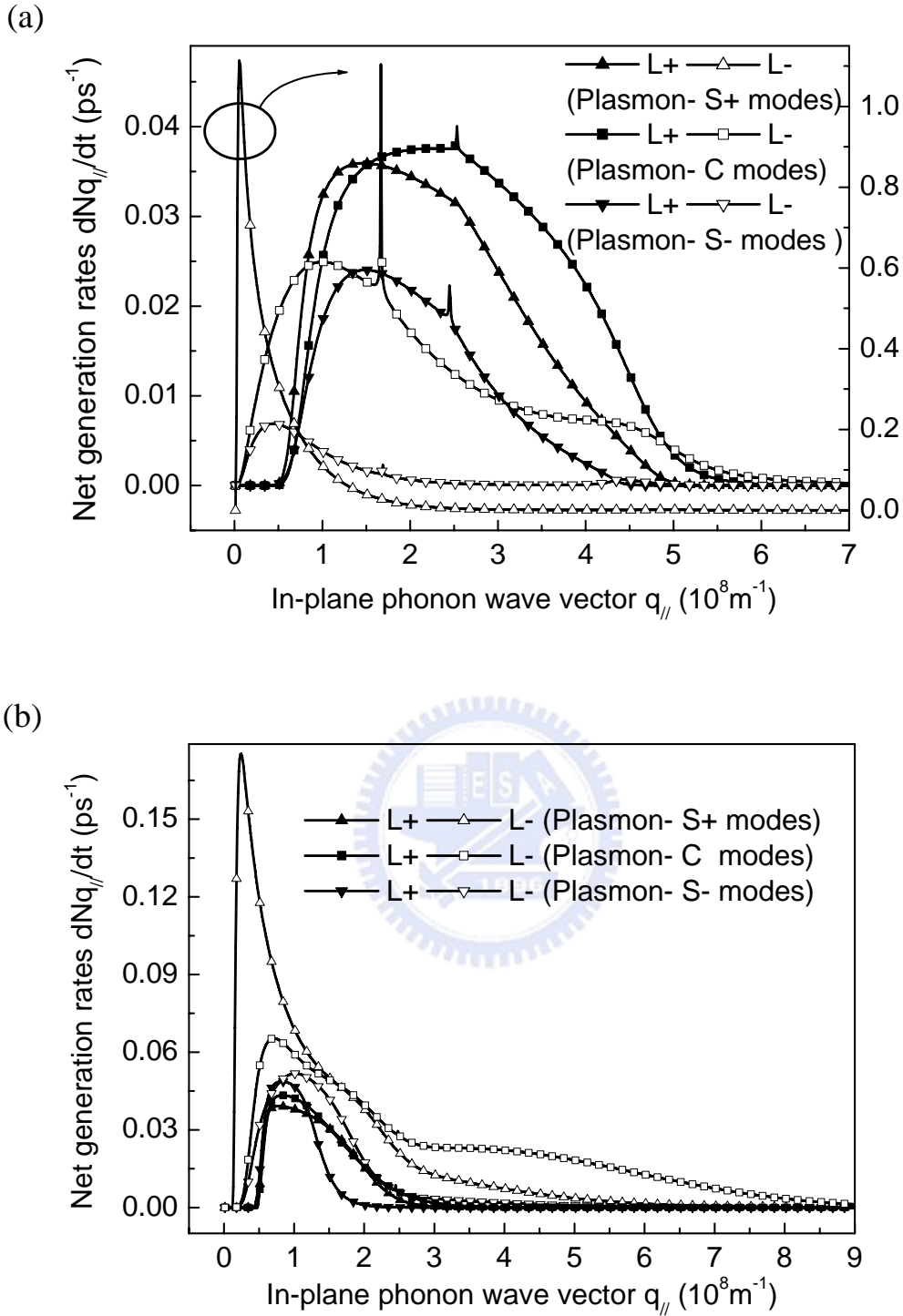


Figure 4.2: Net plasmon-phonon generation rate in a 10nm GaAs/Al_{0.24}Ga_{0.76}As quantum well. (a) the carrier density of 10^{11}cm^{-2} . (b) the carrier density of 10^{12}cm^{-2} . L+ and L- denote the upper and lower modes, respectively. A carrier temperature of 300K and an initial lattice temperature of 15K are used.

plasmon-phonon coupled modes that could be generated by hot carriers, the L+ and L- branches correspond to the phonon-like and the plasmon-like modes, respectively. A very larger generation rate of the PS+ plasmon-like mode than others is found and this can be categorized into two reasons. The first one is that L- branches become important relaxation channels for hot carriers at the sheet density shown in the eq. (4.4). Another is that more PS+ plasmon-like mode than others can be excited due to the lowest energy among the two other plasmon-like branches shown in the inset of Fig. 4.1(a). Because of Bose-Einstein relation $N_{i(\pm)}(T_C)$, the little energy difference between them causes the significant effect. The considerable net generation rate also leads enhanced AELR as compared to the case without the PPC effect. The spike in the curves is the consequence of the net plasmon-phonon generation rate with an ideal 2D treatment, where the inside function is proportional to $1/\sqrt{\zeta}$ shown in eq.(4.6). It is finite and does not give much AELR due to the very narrow width.

In the sheet density of 10^{12} cm^{-2} , the crossing in-plane wave vector is around $1.2 \times 10^8 \text{ m}^{-1}$, which is on the intermediate range of the in-plane wave vector of plasmon-phonon coupled modes that can be generated by hot carriers. So, the plasmon-like and the phonon-like modes do not entirely correspond to L- and L+ branches. Plasmon-like (phonon-like) modes distribute on the L- (L+) branches below the crossing in-plane wave vector and the L+ (L-) branches above the crossing wave vector. A rapid drop in the net plasmon-like generation rate as compared to the sheet density of 10^{11} cm^{-2} is found. This is the consequence of the crossing in-plane wave vector moving toward smaller than the case of sheet density of 10^{11} cm^{-2} . Because of a quick rise of L- branches, based on Bose-Einstein relation, excitations of plasmon-like modes are shown to decrease rapidly. Another plasmon-like modes on the L+ branches above the crossing in-plane wave vector are also shown to have small the net

plasmon-like generation rates. Thus, it is expected that, as the sheet densities increase above 10^{12} cm^{-2} , plasmon-like modes gradually become a minor relaxation channel for hot carriers. Around the in-plane wave vector of 10^8 m^{-1} , the L+ branch of the PS-mode is shown to have a slightly larger net plasmon-phonon generation rate than L+ branches of PS+ and PC modes. This is different from the case of the sheet density of 10^{11} cm^{-2} .

In Fig. 4.3 we show the dependence of the AELR summed over all plasmon-phonon modes and the AELR with different conditions on the sheet carrier density. The different conditions include the bare electron-phonon interaction, HP, DS, HD and static screening (SS), where the notations are same as the chap. 3. The PPC is shown to enhance the AELR and this is the consequence of the contribution of plasmon-like modes to the AELR. Around the sheet density of 10^{11} cm^{-2} , plasmon-like modes are found to be massively generated by hot carriers and significantly influence the AELR. Below the sheet density of 10^{11} cm^{-2} , the crossing in-plane wave vector is gradually larger and departs from the range of wave vector that hot carriers can generate so the contribution to the AELR from the plasmon-like modes becomes smaller. When the sheet density increases above of 10^{11} cm^{-2} , as mentioned earlier, the rapid increase in the plasmon-like energy causes the mode to be more difficultly excited by hot carriers so the contribution also becomes smaller. In these sheet densities, hot phonon effect is shown to decrease the AELR more strongly than dynamical screening, for which there found increasingly shielding strength at high sheet densities. Static screening is shown to overestimate the shielding strength.

4.3.3 Carrier Temperature Effect

The effect of the carrier temperature on the PPC is studied. We show the AELR as a function of sheet densities on the two temperatures of 100K and 500K in Fig. 4.4.

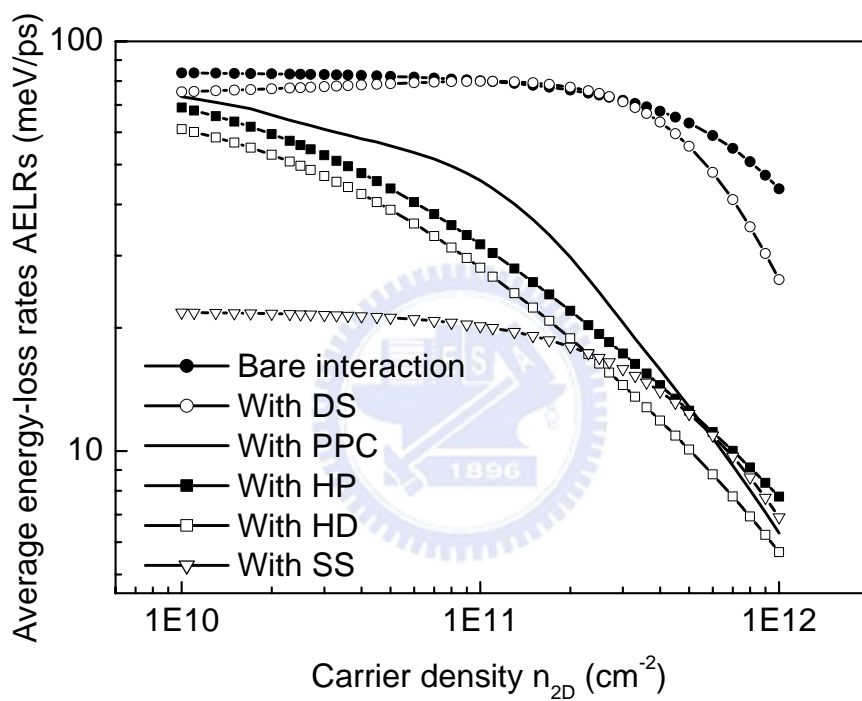


Figure 4.3: Illustration of plasmon-phonon coupling on average energy-loss rate in a 10nm GaAs/ $\text{Al}_{0.24}\text{Ga}_{0.76}\text{As}$ quantum well. Bare: the AELR without any effects, DS: with the dynamical screening, HP: with the hot phonon effect, PPC: with the plasmon-phonon coupling (including HP and DS), HD: with HP and DS, SS: with the static screening.

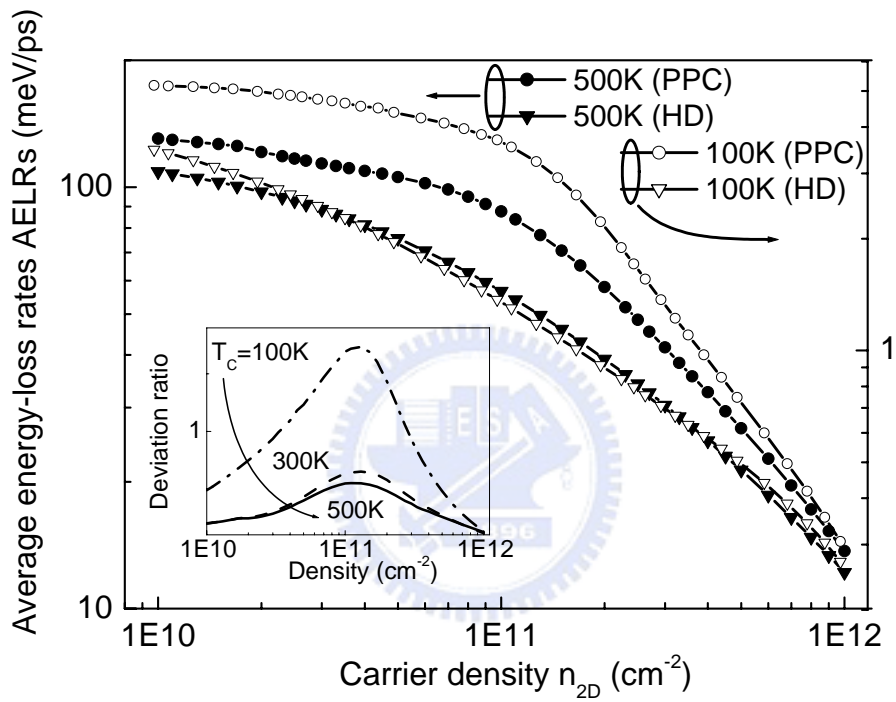


Figure 4.4: Illustration of carrier temperature effect on plasmon-phonon coupling in a 10nm GaAs/Al_{0.24}Ga_{0.76}As quantum well. HD: with the hot phonon effect and the dynamical screening. PPC: with the plasmon-phonon coupling (including HD). Inset figure shows the deviation ratio caused by the PPC.

The PPC effect on hot carrier relaxations at the carrier temperature of 100K is found to enhance the AELR more strongly than that at 500K. In the inset of Fig. 4.4 we show the deviation ratio $((AELR_{PPC}-AELR_{HD})/AELR_{HD})$ as a function of sheet densities on the different carrier temperatures. It is found that the carrier temperature does not significantly influence the sheet densities where the maximum deviation ratio is shown. As the carrier temperature increases, the enhancement on the AELR by the PPC effect becomes smaller. This is the consequence of hot phonon effect. It more greatly drops the net plasmon-phonon generation rate at higher carrier temperature so that the enhancement of ALER by the PPC effect is shown to gradually disappear.

4.4 Summary

Using renormalized phonon propagators, six plasmon-phonon coupled branches in a quantum well are obtained and used to study the influence of the PPC on hot carrier relaxations. When hot carriers can relax their excess energies via the plasmon-like modes, the considerable enhancement of the AELR by the PPC is found. The effect is significant when the sheet carrier densities are around 10^{11} cm^{-2} and the carrier temperatures are low. At higher sheet densities, the effect gradually evanesces because hot carriers are more difficult to excite the plasmon-like modes due to the increased energies. The enhancement of the AELR also strongly depends on hot phonon effect. Thus, at the carrier temperature as low as possible but higher than³⁶ 40K, decreasing nonequilibrium phonons would lead more noticeable effect of the PPC on hot carrier relaxations around the sheet carrier densities of 10^{11} cm^{-2} .

References

1. F. Stern, Phys. Rev. Lett. **18**, 546 (1967).
2. S. D. Sarma and J. J. Quinn, Phys. Rev. B **25**, 7603 (1982).
3. A. C. Tselis and J. J. Quinn, Phys. Rev. B **29**, 3318 (1984).
4. S. D. Sarma and E. H. Hwang, Phys. Rev. Lett. **81**, 4216 (1998).
5. E. H. Hwang and S. D. Sarma, Phys. Rev. B **64**, 165409-1 (2001).
6. J. K. Jain and P. B. Allen, Phys. Rev. Lett. **54**, 2437 (1985).
7. S. J. Cheng and R. R. Gerhardts, Phys. Rev. B **63**, 035314-1 (2001).
8. W. H. Backes, F. M. Peeters, F. Brosens, and J. T. Devreese, Phys. Rev. B. **45**, 8437 (1992).
9. B. Vinter. Phys. Rev. B **13**, 4447 (1976); **15**, 3947 (1977).
10. D. Dahl and L. J. Sham, Phys. Rev. B **16**, 651 (1977).
11. W. L. Bloss, Solid. State Commun. **46**, 779 (1983).
12. W. P. Chen, Y. J. Chen, and E. Burstein, Surf. Sci. **58**, 263 (1976).
13. A. Tselis, G. Gonzales de la Cruz, and J. J. Quinn, Solid. State Commun. **46**, 779 (1983).
14. D. Olego, A. Pinczuk, A. C. Gossard, and W. Wiegmann, Phys. Rev. B **26**, 7867 (1982).
15. G. Abstreiter and K. Ploog, Phys. Rev. Lett. **42**, 1308 (1979).
16. R. Sooryakumar, A. Pinczuk, A. Gossard, and W. Wiegmann, Phys. Rev. B **31**, 2578 (1985).
17. G. Fasol, N. Mestres, H. P. Hughes, A. Fischer, and K. Ploog, Phys. Rev. Lett. **56**, 2517 (1986).
18. G. Fasol, R. D. King-Smith, D. Richards, U. Ekenberg, N. Mestres, and K. Ploog, Phys. Rev. B **39**, 12695 (1989).

19. A. Pinczuk, M. G. Lamont, and A. C. Gossard, Phys. Rev. Lett. **56**, 2092 (1986).
20. R. Merlin, K. Bajema, R. Clarke, F.-Y Juang, and P. K. Bhattacharya, Phys. Rev. Lett. **55**, 1768 (1985).
21. S. Oelting, D. Heitmann, and J. P. Kotthaus, Phys. Rev. Lett. **56**, 1846 (1986).
22. J. K. Jain, R. Jalabert, and S. D. Sarma, Phys. Rev. Lett. **60**, 353 (1988).
23. S. D. Sarma, J. K. Jain, and R. Jalabert, Phys. Rev. B **37**, 6290 (1988).
24. S. D. Sarma, J. K. Jain, and R. Jalabert, Phys. Rev. B **37**, 1228 (1988), S. D. Sarma, J. K. Jain, and R. Jalabert, Phys. Rev. B **37**, 4560 (1988).
25. J. F. Young and P. J. Kelly, Phys. Rev. B **47**, 6316 (1993).
26. L. Wendler and R. Pechstedt, Phys. Rev. B **35**, 5887 (1987).
27. W. Xiaoguang, F. M. Peeters, and J. T. Devreese, Phys. Rev. B **32**, 6982 (1985).
28. K. J. Yee, D. S. Yee, D. S. Kim, T. Dekorsy, G. C. Cho, and Y. S. Lim, Phys. Rev. B **60**, R8513 (1999).
29. J. J. Baumberg and D. A. Williams, Phys. Rev. B **53**, R16140 (1996).
30. T. Dekorsy, A. M. T. Kim, G. C. Cho, H. Kurz, A. V. Kuznetsov, and A. Forster, Phys. Rev. B **53**, 1531 (1996).
31. J. J. Licari and R. Evrard, Phys. Rev. B **15**, 2254 (1977).
32. N. Mori and T. Ando, Phys. Rev. B **40**, 6175 (1989).
33. A. K. Sood, J. Menendez, M. Cardona, and K. Ploog, Phys. Rev. Lett. **54**, 2111 (1985); A. K. Sood, J. Menendez, M. Cardona, and K. Ploog, Phys. Rev. Lett. **54**, 2115 (1985).
34. G. D. Mahan, "Many-particle physics" (Kluwer Academic, Plenum Publishers, New York, 2000), p.468-474.
35. J. T. Devreese and F. M. Peeters, "The Physics of the Two-Dimensional Electron Gas" (Plenum, New York, 1987), p.183-225.

36. J. Shah, “Ultrafast Spectroscopy of Semiconductors and Semiconductor Nanostructures” (Springer, Berlin, 1996), p.163.



Chapter 5

Structure Effect on Fröhlich Interaction

5.1 Introduction

Electron polar-optical-phonon interaction in III-V semiconductor quantum wells plays an important role for hot carrier relaxations, which influence the high-speed responses of many quantum devices. In the past, electron-phonon scattering rates in a quantum well were typically calculated using the bulk phonon model or the bulk-like phonon model¹⁻³. In the bulk-like phonon model, the optical phonon modes are assumed to be the same as those in the bulk material while the electron wave functions incorporate quantum confinement. More recently, the DCM⁴⁻⁷ and Huang-Zhu model⁸ (HZM) were developed for dielectric slab problems and were more accurate than the bulk and the bulk-like phonon models. The fundamental types of phonon modes^{4,7,8} and the electron-phonon Hamiltonian^{5,6,8} in heterostructures have become an interesting subject. Experimentally, Ploog et al.^{9,10} discovered the evidence of the confined LO, TO phonons and interface phonons in GaAs/AlAs superlattices using Raman scattering. An order of magnitude reduction in the intersubband scattering rates in GaAs/Al_xGa_{1-x}As quantum wells was reported by Schlapp et al. using an infrared bleaching technique¹¹. The reduced scattering rates were explained successfully by Sarma et al. using the DCM¹².

In the last decade, techniques involving ultrafast spectroscopy became very

powerful tools in studying carrier dynamics in semiconductors. Ploog et al.¹³⁻¹⁵ used time-resolved photoluminescence to study the hot carrier relaxation in a quasi-two dimensional system. Their experimental results were analyzed with the AELR¹⁶ and indicated that the width of a quantum well had little effect on the hot carrier relaxation. However, the AELR in their analysis was calculated using the bulk phonon model.

More recently, a better method using the hot-electron neutral-acceptor luminescence¹⁷, shown in Fig. 5.1, was developed to study the carrier relaxation mechanisms. It gives a better spectral resolution at lower carrier excitation densities than those of the ultrafast spectroscopy technique. This method has been used¹⁸⁻²⁰ to determine the effective phonon energy in GaAs/Al_xGa_{1-x}As quantum wells with various structure parameters. The effective phonon energy can be estimated in our calculations and be compared with experimental measurements.

The purpose of the report is to calculate the electron-phonon scattering rates in GaAs/Al_xGa_{1-x}As quantum wells with various structure parameters based on the DCM model. Especially, we focus on the dependence of the electron-optical phonon interaction on the Al composition in the barrier, which is the subject that is still lacking in earlier reports. The calculated results are compared with earlier experimental results²⁰.

5.2 Dielectric Continuum Model

5.2.1 Phonon energy in GaAs/Al_xGa_{1-x}As quantum wells

Based on DCM, there are six types of optical-phonon modes⁶ in a dielectric slab. However, due to selection rules for the intra-subband scattering, only the confined LO mode, the half-space LO mode, and the symmetric interface modes were taken into consideration in our calculations. The confined phonons propagate in the well, and the component of the phonon wave vector along the layer growth direction (z direction)

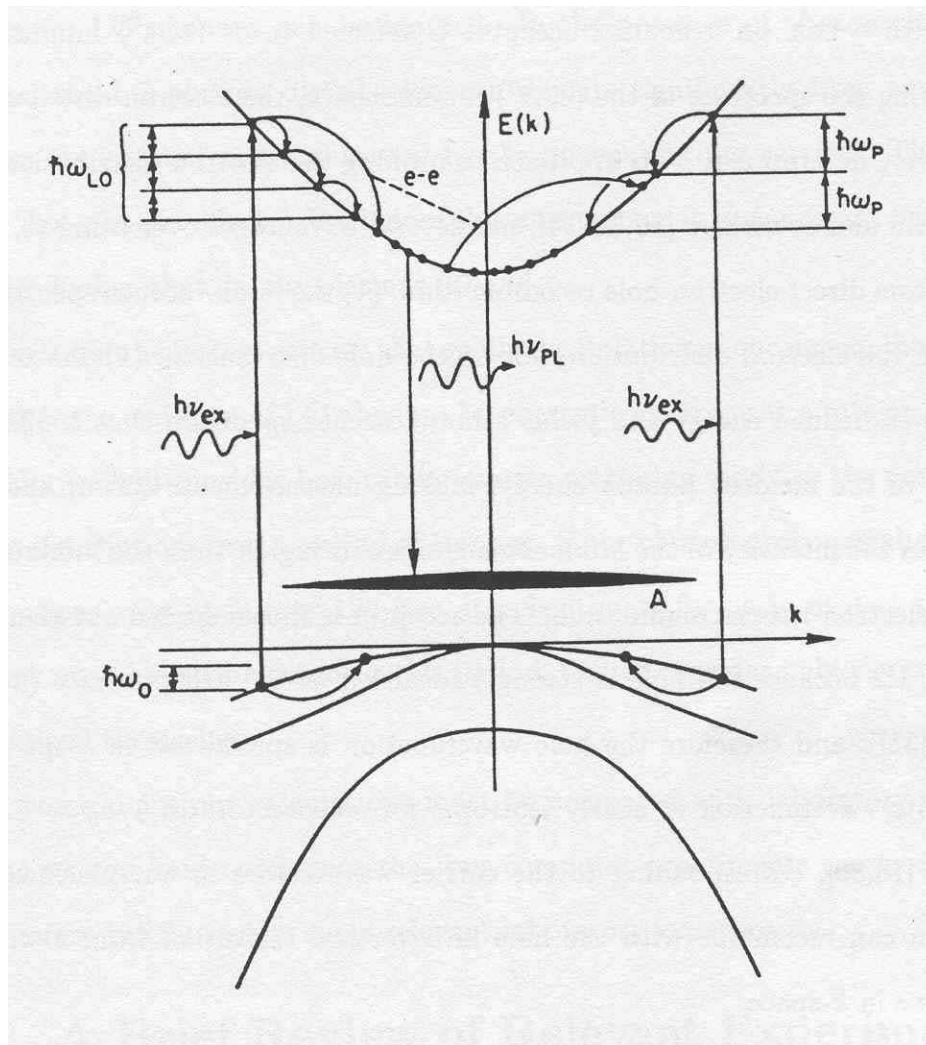


Figure 5.1: Schematic diagram of hot photoluminescence at energy $h\nu_{PL}$ through electron-neutral acceptor (marked by A) recombination. Incident photons with $h\nu_{ex}$ excite electrons, and subsequent scattering processes are illustrated including electron-electron, electron-phonon, electron-plasmon scatterings. (quoted from Ref.[21])

q_z is quantized. The half-space phonons, whose z component of the phonon wave vector is not restricted, propagate in the barrier. Symmetric interface phonons propagate along the interface, and the in-plane atomic displacement is symmetric with respect to the center of the well. Symmetric interface mode can be further divided into the S+ and the S- branches. These two phonon branches also have different dispersion characteristics, which is given by the solution of

$$\varepsilon_{\text{latt},1}(\omega_{S\pm}) \tanh(q_{//}L/2) + \varepsilon_{\text{latt},2}(\omega_{S\pm}) = 0 \quad (5.1)$$

where the lattice dielectric function is given by

$$\varepsilon_{\text{latt},n}(\omega_{S\pm}) = \varepsilon_{\infty n} \frac{\omega_{S\pm}^2 - \langle \omega_{\text{LO}n} \rangle^2}{\omega_{S\pm}^2 - \langle \omega_{\text{TO}n} \rangle^2} \quad (5.2)$$

where the optical phonon energy in the $\text{Al}_x\text{Ga}_{1-x}\text{As}$ layer has two modes: the GaAs-like mode and the AlAs-like mode. $\langle \omega_{\text{LO}1(\text{TO}1)} \rangle$ represents the LO (TO) energy in the GaAs layer. $\langle \omega_{\text{LO}2(\text{TO}2)} \rangle$ represents the LO (TO) energy in the $\text{Al}_x\text{Ga}_{1-x}\text{As}$ layer, and is taken as the average of those of the AlAs-like mode $\omega_{\text{LO}2(\text{TO}2)}^{\text{AlAs}}(x)$ and the GaAs-like mode $\omega_{\text{LO}2(\text{TO}2)}^{\text{GaAs}}(x)$

$$\langle \omega_{\text{LO}2(\text{TO}2)} \rangle = x\omega_{\text{LO}2(\text{TO}2)}^{\text{AlAs}}(x) + (1-x)\omega_{\text{LO}2(\text{TO}2)}^{\text{GaAs}}(x) \quad (5.3)$$

The material parameters used in the dissertation are listed in Table II²². Fig. 5.2 shows an example of the interface phonon dispersion in a 50nm-width GaAs/ $\text{Al}_{0.3}\text{Ga}_{0.7}\text{As}$ quantum well. At the long wave length limit, the S+ and the S- interface modes go to the LO phonon energy in AlGaAs barrier and TO energy in GaAs well, respectively, while the antisymmetric plus (A+) and the antisymmetric minus (A-) interface modes go to the LO phonon energy in GaAs well and TO energy in AlGaAs barrier. At the short wave length limit, the S+ and the A+ modes go to the

TABLE II. Material parameters for GaAs, AlAs and $\text{Al}_x\text{Ga}_{1-x}\text{As}$ used in the dissertation

Parameter	GaAs	AlAs	$\text{Al}_x\text{Ga}_{1-x}\text{As}$
LO-phonon energy $\hbar\omega_{\text{LO}}$ (meV)			
GaAs-type	36.25		$36.25-6.55x+1.79x^2$
AlAs type		50.09	$44.63+8.78x-3.32x^2$
TO-phonon energy $\hbar\omega_{\text{TO}}$ (meV)			
GaAs-type	33.29		$33.29-0.64x-1.16x^2$
AlAl type		44.88	$44.63+0.05x-0.30x^2$
Relative dielectric constant			
Static κ_s	13.18	10.06	$13.18-3.12x$
High frequency κ_∞	10.89	8.16	$10.89-2.73x$
Band-gap energy $E_g^\Gamma(15\text{K})$ (eV)	1.519	3.13	$1.519+1.611x$
Electron's effective mass $m_e(m_0)^a$	0.067	0.15	$0.067+0.083x$

^a m_0 denotes the free electron mass.

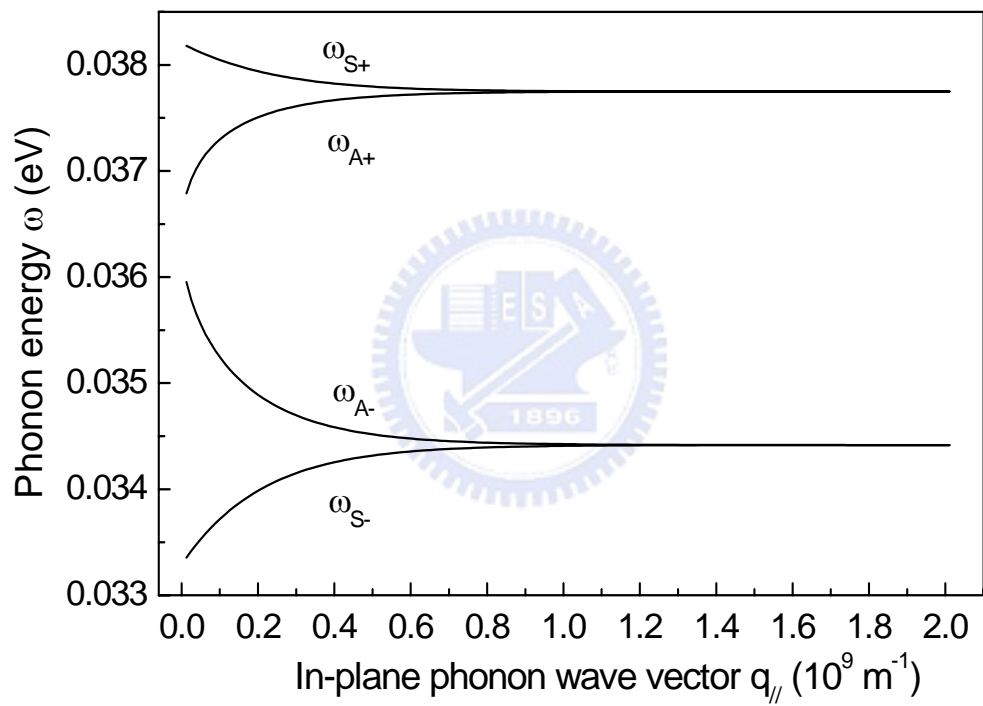


Figure 5.2: Dispersion curves of symmetric and anti-symmetric interface phonon modes in a 50nm GaAs/Al_{0.3}Ga_{0.7}As quantum well.

same phonon energy while the S- and the A- go to the same energy. The long-wave-length phonons play a more important role on the scattering with electrons because the Fröhlich interaction inversely proportional to the phonon's wave vector, which favors the small-angle scattering. The anti-symmetric interface phonons become important on the interaction with electrons when the electron has intersubband scatterings.

5.2.2 Electron-Phonon Scattering Rates

With the average phonon energy in $\text{Al}_x\text{Ga}_{1-x}\text{As}$ alloy shown in eq.(5.3), intrasubband electron-optical-phonon scattering rates in the lowest subband can be calculated using the Fermi's golden rule. The scattering rates are obtained by integrating over all possible states using the two-dimensional density of state function with states restricted by energy and momentum conservations. Scattering rates of the interface modes, $W_{S\pm}$, the confined mode, W_C , and the half-space mode, W_{HS} , are respectively written as

$$W_{S\pm} = \frac{e^2}{4\pi\epsilon_0\hbar^3k} \sum_{n=1,2} \left\{ m_{en} \int_{q_{//\min}}^{q_{//\max}} \frac{\omega_{S\pm}}{q_{//}} [N_{q_{//}}(\omega_{S\pm}) + 1] |\langle \phi_f | \phi_{S\pm} | \phi_i \rangle|^2 \times \left\{ [h_1^{-1}(\omega_{S\pm}) \tanh(\frac{1}{2}q_{//}L) + h_2^{-1}(\omega_{S\pm})] \right\}^{-1} dq_{//} \right\} \quad (5.4)$$

$$W_C = \frac{m_{e1}e^2\omega_C}{\pi^2\hbar^3k} \left(\frac{1}{\epsilon_{\infty 1}} - \frac{1}{\epsilon_{S1}} \right) [N_{q_{//}}(\omega_C) + 1] \sum_p \frac{1}{p} \times \left\{ |\langle \phi_f | \phi_C | \phi_i \rangle|^2 \left[\tan^{-1}\left(\frac{q_{//\max}L_w}{p\pi}\right) - \tan^{-1}\left(\frac{q_{//\min}L_w}{p\pi}\right) \right] \right\} \quad (5.5)$$

$$W_{HS} = \frac{m_{e2}e^2\omega_{HS}}{2\pi^2\hbar^3k} \left(\frac{1}{\epsilon_{\infty 2}} - \frac{1}{\epsilon_{S2}} \right) [N_{q_{//}}(\omega_{HS}) + 1] \times \int_0^{\infty} \frac{1}{q_z} |\langle \phi_f | \phi_{HS} | \phi_i \rangle|^2 \left[\tan^{-1}\left(\frac{q_{//\max}}{q_z}\right) - \tan^{-1}\left(\frac{q_{//\min}}{q_z}\right) \right] dq_z \quad (5.6)$$

$N_{q_{//}}(\omega_{S\pm})$, $N_{q_{//}}(\omega_C)$, and $N_{q_{//}}(\omega_{HS})$ are phonon occupation numbers of the interface

modes, the confined mode, and the half-space mode respectively. ϕ_i and ϕ_f are the electron's wave functions of the initial and the final states in the quantum well. $\phi_{S\pm}$, ϕ_C , and ϕ_{HS} , given in Table III, are the potential functions of the interface, the confined, and the half-space modes respectively. The function, $h_n(\omega_{S\pm})$, is expressed as

$$h_n(\omega_{q_{//}, S\pm}) = \left(\frac{1}{\kappa_{\infty n}} - \frac{1}{\kappa_{0n}} \right) \left(\frac{\langle \omega_{LOn} \rangle^2}{\omega_{S\pm}^2} \right) \left(\frac{\omega_{S\pm}^2 - \langle \omega_{TO n} \rangle^2}{\langle \omega_{LO n} \rangle^2 - \langle \omega_{TO n} \rangle^2} \right)^2 \quad (5.7)$$

The minimum and maximum in-plane phonon wave vector can be expressed as

$$q_{//\min} = k \left[1 - (\hbar \omega_{LO} / E_k) \right]^{1/2} \quad (5.8a)$$

$$q_{//\max} = k \left[1 + (\hbar \omega_{LO} / E_k) \right]^{1/2} \quad (5.8b)$$

In order to clearly explain the dependence of scattering rates on the structure parameters for the interface modes, we introduce the H factor, defined as

$$H = [h_1^{-1}(\omega_{S\pm}) \tanh\left(\frac{1}{2} q_{//} L_w\right) + h_2^{-1}(\omega_{S\pm})]^{-1} \quad (5.9)$$

It appears in the eq. (5.4) for the interface modes. In addition, we call the overlap integral, $\langle \phi_f | \phi | \phi_i \rangle$, for the electric potential G factors for the phonon modes. For S+ and S- modes, the G factors in the well and the barrier are respectively

$$G_{S\pm}^w = \frac{2 / \cosh\left(\frac{1}{2} q_{//} L_w\right)}{\frac{\hbar}{\sqrt{2m_{e2}(\Delta E_C - E_{e1})}} \left[1 + \cos\left(\frac{\sqrt{2m_{e1}E_{e1}}}{\hbar} L_w\right) \right] + L_w + \frac{\hbar}{\sqrt{2m_{e1}E_{e1}}} \sin\left(\frac{\sqrt{2m_{e1}E_{e1}}}{\hbar} L_w\right)} \times \left[\frac{1}{q_{//}} \sinh\left(\frac{1}{2} q_{//} L_w\right) + \frac{q_{//} \sinh\left(\frac{1}{2} q_{//} L_w\right) \cos\left(\frac{\sqrt{2m_{e1}E_{e1}}}{\hbar} L_w\right)}{q_{//}^2 + \frac{8m_{e1}E_{e1}}{\hbar^2}} + \frac{2\sqrt{2m_{e1}E_{e1}} \cosh\left(\frac{1}{2} q_{//} L_w\right) \sin\left(\frac{\sqrt{2m_{e1}E_{e1}}}{\hbar} L_w\right)}{q_{//}^2 + \frac{8m_{e1}E_{e1}}{\hbar^2}} \right] \quad (5.10)$$

$$G_{S\pm}^b = \frac{4}{q_{//} + \frac{\sqrt{8m_{e2}(\Delta E_C - E_{e1})}}{\hbar}} \times \frac{\cos^2\left(\frac{\sqrt{2m_{e1}E_{e1}}}{2\hbar}L_w\right)}{\frac{\hbar}{\sqrt{2m_{e2}(\Delta E_C - E_{e1})}}[1 + \cos\left(\frac{\sqrt{2m_{e1}E_{e1}}}{\hbar}L_w\right)] + L_w + \frac{\hbar}{\sqrt{2m_{e1}E_{e1}}}\sin\left(\frac{\sqrt{2m_{e1}E_{e1}}}{\hbar}L_w\right)} \quad (5.11)$$

The G factor for the p_{th} confined mode and the half-space mode are respectively

$$G_C^p = \frac{L_w}{\pi} + \frac{1}{2} \left\{ \frac{\sin\left[\left(\frac{p\pi}{L_w} - \frac{\sqrt{8m_{e1}E_{e1}}}{\hbar}\right)\frac{L_w}{2}\right]}{\frac{p\pi}{L_w} - \frac{\sqrt{8m_{e1}E_{e1}}}{\hbar}} + \frac{\sin\left[\left(\frac{p\pi}{L_w} + \frac{\sqrt{8m_{e1}E_{e1}}}{\hbar}\right)\frac{L_w}{2}\right]}{\frac{p\pi}{L_w} + \frac{\sqrt{8m_{e1}E_{e1}}}{\hbar}} \right\}, p: \text{odd} \quad (5.12a)$$

$$G_C^p = 0, \quad p: \text{even} \quad (5.12b)$$

$$G_{HS} = \frac{q_z}{\frac{8m_2(\Delta E_C - E_{e1})}{\hbar^2} + q_z^2} \times \frac{4\cos^2\left(\frac{\sqrt{2m_{e1}E_{e1}}}{2\hbar}L_w\right)}{\frac{\hbar}{\sqrt{2m_{e2}(\Delta E_C - E_{e1})}}[1 + \cos\left(\frac{\sqrt{2m_{e1}E_{e1}}}{\hbar}L_w\right)] + L_w + \frac{\hbar}{\sqrt{2m_{e1}E_{e1}}}\sin\left(\frac{\sqrt{2m_{e1}E_{e1}}}{\hbar}L_w\right)} \quad (5.13)$$

where E_{e1} is the electron's ground-state energy, and ΔE_C is the barrier height of the quantum well. The G factor for the intersubband scattering is in Appendix C.

We used the DCM instead of the HZM⁸ for the boundaries' treatment. It is because the scattering rate calculated by HZM gives an unreasonably large scattering rate even with very narrow well width due to the slow convergence of the higher order's modes. The RPA was used for the dynamical screening^{23,24}.

TABLE III. The potential in a quantum well for various phonon modes

Optical-phonon mode	Potential for three distinct regions		
	$z \leq -\frac{L_w}{2}$	$-\frac{L_w}{2} < z \leq \frac{L_w}{2}$	$z > \frac{L_w}{2}$
Symmetric interface $\phi_{S\pm}$	$e^{q_{//}(z+\frac{L_w}{2})}$	$\cosh(q_{//}z)/\cosh(q_{//}L_w/2)$	$e^{-q_{//}(z-\frac{L_w}{2})}$
Anti-symmetric interface $\phi_{A\pm}$	$-e^{q_{//}(z+\frac{L_w}{2})}$	$\sinh(q_{//}z)/\sinh(q_{//}L_w/2)$	$e^{-q_{//}(z-\frac{L_w}{2})}$
Confined ϕ_c		$\cos(\frac{n\pi z}{L_w}),$ n: odd	
		$\sin(\frac{n\pi z}{L_w}),$ n: even	
Half-Space ϕ_{HS}	$\sin[q_z(z+\frac{1}{2}L_w)]$		$\sin[q_z(z-\frac{1}{2}L_w)]$

5.3 Intraband Scattering

In our calculations, band-offset ratio $\Delta E_c : \Delta E_v$ in GaAs/Al_xGa_{1-x}As quantum wells was chosen to be 65:35. The electrons were given an excess energy of 50meV so that the intersubband transition can be neglected. The sheet-charge density was chosen to be $5 \times 10^{10} \text{ cm}^{-2}$.

In Fig. 5.3 we show the dependence of the phonon energy of the S+ mode and the S- mode on the Al composition in the barrier at the minimum $q_{//\text{min}}$ and the maximum $q_{//\text{max}}$ in-plane phonon wave vectors with a well width of 5nm. For the S+ mode, the phonon energy increases quickly with the Al composition for both $q_{//\text{min}}$ and $q_{//\text{max}}$. It approaches the LO phonon energy in the barrier layer when $q_{//}$ approaches zero. The increase of the calculated S+ mode energy with Al composition at $q_{//\text{min}}$ agrees with the increased LO phonon energy in Al_xGa_{1-x}As layer as Al composition is increased. For the S- mode, the phonon energy has a weak dependence on the Al composition. It approaches the TO phonon energy of the well when $q_{//}$ approaches zero. The weak dependence on the Al composition is easily understood because there is no Al in the well.

In Fig. 5.4 we show the calculated dependence of electron-optical phonon scattering rates on the Al composition for various types of phonon modes in a 5nm wide GaAs/Al_xGa_{1-x}As quantum well with a lattice temperature of 15K. For the S+ mode, the scattering rate increases from 4.1 ps^{-1} to 6.9 ps^{-1} as the Al composition, x , is increased from 0.2 to 1. In order to interpret the results, we show in Fig. 5.5 (a) the dependence of the H factor and the G factor on $q_{//}$. As we can see, both the H factor and the G factor increase with the Al composition at small $q_{//}$. Since the S+ mode favors the small-angle scattering, this dependence follows the behavior of the H and the G factors at small $q_{//}$. For the S- mode, the scattering rate increases from 0.32 ps^{-1} to 1.1 ps^{-1} as the Al composition is increased from 0.2 to 1. The strong dependence on

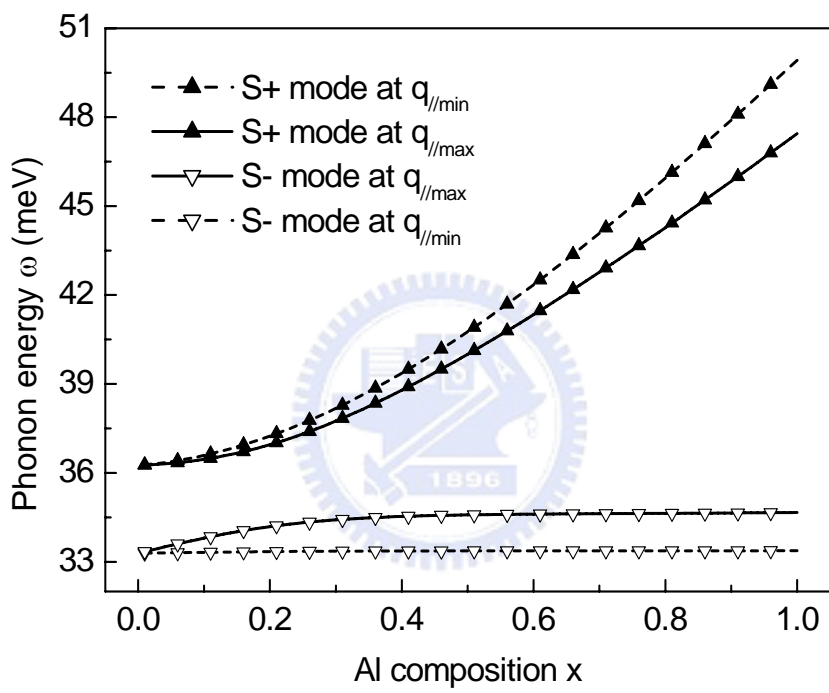


Figure 5.3: Dependence of phonon energy of S+ and S- interface modes on the Al composition at $q_{//min}$ and $q_{//max}$.

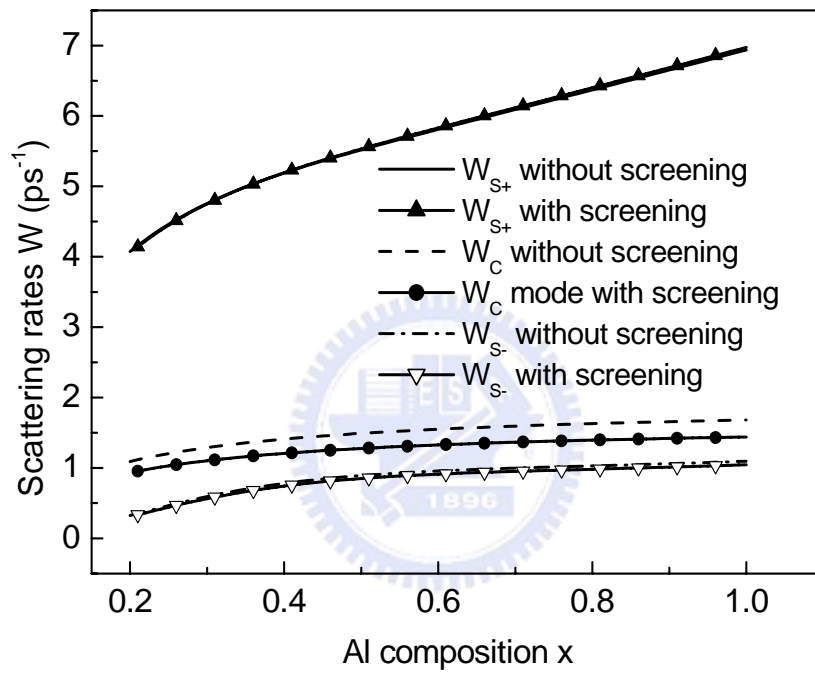
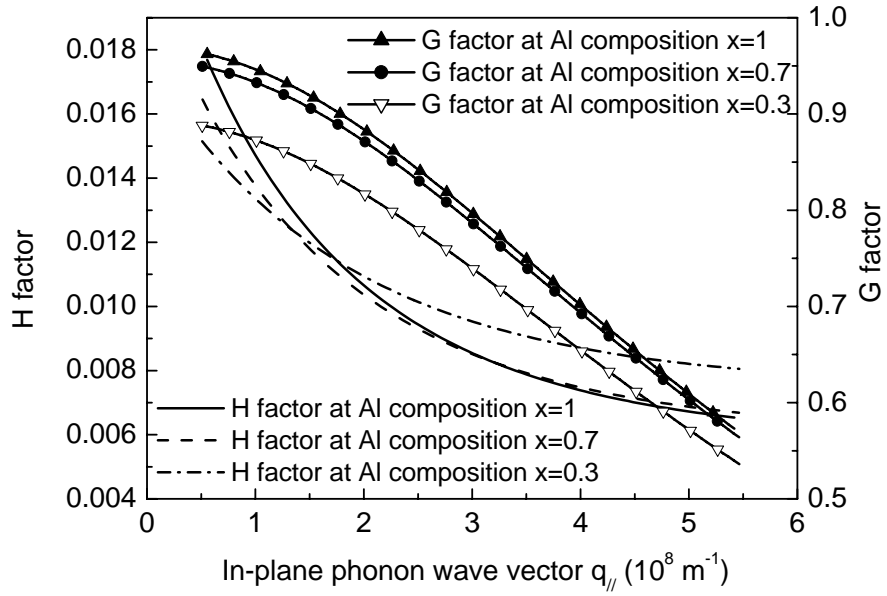


Figure 5.4: Dependence of electron- phonon scattering rate of S+ mode, confined mode, and S- mode on the Al composition. The well width is 5nm, the lattice temperature is 15K, and the amount of the excess kinetic energy of the electron is 50meV.

(a)



(b)

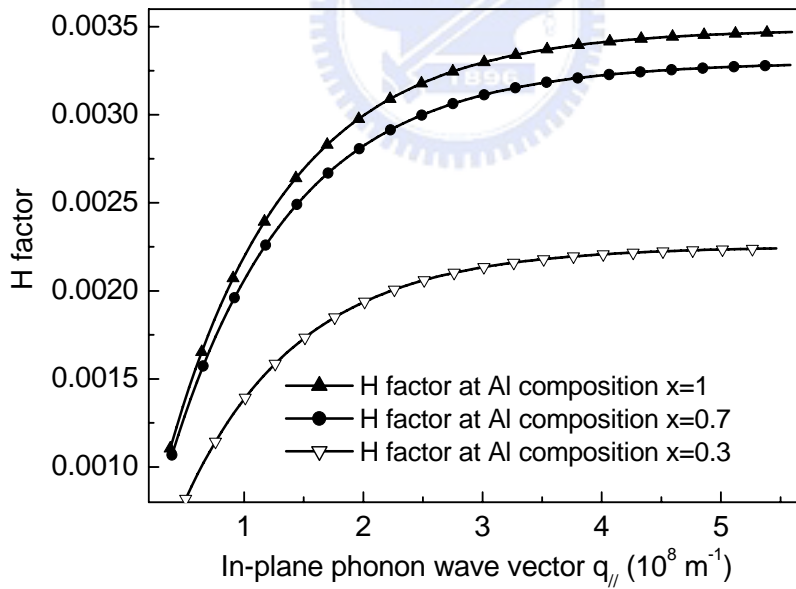


Figure 5.5: Dependence of H and G factors on $q_{||}$ at three Al compositions in the barrier, 0.3, 0.7, and 1. (a) for the S+ mode. (b) for the S- mode.

the Al composition is mostly due to the H factor. In Fig. 5.5(b) we show the dependence of the H factor on $q_{//}$. As $q_{//}$ decreases toward zero, ω_{S-} approaches the TO phonon energy in the well. This leads to the decrease of the H factor. Because of this, the small-angle scattering for the S- mode is not as important as that for other phonon modes. In Fig. 5.4 we have also found that the screening effect for the S+ mode and the S- mode is not significant.

Comparing to the S+ and the S- modes, the scattering rate of the confined phonon mode does not show strong dependence with the Al composition in the range that we have investigated. It is because that the G factor in the expression of the scattering rate equation for the confined phonon mode is less sensitive to the Al composition. The screening effect for the confined mode is stronger than that of the S+ and the S- interface modes.

For the 5nm well the electron wave function does not penetrate deep into the barriers. Therefore, the half-space mode's contribution to the scattering rate is insignificant in comparing to the other three types of phonon modes and is not considered here.

The calculated results were compared with the experimental results²⁰ performed by hot-electron neutral-acceptor luminescence for GaAs/Al_xGa_{1-x}As quantum wells with various Al compositions. The calculated effective phonon energy (ω_{eff}) is given by the following equation.

$$\omega_{\text{eff}} = \frac{W_{S+}\omega_{S+} + W_{S-}\omega_{S-} + W_C\omega_C}{W_{S+} + W_{S-} + W_C} \quad (5.14)$$

In Fig. 5.6 we show the dependence of the effective phonon energy on the Al composition of both the experimental result²⁰ and our calculations. There are two calculated curves in the figure. The solid line represents the results without screening

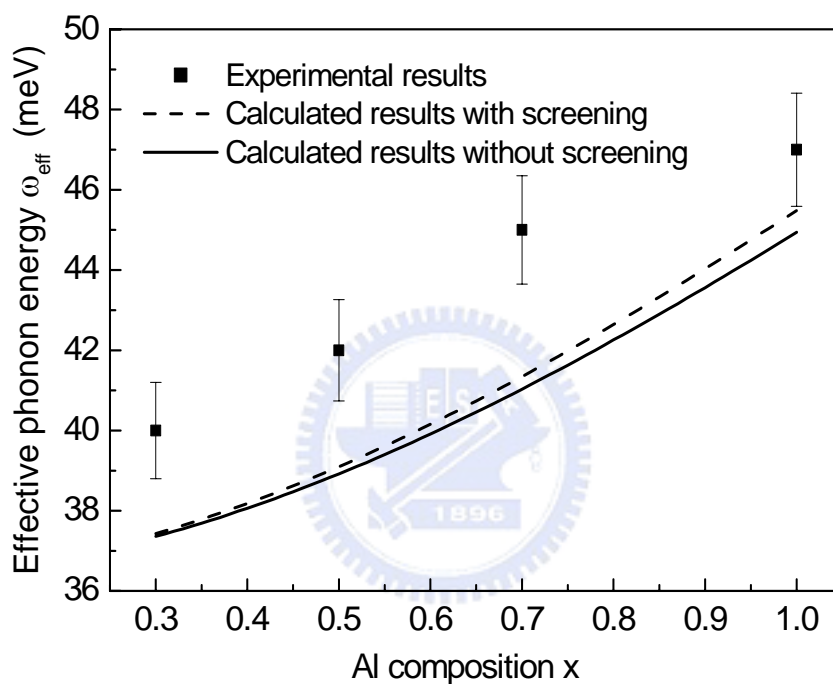


Figure 5.6: Comparison of experimental and calculated results for the dependence of the effective phonon energy on the Al composition. The well width is 5nm, the lattice temperature is 15K, and the amount of the excess kinetic energy of the electron is 180meV.

and the dash one with screening. Since the S+ mode plays the dominant role in the calculated scattering rate among all phonon modes, the calculated effective phonon energy basically follows the behavior of the S+ mode. The tendency of the calculations is in good agreement with the experiments.

The minor difference between the measured result and the calculated result on the effective phonon energy is attributed to the assumptions that we made in the calculations of the average phonon energy in $\text{Al}_x\text{Ga}_{1-x}\text{As}$ alloy, which probably simplified the complexity of the phonon spectrum in the ternary compound.

In Fig. 5.7 we show the dependence of scattering rates on the well width for various types of phonon modes with an Al composition $x=0.3$ in the barriers. Other parameters are kept the same as in previous calculations. For the S+ mode, the scattering rate decreases considerably from 5.3ps^{-1} to 1.4ps^{-1} as the well width is increased from 4nm to 12nm. We attribute this to the decrease of the H factor and the G factor as the well width is increased. When the wells move toward wider wells, the electron wave functions centered at the middle of the well do not spread deep into the interfaces as in the narrower wells. The interface is the place where the strongest electron-phonon interaction took place. Thus, it leads to the decrease of the G factor. But, the tendency on the decrease of the G factor does not hold for extremely small $q_{//}$. As the well gets narrower, the increasing of the G factor has been canceled out by the decreasing of the H Factor and results in the weak dependence for well width narrower than 4nm. This behavior was not found in the earlier calculated results²⁵ where the assumption of an infinite quantum well was made.

For the S- mode, due to the small H factor, the scattering rate is much smaller than the rate of the S+ mode. In addition, the increased H factor with the well width compensates the decreased G factor each other. This results in a weak dependence of scattering rates on the well width.

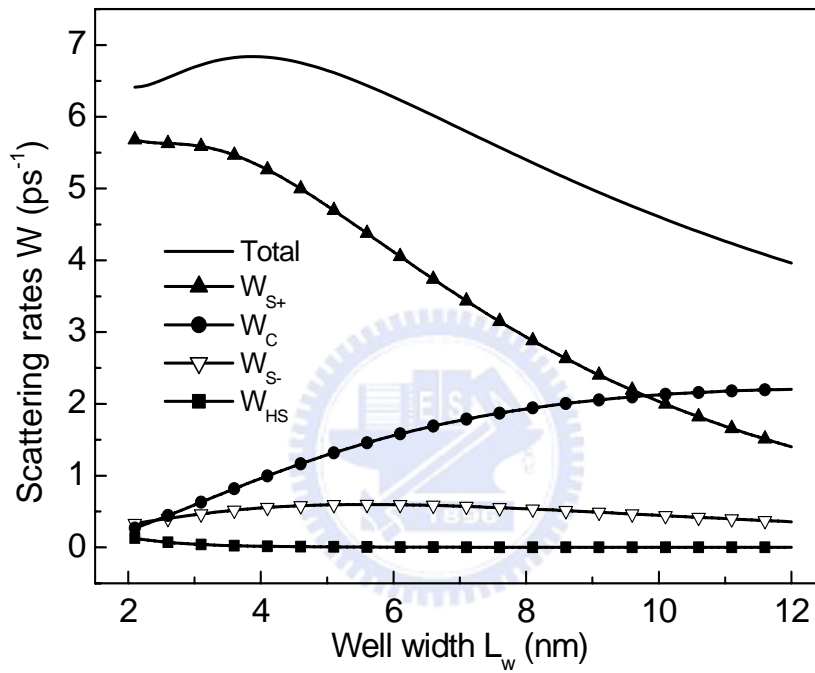


Figure 5.7: Dependence of electron-optical phonon scattering rate of S+ mode, confined mode, S- mode, half-space mode, and the total rate contributed by all types of phonon modes on the well width. The Al composition is 0.3, the lattice temperature is 15K, and the amount of the excess kinetic energy of the electron is 50meV.

The scattering rate of the confined mode increases from 0.27 ps^{-1} to 2.2 ps^{-1} while the rate of the half-space mode decreases sharply from 0.13 ps^{-1} to 0.12 ns^{-1} as the well width is increased from 2nm to 12nm. The increase of the scattering rate of the confined mode is due to the increased G factor as the well width is increased. On the contrary, the G factor decreases for the half-space mode.

There is a crossover point of the scattering rate for the confined mode and the S+ mode at a well width of 10nm and an Al composition of 0.3. So the confined mode is the major relaxation channel for hot electrons in wide quantum wells and the S+ mode is responsible for the narrow wells. Although the total scattering rate only varies slightly with the well width, there still can be a strong dependence of the average electron's energy-loss rate on the well width when the phonon energy of the corresponding modes is considered.

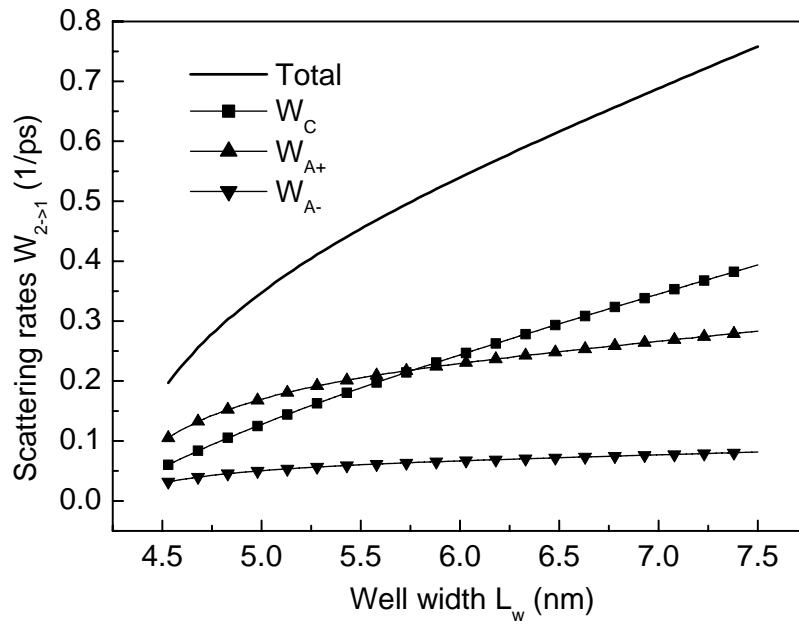
5.4 Intersubband Scattering

Intersubband scattering rate has the better estimation than intrasubband case via Fermi golden rule where the energy-conserved rule is more available in intersubband than intrasubband transition due to one order lower magnitude of scattering rates.

For a two-state quantum well, the increasing intersubband scattering rate with well widths for interface modes is found, shown in Fig. 5.8(a), while the dependence is opposite to the intrasubband case because the moving lower in-plane wave vector due to closing adjacent states gives stronger increased dependence than the decreased Hamiltonian when the well width is increased. The effect of the movement in in-plane phonon wave vector when the well structure is adjusted also leads the different dependence of the Al composition in intersubband transition, shown in Fig. 5.8(b), from the intrasubband case.

For a three-state quantum well, the electron at the highest state shows the faster

(a)



(b)

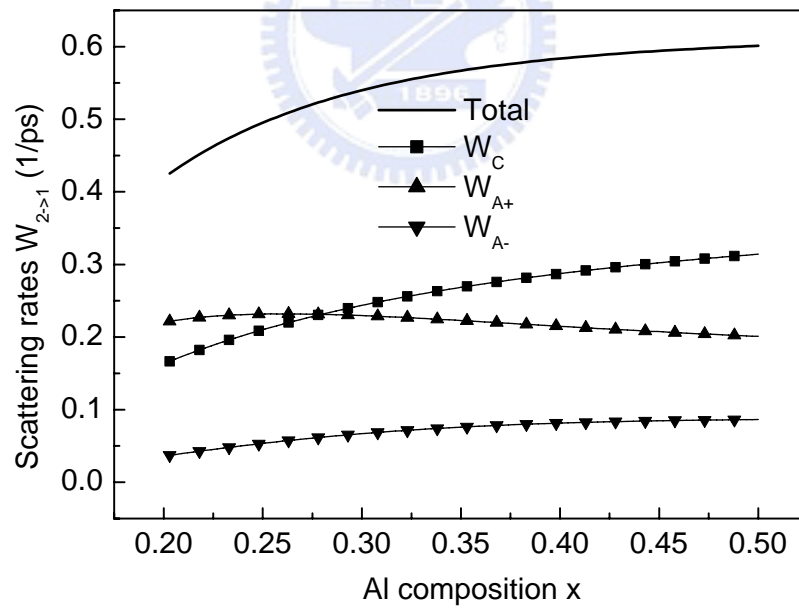


Figure 5.8: Intersubband scattering rate in a two-state quantum well. (a) Al composition $x=0.3$. (b) well width $L_w=6$ nm

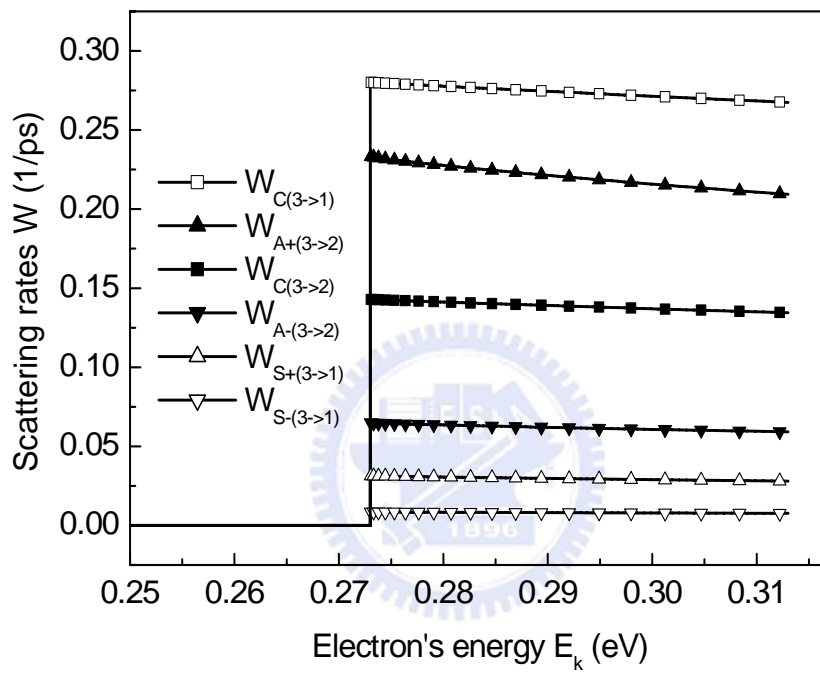


Fig. 5.9: Intersubband scattering rate in a three-state quantum well with well width of 10nm and Al composition of 0.3.

scattering to the ground state than to the first excited state for the confined mode, shown in Fig. 5.9. The result rebuts the sequential state-by-state scattering and implies that the dynamics analysis should be replaced by the time evolution of the electron distribution, which is obtained by solving Boltzmann equation.

References

1. C. H. Yang, J. M. Carlson-Swindle, S. A. Lyon, and J. M. Worlock, Phys. Rev. Lett. **55**, 2359 (1985).
2. R. G. Ulbrich, Phys. Rev. B **8**, 5719 (1973).
3. S. J. Manion, M. Artaki, M. A. Emanuel, J. J. Coleman, and K. Hess, Phys. Rev. B **35**, 9203 (1987).
4. R. Fuchs and K. L. Kliewer, Phys. Rev. **140**, A2076 (1965).
5. J. J. Licari and R. Evrard, Phys. Rev. B **15**, 2254 (1977).
6. N. Mori and T. Ando, Phys. Rev. B **40**, 6175 (1989).
7. R. Chen, D. L. Lin, and Thomas F. George, Phys. Rev. B **41**, 1435 (1990).
8. K. Huang and B. Zhu, Phys. Rev. B **38**, 13377 (1988).
9. A. K. Sood, J. Menendez, M. Cardona, and K. Ploog, Phys. Rev. Lett. **54**, 2111 (1985).
10. A. K. Sood, J. Menendez, M. Cardona, and K. Ploog, Phys. Rev. Lett. **54**, 2115 (1985).
11. A. Seilmeier, H. J. Hubner, G. Abstreiter, G. Weimann, and W. Schlapp, Phys. Rev. Lett. **59**, 1345 (1987).
12. J. K. Jain and S. Das Sarma, Phys. Rev. Lett. **62**, 2305 (1989).
13. K. Leo, W. W. Rühle, and K. Ploog, Phys. Rev. B **38**, 1947 (1988).
14. K. Leo, W. W. Rühle, H. J. Queisser, and K. Ploog, Phys. Rev. B **37**, 7121 (1988).

15. H. Lobentanzer, W. Stolz, J. Nagle, and K. Ploog, *Phys. Rev. B* **39**, 5234 (1989).
16. J. Shah, A. Pinczuk, A. C. Gossard, and W. Wiegmann, *Phys. Rev. Lett.* **54**, 2045 (1985).
17. G. Fasol, W. Hackenberg, H. P. Hughes, K. Ploog, E. Bauser, and H. Kano, *Phys. Rev. B* **41**, 1461 (1990).
18. D. N. Mirlin, B. P. Zakharchenya, I. I. Reshina, A. V. Rodina, V. F. Sapega, A. A. Sirenko, V. M. Ustinov, A. E. Zhukov, and A. Yu. Egorov, *Semicond.* **30**, 377 (1996).
19. V. F. Sapega, M. P. Chamberlain, T. Ruf, M. Cardona, D. N. Mirlin, K. Totemeyer, A. Fischer, and K. Eberl, *Phys. Rev. B* **52**, 14144 (1995).
20. K. W. Sun, H. Y. Chang, C. M. Wang, T. S. Song, S. Y. Wang, and C. P. Lee, *Solid State Commun.* **115**, 563 (2000).
21. M. G. Kane, "Carrier-Carrier Scattering Among Photoexcited Nonequilibrium Carriers in GaAs" (Dissertation of Princeton University, 1994), p.7.
22. S. Adachi, *J. Appl. Phys.* **58**, R1 (1985).
23. T. Ando, A. B. Fowler, and F. Stern, *Rev. Mod. Phys.* **54**, 437 (1982).
24. T. Thoai and H. Haug, *Phys. Status Solidi (B)* **98**, 581 (1980).
25. S. Rudin, and T. L. Reinecke, *Phys. Rev. B* **41**, 7713 (1990).

Chapter 6

Conclusion and Direction

The non-equilibrium carrier-carrier scattering and the hot carrier relaxation in GaAs were theoretically studied by using the Generalized Kadanoff-Baym equation and the semi-classical Boltzmann equation, respectively. The dimensional effect and the dynamical screening on the two fundamental interactions were clarified. In contrast to earlier investigations, the dynamical screening is shown to be stronger in a quantum well than a bulk for both the carrier-carrier and the carrier-phonon interactions. The electric flux in a lower dimension has a stronger confinement so that has a stronger electric field. The stronger dynamical screening in a lower dimension is as a result of larger difference between the unscreened and the screened electric fields. Although the carrier in a bulk has a weaker Coulomb interaction, a higher dimension leading to more scattering channels overcomes the effect and gives rise to a rapider thermalization of non-equilibrium carriers and a faster relaxation of hot carriers in a bulk. In the quantum kinetic regime, the memory effect on the carrier-carrier scattering is firstly demonstrated to have a burning hole on the carrier's distribution, which is the early stage of oscillation. As the time further goes, the one burning hole and two hills around the hole will continue to evolve to two burning holes and three hills. The process will go on until the carrier dephases or thermalizes.

The next step is to extend the quantum kinetic theory to the curved space time where the semi-classical Boltzmann equation has been established¹. The current quantum kinetic theory has already been developed for relativistic particles by using

the Wigner function; however, it has not been reached to the generalized coordinate yet². Starting from the quantum field theory in the curved space time³, the non-equilibrium Green function will be used to derive the relativistic quantum kinetic equation with the Robertson-Walker and the Schwarzschild metrics. The non-equilibrium Green function is chosen rather than the Wigner function to explore the quantum kinetic theory because the quantum statistical method in the Wigner function is principally semiclassical, which is not valid for carrier kinetics on the ultrashort-time and ultrasmall-space scales and the important information in the quantum kinetic regime such as the memory effect and the energy non-conservation is lost.

By constructing the theoretical framework, the evolution of the universe at the different stages will be studied. First of all, the singular point of the infinite curvature space time at the moment of the big bang could be eliminated by using the quantum statistical method. Second, the kinetics of the rapid expanding universe where the SU(5) and subsequent symmetries break will be paid the attention to study the emitting and the cooling dynamics of the kinds of particles during different periods of the separating fundamental interactions, where the quantum kinetic effects of non-Markovian process and non-conserving events will be addressed. As the time evolves, the coherent behavior of the dynamical state evanesces due to abundant collisions among these non-equilibrium particles, and the carrier kinetics can be simplified to govern by the semi-classical Boltzmann equation. When the hydrodynamic regime is entered, the subsequent degree of approximations on the kinetic equation can be made to study the large-scale fluid dynamics such as the formation of galaxies clusters and the mechanics in the blackhole where the Hawking radiation will be considered. The simplified kinetic equation can be obtained by using the Chapman-Enskog expansion and the Maxwell-Grad method to derive the

Navier-stokes, and Burnett equations where the deviated distribution function from the equilibrium is in terms of hydrodynamic velocity, temperature, particle density, etc., and their gradients. Eventually, the validity or the precise valid range of the Birkhoff-Khinchin ergodic theorem, where there exists an asymptotic distribution function when the ensemble numbers are large enough, will be examined or probed, respectively, by using the theoretical investigation on the varieties of astronomy objects and the observational Cosmological results.

References

1. C. Cercignani and G. M. Kremer, *The Relativistic Boltzmann Equations: theory and applications* (Birkhauser, Basel, 2002).
2. S. R. de Groot, W. A. van Leeuwen, and C. G. van Weert, *Relativistic Kinetic Theory: principles and applications* (North-Holland, Amsterdam, 1980).
3. N. D. Birrell and P. C. W. Davies, *Quantum Fields in Curved Space* (Cambridge University, New York, 1982).

APPENDIX A

Calculating Interband Coulomb

Quantum Kinetics

At the initial stage of non-equilibrium carrier excited by the ultrafast pulse laser, before the screening developed, the interband Coulomb quantum kinetics can be modeled by the simplified GKBE as follows[†]

$$\frac{\partial P_{\mathbf{k}_1}}{\partial t} = \left. \frac{\partial P_{\mathbf{k}_1}}{\partial t} \right|_{\text{coh.}} + \left. \frac{\partial P_{\mathbf{k}_1}}{\partial t} \right|_{\text{scatt.}} \quad (\text{A.1a})$$

$$\frac{\partial f_{j,\mathbf{k}_1}}{\partial t} = \left. \frac{\partial f_{j,\mathbf{k}_1}}{\partial t} \right|_{\text{coh.}} + \left. \frac{\partial f_{j,\mathbf{k}_1}}{\partial t} \right|_{\text{scatt.}} \quad (\text{A.1b})$$

where $P_{\mathbf{k}_1}$ and f_{j,\mathbf{k}_1} denotes the polarization field and the carrier's distribution at the electron and the hole bands ($j=e, h$).

$$\left. \frac{\partial P_{\mathbf{k}_1}(t)}{\partial t} \right|_{\text{coh.}} = \frac{i}{\hbar} \left[\frac{d_{\mathbf{k}_1} E_0(t)}{2} (1 - f_{e,\mathbf{k}_1}(t) - f_{h,\mathbf{k}_1}(t)) - \delta_{\mathbf{k}_1} P_{\mathbf{k}_1}(t) \right] \quad (\text{A.2a})$$

$$\left. \frac{\partial f_{j,\mathbf{k}_1}(t)}{\partial t} \right|_{\text{coh.}} = \frac{1}{\hbar} \text{Im} [d_{\mathbf{k}_1} E_0(t) P_{\mathbf{k}_1}(t)] \quad (\text{A.2b})$$

$$\begin{aligned} \left. \frac{\partial P_{\mathbf{k}_1}}{\partial t} \right|_{\text{scatt.}} &= -\frac{4}{\hbar^2} \sum_{\mathbf{k}_3} \int_{-\infty}^t dt' V_{\mathbf{q}=\mathbf{k}_1-\mathbf{k}_3}^2 [P_{\mathbf{k}_1}(t') - P_{\mathbf{k}_3}(t')] \\ &\quad \times \left\{ \sum_{j=e,h} \sum_{\mathbf{k}_2} f_{j,\mathbf{k}_2}(t') [1 - f_{j,\mathbf{k}_4}(t')] - \text{Re} [P_{\mathbf{k}_4}(t') P_{\mathbf{k}_2}^*(t')] \right\} \end{aligned} \quad (\text{A.3a})$$

$$\begin{aligned} \left. \frac{\partial f_{j,\mathbf{k}_1}}{\partial t} \right|_{\text{scatt.}} &= -\frac{4}{\hbar^2} \sum_{\mathbf{k}_3} \int_{-\infty}^t dt' V_{\mathbf{q}=\mathbf{k}_1-\mathbf{k}_3}^2 [f_{j,\mathbf{k}_1}(t') - f_{j,\mathbf{k}_3}(t')] \\ &\quad \times \left\{ \sum_{j=e,h} \sum_{\mathbf{k}_2} f_{j,\mathbf{k}_2}(t') [1 - f_{j,\mathbf{k}_4}(t')] - \text{Re} [P_{\mathbf{k}_4}(t') P_{\mathbf{k}_2}^*(t')] \right\} \end{aligned} \quad (\text{A.3b})$$

where $\delta_{\mathbf{k}_1}$ is equal to $E_{e,\mathbf{k}_1} + E_{h,\mathbf{k}_1} + E_g - \hbar\omega_0$. ω_0 is the central frequency of optical source. $\mathbf{d}_{\mathbf{k}_1}$ and $E_0(t)$ are the dipole moment and the excitation electric field, and can be expressed as

$$\mathbf{d}_{\mathbf{k}_1} E_0(t) = A(t) \mathbf{p}_{cv} (e/m_e) \quad (\text{A.4})$$

where \mathbf{p}_{cv} is the momentum matrix. The 2D and 3D matrices with TE polarization transition from heavy hole to conduction bands can be written as respectively⁺⁺,

$$\mathbf{p}_{cv}^{2D} = \frac{\sqrt{3}}{2} \sqrt{1 + \frac{E_{e1} + |E_{h1}|}{E_{e1} + |E_{h1}| + \hbar^2 \mathbf{k}^2 / 2m_r}} \sqrt{m_0 E_p / 6} \quad (\text{A.5a})$$

$$\mathbf{p}_{cv}^{3D} = \sqrt{m_0 E_p / 6} \quad (\text{A.5b})$$

where m_r is $(m_e^{-1} + m_h^{-1})^{-1}$ and E_p is equal to 25eV. $A(t)$ is the magnetic vector potential and can be written as⁺⁺⁺

$$A(t) = \frac{1}{\omega \sqrt{\epsilon_\infty}} \sqrt{\frac{4\hbar \cosh^{-1} 2}{\sigma \tau_0} \frac{E_{\text{pulse}}}{V} \sqrt{\frac{\ln 2}{\pi} \operatorname{sech}^2\left(\frac{2t \cosh^{-1} 2}{\tau_0}\right)} \exp\left(-\frac{4 \ln 2}{\sigma^2} (\hbar\omega - \hbar\omega_0)^2\right)} \quad (\text{A.6})$$

where an initial Gaussian distribution with the time dependence of $\operatorname{sech}^2(2t \cosh^{-1} 2 / \tau_0)$ is assumed. τ_0 is the temporal pulse width. E_{pulse} is the energy per pulse. σ is the standard deviation. ω is equal to $(E_{e,\mathbf{k}_1} + E_{h,\mathbf{k}_1} + E_g) / \hbar$.

The scattering terms can be derived in distinct dimensions.

$$\begin{aligned} \left. \frac{\partial P_{\mathbf{k}_1}}{\partial t} \right|_{2D, \text{scatt.}} &= -\frac{m_e^2 e^4}{2\epsilon_\infty^2 \pi^4 \hbar^6 k_1} \int_{-\infty}^t dt' \int_{E_{e1}}^{\infty} \frac{dE_{k_3}}{\sqrt{E_{k_3} - E_{e1}}} \int_{|k_1 - k_3|}^{k_1 + k_3} \frac{dq}{q^2} \frac{[P_{\mathbf{k}_1}(t') - P_{\mathbf{k}_3}(t')]}{\sqrt{1 - \left(\frac{k_1^2 + k_3^2 - q^2}{2k_1 k_3}\right)^2}} \\ &\times \sum_{j=e,h} \int_{E_{e1}}^{\infty} \frac{dE_{k_2}}{\sqrt{E_{k_2} - E_{e1}}} \int_{\Delta_{\min}}^{\Delta_{\max}} d\Delta \frac{f_{j,\mathbf{k}_2}(t') [1 - f_{j,\mathbf{k}_4}(t')] - \operatorname{Re}[P_{\mathbf{k}_4}(t') P_{\mathbf{k}_2}^*(t')]}{\sqrt{1 - \left(\frac{2m_e (E_{k_1} + E_{k_2} - E_{k_3} - E_{e1} - \Delta) - q^2 - k_2^2}{2qk_2}\right)^2}} \quad (\text{A.7a}) \end{aligned}$$

$$\left. \frac{\partial P_{k_1}}{\partial t} \right|_{3D,scatt.} = -\frac{m_e^3 e^4}{\varepsilon_\infty^2 \pi^4 \hbar^8 k_1} \int_{-\infty}^t dt' \int_0^\infty dE_{k_3} \int_{|k_1-k_3|}^{k_1+k_3} \frac{dq}{q^4} [P_{k_1}(t') - P_{k_3}(t')] \\ \times \sum_{j=e,h0} \int dE_{k_2} \int_{\Delta_{min}}^{\Delta_{max}} d\Delta [f_{j,k_2}(t')[1 - f_{j,k_4}(t')] - \text{Re}[P_{k_4}(t')P_{k_2}^*(t')]] \quad (\text{A.7b})$$

$$\left. \frac{\partial f_{j,k_1}}{\partial t} \right|_{2D,scatt.} = -\frac{m_e^2 e^4}{2\varepsilon_\infty^2 \pi^4 \hbar^6 k_1} \int_{-\infty}^t dt' \int_{E_{e1}}^\infty \frac{dE_{k_3}}{\sqrt{E_{k_3} - E_{e1}}} \int_{|k_1-k_3|}^{k_1+k_3} \frac{dq}{q^2} \frac{[f_{j,k_1}(t') - f_{j,k_3}(t')]}{\sqrt{1 - \left(\frac{k_1^2 + k_3^2 - q^2}{2k_1 k_3} \right)^2}} \\ \times \sum_{j=e,hE_{e1}} \int \frac{dE_{k_2}}{\sqrt{E_{k_2} - E_{e1}}} \int_{\Delta_{min}}^{\Delta_{max}} d\Delta \frac{f_{j,k_2}(t')[1 - f_{j,k_4}(t')] - \text{Re}[P_{k_4}(t')P_{k_2}^*(t')]}{\sqrt{1 - \left(\frac{\frac{2m_e}{\hbar^2} (E_{k_1} + E_{k_2} - E_{k_3} - E_{e1} - \Delta) - q^2 - k_2^2}{2qk_2} \right)^2}} \quad (\text{A.8a})$$

$$\left. \frac{\partial f_{j,k_1}}{\partial t} \right|_{3D,scatt.} = -\frac{m_e^3 e^4}{\varepsilon_\infty^2 \pi^4 \hbar^8 k_1} \int_{-\infty}^t dt' \int_0^\infty dE_{k_3} \int_{|k_1-k_3|}^{k_1+k_3} \frac{dq}{q^4} [f_{j,k_1}(t') - f_{j,k_3}(t')] \\ \times \sum_{j=e,h0} \int dE_{k_2} \int_{\Delta_{min}}^{\Delta_{max}} d\Delta [f_{j,k_2}(t')[1 - f_{j,k_4}(t')] - \text{Re}[P_{k_4}(t')P_{k_2}^*(t')]] \quad (\text{A.8b})$$

where k_4 is equal to $k_1+k_2-k_3$. The parabolic electronic band structure was used

[†]H. Haug and A. -P Jauho, “Quantum Kinetics in Transport and Optics of Semiconductors” 2nd ed. (Springer, Berlin, 1998), p.280-284.

^{**}S. L. Chuang, “Physics of Optoelectronic Devices” (John Wiley & Sons, New York, 1995), p.370-372.

^{***}G. D. Sanders, C. K. Sun, J. G. Fujimoto, H. K. Choi, C. A. Wang, and C. J. Stanton Phys. Rev. B **50**, 8539 (1994).

APPENDIX B

Calculating Building Up of

Screening

After the non-equilibrium carrier generated, the shielding potential gradually builds up as the time evolves and it can be modeled by the GKBE where the RPA was used^{*}.

$$\begin{aligned}
 \left. \frac{\partial f_{\mathbf{k}_1}}{\partial t} \right|_{\text{scatt.}} &= -\frac{2}{\hbar^2} \sum_{\mathbf{k}_2, \mathbf{k}_3} \int_{-\infty}^t dt' \left[G_{\mathbf{k}_3}^r(t, t') G_{\mathbf{k}_1}^a(t', t) ([1 - f_{\mathbf{k}_3}(t')] f_{\mathbf{k}_1}(t')) \int_{-\infty}^{t'} dt_2 V_{s,q}^a(t_2, t') \right. \\
 &\quad \times \left\{ \int_{-\infty}^{t_2} dt_1 V_{s,q}^r(t, t_1) G_{\mathbf{k}_4}^a(t_1, t_2) G_{\mathbf{k}_2}^r(t_2, t_1) [1 - f_{\mathbf{k}_4}(t_1)] f_{\mathbf{k}_2}(t_1) + \int_{t_2}^t dt_1 V_{s,q}^r(t, t_1) G_{\mathbf{k}_4}^r(t_1, t_2) \right. \\
 &\quad \left. \left. \times G_{\mathbf{k}_2}^a(t_2, t_1) [1 - f_{\mathbf{k}_4}(t_2)] f_{\mathbf{k}_2}(t_2) \right\} - (f \leftrightarrow (1-f)) \right] - \left[\mathbf{k}_1 \leftrightarrow \mathbf{k}_3, \mathbf{k}_2 \leftrightarrow \mathbf{k}_4, V_{s,q}^{r,a} \leftrightarrow (V_{s,q}^{r,a})^* \right] \quad (\text{B.1})
 \end{aligned}$$

where the $f \leftrightarrow (1-f)$ denotes the interchanging term. The retarded and advanced Green function can be obtained by solving the Dyson equation. For a simplification they are assumed

$$G_{\mathbf{k}_1}^r(t_1, t_2) = -i\theta(t_1 - t_2) e^{(-iE_{\mathbf{k}_1} - \gamma)(t_1 - t_2)} \quad (\text{B.2a})$$

$$G_{\mathbf{k}_1}^a(t_1, t_2) = i\theta(t_2 - t_1) e^{(-iE_{\mathbf{k}_1} + \gamma)(t_1 - t_2)} \quad (\text{B.2b})$$

where $\theta(\cdot)$ denotes the step function.

By taking the eq. (B.2a) and (B.2b) into the eq. (B.1), after some algebraic arrangement, the scattering term in distinct dimensions can be written as

$$\begin{aligned}
 \left. \frac{\partial f_{\mathbf{k}_1}}{\partial t} \right|_{2\text{D,scatt.}} &= \frac{1}{\hbar^2} \int_0^\infty L^2 q dq \int_0^\pi \frac{2}{\pi^2} d\sigma \int_{-\infty}^t dt' \left[\theta(t - t') e^{-2\gamma(t-t')} \left\{ f_{\mathbf{k}_3}(t') [1 - f_{\mathbf{k}_1}(t')] \int_{-\infty}^{t'} dt_2 \right. \right. \\
 &\quad \left. \left. \times V_{s,q}^r(t', t_2) F_{2\text{D}}(t, t_2) - [1 - f_{\mathbf{k}_3}(t')] f_{\mathbf{k}_1}(t') \int_{-\infty}^{t'} dt_2 V_{s,q}^r(t', t_2) F_{2\text{D}}'(t, t_2) \right\} \right] \quad (\text{B.3})
 \end{aligned}$$

where σ denotes the angle between \mathbf{k}_2 and $\mathbf{k}_3 - \mathbf{k}_1$.

$$\begin{aligned}
F_{2D}(t, t_2) &= \int_0^\infty L^2 k_2 dk_2 \int_0^\pi \frac{2}{\pi^2} d\psi \\
&\int_{-\infty}^{t_2} dt_1 \theta(t_2 - t_1) \cos(\Delta E_{k_3, k_1}(t - t') + \Delta E_{k_4, k_2}(t_1 - t_2)) e^{2\gamma(t_1 - t_2)} f_{k_4}(t_1) [1 - f_{k_2}(t_1)] V_{s,q}^r(t, t_1) \\
&+ f_{k_4}(t_2) [1 - f_{k_2}(t_2)] \int_{t_2}^t dt_1 \theta(t_1 - t_2) \cos(\Delta E_{k_3, k_1}(t - t') + \Delta E_{k_4, k_2}(t_1 - t_2)) e^{-2\gamma(t_1 - t_2)} V_{s,q}^r(t, t_1)
\end{aligned} \tag{B.4a}$$

$$\begin{aligned}
F'_{2D}(t, t_2) &= \int_0^\infty L^2 k_2 dk_2 \int_0^\pi \frac{2}{\pi^2} d\psi \\
&\int_{-\infty}^{t_2} dt_1 \theta(t_2 - t_1) \cos(\Delta E_{k_3, k_1}(t - t') + \Delta E_{k_4, k_2}(t_1 - t_2)) e^{2\gamma(t_1 - t_2)} f_{k_2}(t_1) [1 - f_{k_4}(t_1)] V_{s,q}^r(t, t_1) \\
&+ f_{k_2}(t_2) [1 - f_{k_4}(t_2)] \int_{t_2}^t dt_1 \theta(t_1 - t_2) \cos(\Delta E_{k_3, k_1}(t - t') + \Delta E_{k_4, k_2}(t_1 - t_2)) e^{-2\gamma(t_1 - t_2)} V_{s,q}^r(t, t_1)
\end{aligned} \tag{B.4b}$$

where ψ denotes the angle between \mathbf{k}_1 and \mathbf{k}_3 .

$$\begin{aligned}
\left. \frac{\partial f_{\mathbf{k}_1}}{\partial t} \right|_{3D, \text{scatt.}} &= \frac{1}{\hbar^2} \int_0^\infty L^3 q^2 dq \int_0^\pi \frac{\sin \sigma}{\pi^2} d\sigma \int_{-\infty}^t dt' \left[\theta(t - t') e^{-2\gamma(t - t')} \left\{ f_{k_3}(t') [1 - f_{k_1}(t')] \int_{-\infty}^{t'} dt_2 \right. \right. \\
&\quad \left. \left. \times V_{s,q}^r(t', t_2) F_{3D}(t, t_2) - [1 - f_{k_3}(t')] f_{k_1}(t') \int_{-\infty}^{t'} dt_2 V_{s,q}^r(t', t_2) F'_{3D}(t, t_2) \right\} \right]
\end{aligned} \tag{B.5}$$

$$\begin{aligned}
F_{3D}(t, t_2) &= \int_0^\infty L^3 k_2^2 dk_2 \int_0^\pi \frac{\sin \psi}{\pi^2} d\psi \\
&\int_{-\infty}^{t_2} dt_1 \theta(t_2 - t_1) \cos(\Delta E_{k_3, k_1}(t - t') + \Delta E_{k_4, k_2}(t_1 - t_2)) e^{2\gamma(t_1 - t_2)} f_{k_4}(t_1) [1 - f_{k_2}(t_1)] V_{s,q}^r(t, t_1) \\
&+ f_{k_4}(t_2) [1 - f_{k_2}(t_2)] \int_{t_2}^t dt_1 \theta(t_1 - t_2) \cos(\Delta E_{k_3, k_1}(t - t') + \Delta E_{k_4, k_2}(t_1 - t_2)) e^{-2\gamma(t_1 - t_2)} V_{s,q}^r(t, t_1)
\end{aligned} \tag{B.6a}$$

$$\begin{aligned}
F'_{3D}(t, t_2) &= \int_0^\infty L^3 k_2^2 dk_2 \int_0^\pi \frac{\sin \psi}{\pi^2} d\psi \\
&\int_{-\infty}^{t_2} dt_1 \theta(t_2 - t_1) \cos(\Delta E_{k_3, k_1}(t - t') + \Delta E_{k_4, k_2}(t_1 - t_2)) e^{2\gamma(t_1 - t_2)} f_{k_2}(t_1) [1 - f_{k_4}(t_1)] V_{s,q}^r(t, t_1) \\
&+ f_{k_2}(t_2) [1 - f_{k_4}(t_2)] \int_{t_2}^t dt_1 \theta(t_1 - t_2) \cos(\Delta E_{k_3, k_1}(t - t') + \Delta E_{k_4, k_2}(t_1 - t_2)) e^{-2\gamma(t_1 - t_2)} V_{s,q}^r(t, t_1)
\end{aligned} \tag{B.6b}$$

where $V_{s,q}^r(t_1, t_2) = V_q \delta(t_1 - t_2) - 2iV_q \int_{t_2}^{t_1} dt_3 \sum_{\mathbf{k}_2} G_{\mathbf{k}_4}^r(t_1, t_2) G_{\mathbf{k}_2}^a(t_2, t_1) [f_{\mathbf{k}_2}(t_2) - f_{\mathbf{k}_4}(t_2)]$.



H. Haug and A. -P Jauho, “Quantum Kinetics in Transport and Optics of Semiconductors” 2nd ed. (Springer, Berlin, 1998), p.265.

APPENDIX C

G factor for Intersubband Scattering

Under the conservation of energy and momentum, the allow range of in-plane phonon wave vector for the electronic intersubband scattering can be obtained

$$q_{//\max} = k \left[1 + \sqrt{1 + (\Delta E_{e,mn} - \hbar\omega_{LO}) / E_k} \right] \quad (C.1a)$$

$$q_{//\min} = \begin{cases} k \left[1 - \sqrt{1 + (\Delta E_{e,mn} - \hbar\omega_{LO}) / E_k} \right] & , \Delta E_{e,mn} < \hbar\omega_{LO} \\ k \left[-1 + \sqrt{1 + (\Delta E_{e,mn} - \hbar\omega_{LO}) / E_k} \right] & , \Delta E_{e,mn} > \hbar\omega_{LO} \end{cases} \quad (C.1b)$$

where $\Delta E_{e,mn}$ denotes the energy difference between m and n electron's states.

By the definition,

$$k_n = \sqrt{2m_e E_{en}} / \hbar \quad (C.2)$$

$$\alpha = \sqrt{2m_e (\Delta E_c - E_{en})} / \hbar \quad (C.3)$$

$$|B_n| = \left[\frac{2}{(1 + \cos(k_n L_w)) / \alpha + L_w + \sin(k_n L_w) / k_n} \right]^{1/2} \quad (C.4)$$

$$A_n = B_n e^{\alpha L_w / 2} \cos(k_n L_w / 2) \quad (C.5)$$

The G factor used in the dissertation can be shown

$$G_{A\pm(3\rightarrow 2)}^w = \frac{B_3 C_2}{\sinh(q_{//} L_w / 2)} \times \left[\frac{q_{//} \cosh(q_{//} L_w / 2) \sin[(k_2 + k_3) L_w / 2] - (k_2 + k_3) \sinh(q_{//} L_w / 2) \cos[(k_2 + k_3) L_w / 2]}{q_{//}^2 + (k_2 + k_3)^2} + \frac{q_{//} \cosh(q_{//} L_w / 2) \sin[(k_2 - k_3) L_w / 2] - (k_2 - k_3) \sinh(q_{//} L_w / 2) \cos[(k_2 - k_3) L_w / 2]}{q_{//}^2 + (k_2 - k_3)^2} \right] \quad (C.6)$$

$$G_{A\pm(3\rightarrow 2)}^b = \frac{2|A_3||A_2|e^{-(\alpha_2 + \alpha_3)L_w / 2}}{q_{//} + \alpha_2 + \alpha_3} \quad (C.7)$$

where the upper index w and b denote the well and barrier regions. Lower index A± denotes the antisymmetric modes and (3 → 2) denotes the transition from third to second subband.

$$G_{C(3\rightarrow 2)}^{p(\text{even})} = \frac{1}{2} B_3 C_2 \left[\frac{\sin[(p\pi / L_w - k_2 - k_3) L_w / 2]}{(p\pi / L_w - k_2 - k_3)} + \frac{\sin[(p\pi / L_w - k_2 + k_3) L_w / 2]}{(p\pi / L_w - k_2 + k_3)} - \frac{\sin[(p\pi / L_w + k_2 - k_3) L_w / 2]}{(p\pi / L_w + k_2 - k_3)} - \frac{\sin[(p\pi / L_w + k_2 + k_3) L_w / 2]}{(p\pi / L_w + k_2 + k_3)} \right] \quad (C.8)$$

where lower index C denotes the confined phonon modes and upper index denotes the pth modes. The G factor is zero for odd pth modes

$$G_{A\pm(2\rightarrow 1)}^w = \frac{B_1 C_2}{\sinh(q_{//} L_w / 2)} \times \left[\frac{q_{//} \cosh(q_{//} L_w / 2) \sin[(k_2 + k_1) L_w / 2] - (k_2 + k_1) \sinh(q_{//} L_w / 2) \cos[(k_2 + k_1) L_w / 2]}{q_{//}^2 + (k_2 + k_1)^2} + \frac{q_{//} \cosh(q_{//} L_w / 2) \sin[(k_2 - k_1) L_w / 2] - (k_2 - k_1) \sinh(q_{//} L_w / 2) \cos[(k_2 - k_1) L_w / 2]}{q_{//}^2 + (k_2 - k_1)^2} \right] \quad (C.9)$$

$$G_{A\pm(2\rightarrow 1)}^b = \frac{2|A_2||A_1|e^{-(\alpha_1 + \alpha_2)L_w / 2}}{q_{//} + \alpha_1 + \alpha_2} \quad (C.10)$$

$$G_{C(2\rightarrow 1)}^{p(\text{even})} = \frac{1}{2} B_1 C_2 \left[\frac{\sin[(p\pi / L_w - k_2 - k_1) L_w / 2]}{(p\pi / L_w - k_2 - k_1)} + \frac{\sin[(p\pi / L_w - k_2 + k_1) L_w / 2]}{(p\pi / L_w - k_2 + k_1)} - \frac{\sin[(p\pi / L_w + k_2 - k_1) L_w / 2]}{(p\pi / L_w + k_2 - k_1)} - \frac{\sin[(p\pi / L_w + k_2 + k_1) L_w / 2]}{(p\pi / L_w + k_2 + k_1)} \right] \quad (C.11)$$

$$\begin{aligned}
G_{S_{\pm}(3 \rightarrow 1)}^w &= \frac{B_1 B_3}{\cosh(q_{//} L_w / 2)} \\
&\times \left[\frac{q_{//} \sinh(q_{//} L_w / 2) \cos[(k_1 + k_3) L_w / 2] + (k_1 + k_3) \cosh(q_{//} L_w / 2) \sin[(k_1 + k_3) L_w / 2]}{q_{//}^2 + (k_1 + k_3)^2} \right. \\
&+ \left. \frac{q_{//} \sinh(q_{//} L_w / 2) \cos[(k_1 - k_3) L_w / 2] + (k_1 - k_3) \cosh(q_{//} L_w / 2) \sin[(k_1 - k_3) L_w / 2]}{q_{//}^2 + (k_1 - k_3)^2} \right] \quad (C.12)
\end{aligned}$$

$$G_{S_{\pm}(3 \rightarrow 1)}^b = \frac{2|A_3||A_1|e^{-(\alpha_1 + \alpha_3)L_w / 2}}{q_{//} + \alpha_1 + \alpha_3} \quad (C.13)$$

$$\begin{aligned}
G_{C(3 \rightarrow 1)}^{p(\text{odd})} &= \frac{1}{2} B_1 B_3 \left[\frac{\sin[(p\pi / L_w - k_1 - k_3)L_w / 2]}{(p\pi / L_w - k_1 - k_3)} + \frac{\sin[(p\pi / L_w + k_1 + k_3)L_w / 2]}{(p\pi / L_w + k_1 + k_3)} \right. \\
&\quad \left. - \frac{\sin[(p\pi / L_w - k_1 + k_3)L_w / 2]}{(p\pi / L_w - k_1 + k_3)} + \frac{\sin[(p\pi / L_w + k_1 - k_3)L_w / 2]}{(p\pi / L_w + k_1 - k_3)} \right] \quad (C.14)
\end{aligned}$$

where the G factor is zero for even modes.



Vita

Han-Chieh Lee was born in Hong Kong in 1974 and was left to Taiwan ten years later. After the education of junior high school, he began the study of electronics engineering at St. John and St. Mary Institute of Technology and received the degree when he was twenty. Two years later, he got the Bachelor degree of electronics engineering from Chung Yuan Christian University and started the graduate study at the institute of electrical engineering in National Tsing Hua University. At this moment, he was working on the Terahertz generation from semiconductors excited by the ultrashort-pulse Laser in experiment. Two years later, he got the Master degree and began the Ph.D. program at the institute of electronics in National Chiao Tung University. At the early stage, he paid the attention on the fabrication of self-assembled quantum-dot Laser with using molecular beam epitaxy. Two years later, he quitted the field and turned to the carrier dynamics in semiconductors. At the final stage, he used the non-equilibrium Green function to investigate the quantum-kinetic carrier-carrier scattering in GaAs and ended the Ph.D. program when he was thirty. His current research is the non-equilibrium quantum field in curved space time.

Publication List

Journal Papers

H. C. Lee, K. W. Sun, and C. P. Lee, “Significance of Dimensionality and Dynamical Screening on Hot Carrier Relaxation in Bulk GaAs and Quantum Wells” *Solid State Comm.* **128**, 245-250 (2003).

H. C. Lee, K. W. Sun, and C. P. Lee, “Structure Effects on Electron-Optical Phonon Interaction in GaAs/Al_xGa_{1-x}As Quantum Wells” *J. of Appl. Phys.* **92**, 268-273 (2002).

H. C. Lee, “Memory Effect and Dynamical Screening on Nonequilibrium Carrier-Carrier Scatterings in GaAs” submitted to *Phys. Rev. B*.

Attended Conference

H. C. Lee, K. W. Sun, and C. P. Lee, “The Comparison of Screening Behaviors between Bulk GaAs and Quantum Wells in Quantum Kinetic Regime”, 13th International Conference on Nonequilibrium Carrier Dynamics in Semiconductors, Università Di Modena E Reggio Emilia, Italy (2003).

H. C. Lee, K. W. Sun, and C. P. Lee, “Theoretical Investigation on Electronic Intersubband Dynamics via Fröhlich Interaction in GaAs Quantum Wells” and “Effects of The Carrier Temperature on The Plasmon-Phonon Coupling in GaAs/Al_xGa_{1-x}As Quantum Wells”, the Annual Meeting of the Physics Society, Republic of China (2003,2002).

H. C. Lee, C. P. Lee, and K. W. Sun, “Dependence of Electron Energy-Loss Rate on Well Width and Al Composition in GaAs/Al_xGa_{1-x}As Quantum Well Structures”, 10th International Conference on Phonon Scattering in Condensed Matter, Dartmouth College, U.S.A. (2001).